UNIVERSITY OF OKLAHOMA

GRADUATE COLLEGE

# PETROPHYSICAL ROCK TYPING IN UINTA BASIN USING MODELS POWERED BY MACHINE LEARNING ALGORITHMS

A THESIS

SUBMITTED TO GRADUATE FACULTY

in partial fulfillment of the requirements for the

Degree of

MASTER OF SCIENCE

By

CARLOS LENIM ARENGAS SANGUINO

Norman, Oklahoma

2023

PETROPHYSICAL ROCK TYPING IN UINTA BASIN USING MODELS POWERED BY MACHINE LEARNING ALGORITHMS

A THESIS APPROVED FOR THE
MEWBOURNE SCHOOL OF PETROLEUM AND GEOLOGICAL ENGINEERING

BY THE COMMITTEE CONSISTING OF

Dr. Chandra Rai, Chair

Dr. Mark Curtis

Dr. Deepak Devegowda

## Acknowledgements

I would like to express my deepest gratitude to Dr. Chandra Rai, my advisor during my master's degree. Throughout the process of writing this thesis, Dr. Rai provided me with invaluable guidance and support, always pushing me to do my best and to never settle for less. He not only helped me develop my technical skills, but also encouraged me to become a better professional and person.

I am grateful for the patience and understanding he showed me during the most challenging moments, for the time he invested in my education, and for the confidence he had in my abilities. I consider myself fortunate to have had the opportunity to work with such a dedicated and inspiring mentor.

I am also grateful to Dr. Carl Sondergeld, Dr. Deepak Devegowda, Dr. Mark Curtis, and Dr. Son Dang for their support during my research. Their insights, expertise, and willingness to help were instrumental in the development of this work.

My gratitude goes out to my colleagues at $IC^3$, Mikki, and Gary, for their invaluable assistance and encouragement. Their dedication to teaching me and resolving any issues with the lab equipment was crucial to the accomplishment of my research.

I would also like to thank my $IC^3$friends, Rishabh, Felipe, Blessed and Sidi for the camaraderie and assistance, and for the enjoyable moments we shared together.

Lastly, I am grateful to my family and friends for their constant support and encouragement. Their love and belief in me kept me motivated during the most challenging times.

Thank you all from the bottom of my heart.

# Table of Contents

# List of Tables

# List of Figures

# Abstract

Petrophysical characterization is key to identifying different rock types for hydrocarbon production optimization. Rock-typing, a petrophysical characterization technique, can be performed using wireline measurements, such as triple combo and special logs; however, this identification needs to be verified using laboratory characterization to enhance the accuracy of rock-typing prediction models.

In this work, we implement an integrated characterization workflow for 600 ft of the core from the Uinta Basin, including total organic carbon, source rock analysis, elemental (X-ray Fluorescence) and mineral (Fourier-transform Infrared Spectroscopy) composition, total porosity (High-pressure pycnometer, Nuclear Magnetic Resonance), pore throat size distribution (Mercury Injection Capillary Pressure), and microstructure (Scanning Electron Microscopy). Wireline measurements include the triple combo and the sonic logs. Principal Component Analysis and K-means (as an unsupervised machine learning algorithm) were applied to both datasets (core and log) to cluster and classify different rock types. In parallel, the petrophysical systematic for each rock type was evaluated.

The Uinta group is vastly diverse, having a wide range of porosity (2-18%) and TOC (0.5-10%). Three main rock types were identified type 1-siliceous rich, type 2-calcite rich, and type 3-dolomite rich. The relative contribution of types 1, 2, and 3 is 37, 42, and 21 %, respectively. The top section of the analyzed core is dominated by rock type 1, which generally has the highest porosity and relatively higher TOC. Most of the bottom section is carbonate-rich rock types, in which calcite-rich and dolomite-rich layers are interbedded. SEM analyses suggest that a fraction of the porosity is associated with organic matter. Between rock types 3 and 2, further studies indicate that the high dolomite rock type and high total porosity tend to have larger pore size, and better-sorted grains,

while the high calcite rock type has lower porosity and small pore size. There is a fair agreement in rock type identification between using core-derived and log-derived models.

The Uinta basin leads the hydrocarbon production in Utah. The study provides a comprehensive core analysis dataset highlighting the vertical complexity of the Uinta group. The agreement in rock-typing using core and wireline inputs suggests that log-derived rock-typing can be utilized to identify sweet zones.

# Chapter 1: Introduction

Petrophysical characterization is an integral and crucial part of hydrocarbon field development and production. Rock typing is one of the most used methods for characterization. It involves analysis of the available petrophysical and other relevant data to identify rock units in the subsurface having similar characteristics.

Rock typing provides insights into formation heterogeneity and petrophysical properties by correlating the latter to geologic fabrics (Lucia et al., 2003). It classifies the reservoir into distinct rock units or facies with similar petrophysical properties such as total porosity, permeability, mineral composition, fracture distribution, fluid saturation, etc. (Gunter et al., 1997). An ideal rock-typing method clusters individual samples with similar geological and rock properties and refers to them as reservoir building blocks (Guo et al., 2007).

Over the years, many approaches for conventional reservoir characterization, including rock typing, have been published (Barach et al., 2022). In conventional formations, the rock types are identified using core- or well log-derived porosity-permeability cross-plots (Gupta et al., 2017). For example, Amaefule et al. (1993) modified the Kozeny-Carman equation instituting a new concept named Rock Quality Index (RQI) and Flow Zone Indicator (FZI). The parameter identifies zones of similar storage and flow behavior in the subsurface. This technique requires that the formation has a simple relationship between porosity and permeability. It fails where the formation has undergone heavy diagenesis (e.g., carbonates).

Other techniques, such as Winland/Pittman R35, J-function, Thomeer Function, and Electro-facies methods, are based on geology, petrophysics, capillary pressure, logs, and dynamics properties (Rebelle & Bruno, 2014). However, such approaches are mainly limited to sandstones

and carbonates, which have a wide range of dynamic total porosity and permeability values (Kale et al., 2010).

Corbett and Potter (2004) modified the FZI parameter. They came up with universal global hydraulic units (GHE) representing a volume unit of the whole reservoir associated with fluid flow and petrophysical properties. They proposed that by associating the FZI values to the GHE, the rock typing robustness and predictability would increase, mainly when there is a paucity of core data.

Rushing et al. (2008) established that each rock type represents different physical and chemical processes that directly impact the rock properties. Complex geology and heterogeneous systems, such as tight sands, highly impact traditional rock typing accuracy. They concluded that core-derived descriptions such as rock texture and mineral composition must be included for an adequate petrophysical characterization.

Rahmanian et al. (2010) studied low-porosity and -permeability formations. They determined that rock properties were controlled by pore size and pore throat structure. Hence, the pore and pore throat configuration are needed to define the rock types since they control the flow, storage properties, formation features such as brittleness and hydraulic fracturing patterns, etc. Merletii et al. (2014) discussed the limitations of the standard petrophysics analysis. They included porosity, mineralogy, photomicrographs, core descriptions, and the impact of sedimentary and depositional processes on the rock pore geometry to define the rock types in the formation.

Unlike sandstone reservoirs, unconventional formations have extremely low permeability and a narrow range of porosity. Thus, traditional rock typing approaches poorly cluster the formation data into meaningful rock units. Kale et al. (2010) identified three rock types in the Barnett Shale by considering mineral composition, pore size distribution, porosity, and total

organic carbon (TOC) and linked those rock types to gas production. Sondhi et al. (2011) used a similar workflow for the Eagle Ford shale, while Gupta et al. (2012) applied it to the Woodford Formation.

Aranibar et al. (2013) carried out a well log-based rock typing, in the organic-rich Haynesville shale, including the photoelectric factor, density, neutron porosity, compressional- and shear-wave slowness, and elemental capture spectroscopy logs. They proved that well-log-derived petrophysical properties agreed with the core measurements. Lieber et al. (2013) defined three main factors to consider in unconventional rock typing, convectional petrophysical properties, mechanical properties, and reservoir performance.

Amin et al. (2016) performed rock typing in the Eagle Ford formation and defined five rock types using the triple combo and elemental capture spectroscopy (ECS) logs. They estimated the volumetric mineral concentration, porosity, and fluid saturation in the formation and associated the production with the brittleness of the rock types. Gupta et al. (2017) upscaled the core-based rock types to the log-based ones using machine learning algorithms. They related the rock types to production in the Wolfcamp formation.

This work is based on characterizing the Uinta group in Utah by implementing the rock typing workflow. A vastly heterogeneous formation with a wide range of porosity (2-18%) and TOC (0.5-10%). The following properties were measured on 192 plug samples taken from 600 ft of core: total organic carbon (TOC), organic maturity, elemental (by x-ray fluorescence XRF and laser-induced breakdown spectroscopy LIBS), and mineral (by transmission Fourier-transform infrared spectroscopy FTIR) composition, total porosity, pore throat size distribution (by mercury injection capillary pressure), and microstructure (by scanning electron microscope).

The machine learning algorithm known as K-means was used to extract major rock types from the core-based data. Finally, supervised classification approaches, known as support vector machine (SVM), decision tree, and random forest, were used to expand the rock typing procedure to a regional level by validating the relation between core- and log-derived data, which allows the classification of the non-cored wells in the area. The distribution of rock types was correlated to well productivity to determine sweet spots.

## 1.1. Organization of Chapters

This thesis is divided into six chapters. Chapter 2 includes the experimental procedure. It begins with describing the laboratory measurements utilized to perform the petrophysical characterization for the Uinta formation in Utah. The first part of the chapter describes techniques such as TOC, SRA, Fourier transform infrared spectroscopy (FTIR), x-ray fluorescence (XRF), laser-induced breakdown spectroscopy (LIBS), porosity (low- and high-pressure pycnometer), ultrasonic velocity, nanoindentation, and mercury. The second half of Chapter 2 describes data analysis and analytic approaches. It explains unsupervised and supervised machine learning algorithms such as K-means (Lloyd 1957, Macqueen 1967) and support vector machine (SVM) (Cortes and Vapnik 1995), describing how the data is clustered into meaningful groups and correlated to upscale from core-based to log-based rock types. Finally, Chapter 2 ends with the rock typing workflow for this study. Chapter 3 describes the study area in general terms, followed by a lithologic description of the Uinta basin. Chapter 4 contains the experimental results. It summarizes the core-based data available, including mineral profile, total porosity, TOC, pore throat size distribution, and chemostratigraphy. Following the rock typing workflow, the machine learning algorithms are applied to the core data, and then the results are upscaled to well log data. Finally, the rock types

are linked to the production data to identify sweet spots in the area. Chapter 5 employs SEM images to explain the impact of the microstructure of the rocks on petrophysical properties such as TOC, pore throat size distribution, and total porosity. It is also utilized to identify the formation heterogeneity and the microstructure differences among the rock types. Chapter 6 summarizes the rock typing results and includes conclusions and recommendations.

# Chapter 2: Experimental Procedure

In this section, the experimental techniques used to characterize the core petrophysical properties are described in detail.

## 2.1 Laboratory Measurements

The experimental measurements made in this study are low-pressure pycnometer (LPP), high-pressure pycnometer (HPP), and nuclear magnetic resonance (NMR) for total porosity; Rock-Eval for total organic carbon and maturity; Fourier transform infrared spectroscopy (FTIR) for mineralogy; x-ray fluorescence (XRF) and laser-induced breakdown spectroscopy (LIBS) for elemental concentration; scanning electron microscope (SEM) for microstructure analysis, and high-pressure mercury injection capillary pressure (MICP) for pore throat size distribution.

### 2.1.1 Sampling procedure

EP Energy provided 600 feet of an almost continuous core recovered from their operations in Utah. To ensure comprehensive analysis, XRF measurements were taken every inch of the entire core, while LIBS measurements were performed every four inches. One-inch diameter cylindrical plugs were collected at three-foot intervals to reduce potential bias towards specific lithofacies. The plugs were then subjected to various measurements, including total porosity and mineralogical analysis (using FTIR). Various tests, such as MICP, SEM, and TOC, were performed on small pieces taken from each depth.

### 2.1.2 Total porosity measurements

Total porosity measurements estimate the pore volume of the samples by considering the gas, free water, and volatile hydrocarbon inside the pore space. In this study, two methods were

used to determine total porosity. Karastathis (2007) established a helium-expansion method to measure the effective porosity. It involves drying the samples at 100˚C until their weight stabilizes, crushing them to powder while minimizing mass loss, heating the powder to eliminate moisture, and estimating the grain volume using a low-pressure pycnometer. Total porosity is calculated using the grain and bulk volume. In the second method, the total porosity was estimated by adding the gas-filled porosity, measured using the Helium expansion method, to the liquid-filled irreducible porosity, measured using NMR (Mukherjee et al. 2021). The HPP measures gas-filled porosity on dried samples under an injection pressure of up to 200 psi, while the NMR porosity was measured using T2 relaxation distribution with a 12MHz Geospec® Oxford Instrument spectrometer and the acquisition software developed by Green Imaging Technology®. Echo spacing was selected as 114 microseconds to capture fluids within micropores and potentially some heavy hydrocarbon signal (Dang et al., 2018).

### 2.1.3 Mineralogy and elemental measurements

#### *2.1.3.1 Fourier Transform Infrared Spectroscopy*

Figure 1 shows the FTIR spectrometer. It is used to identify and quantifies (in wt. %) sixteen minerals, typically found in sedimentary rocks, by inverting the absorbance spectrum (Sondergeld and Rai, 1993; Ballard, 2007). The minerals included are quartz, calcite, dolomite, aragonite, siderite, oligoclase, albite, orthoclase, illite, chlorite, kaolinite, smectite, mixed-layer clays, apatite, anhydrite, and pyrite.

**Figure 1: Fourier Transform Infrared Spectroscopy Apparatus.**

The accuracy of FTIR mineralogy methodology is equivalent to techniques such as X-ray diffraction and thin section analysis. The primary benefit of the FTIR approach is that it is faster than other procedures, with results available within minutes after the sample preparation. Organic material and moisture need to be removed from the material before running FTIR.

*2.1.3.2 X-ray fluorescence (XRF)*

XRF is a technique used to characterize the elemental composition of a sample. XRF works by exposing the material to X-rays, which excite the electrons on the surface of the material and release radiation. The energy peaks of the released radiation correspond to the elements present in the material (Han et al., 2019). This study used a handheld XRF instrument to analyze the core material. The x-ray beam covers a 10mm diameter circle with an approximately 3mm deep penetration depth. A single reading takes 75 seconds to detect the weight percentage of 27 elements, ranging from magnesium to uranium (U and Th are reported in ppm units). However, it does not provide information about light elements such as carbon and oxygen (Pollard et al., 2007). The XRF analysis is performed using an automated setup to reduce the time and potential human

error. This setup allows for analyzing 9 ft of core in just 2.5 hours, with reading taken every inch (Han et al., 2019).

*2.1.3.3 Laser-induced breakdown spectroscopy (LIBS)*

LIBS is an atomic emission spectroscopy that detects elements from hydrogen to uranium in a sample (Han et al., 2020). This technique involves bombarding the surface of the material with a high-energy laser, which generates a plasma plume filled with excited atoms and ions. As the plasma cools down, it emits light at specific wavelengths associated with unique elements (Effenberger et al., 2010). Argon gas is used during the LIBS analysis to purge the sample and prevent external contamination.

### 2.1.4 Rock-Eval Pyrolysis

Rock-Eval Pyrolysis is a method used to measure the thermal maturity of a sample. The technique involves heating 90 to 100 mg of finely crushed material (35 mesh) in crucibles through pyrolysis and oxidation. During the pyrolysis stage, volatile hydrocarbons are released at temperatures below 300°C and can be measured as the $S_1$ peak. As the temperature increases from 300 to 600°C, heavy hydrocarbons are vaporized and broken down by cracking the remaining kerogen, resulting in the $S_2$ peak. The oxidation stage generates $CO_2$ and CO gases, measured as the $S_3$ and $S_4$ peaks, respectively (Law, 1999; Fouch et al., 2006; Gupta et al., 2017).

### 2.1.5 Scanning Electron Microscopy

Scanning Electron Microscopy (SEM), technology is used to image the nanoscale pore structure of a material. Samples for this analysis must be clean, dry, and conductive (Curtis et al., 2011; Curtis et al., 2012). The samples must undergo a similar preparation for nanoindentation,

including mechanical polishing using sandpaper up to 1500 grit size and ion milling using a Fischione dual beam Argon ion mill (Kumar, 2012a). The images were acquired using the FEI Helios Nanolab 600 Dual-Beam Focus Ion Beam (FIB). SEM provides researchers with topographical or morphological features, composition, and nanostructure information (Curtis et al., 2011; Curtis et al., 2012).

## 2.2 Data Mining and Analytics

Over the past years, decision-making and data-driven processes in the oil and gas industry have benefited from data mining and analytics (Atwal et al., 2016). Data mining tools such as machine learning algorithms provide fundamental means for information extraction, data pattern detection, and forecasting. They allow the integration of huge amounts of geological, production, and surveillance data into a single data analytics platform (Kaushik et al., 2017) toward data-driven decisions to increase operational effectiveness and overall performance.

In data mining and analytics, two main approaches exist: descriptive and predictive. The first focuses on finding correlations, trends, clusters, patterns, and anomalies within the data and typically involves exploratory activities followed by post-processing to validate and interpret the findings (Atwal et al., 2016). On the other hand, predictive data mining is geared towards predicting the behavior of a system under specific conditions, and encompasses techniques such as neural networks, discriminate analysis, and linear regression.

### 2.2.1 Data mining workflow

Data mining and analytics consist of four steps; preprocessing (de-noising), transformation, mining, and interpretation of the data (**Figure 2**) (Han et al., 2001). De-noising involves checking for outliers and errors and verifying the quality of the data (Sharma et al., 2010).

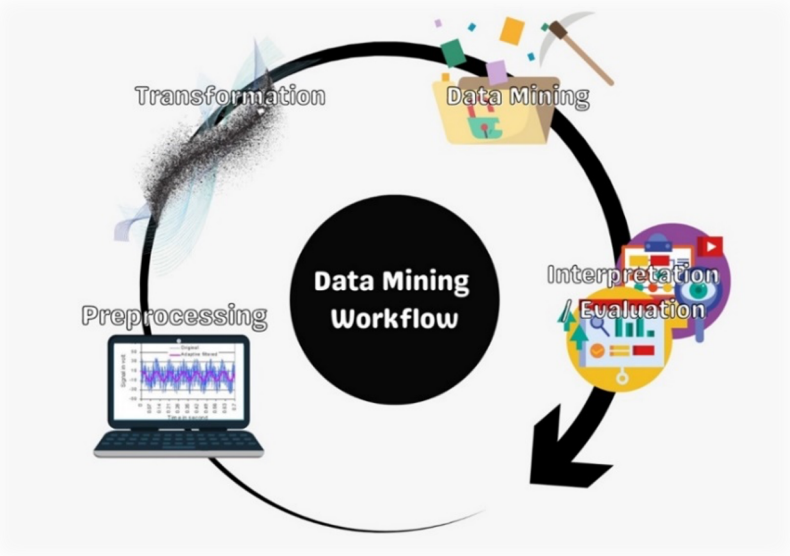


**Figure 2: Data Mining Workflow.**

Data transformation involves changing the data format, structure, or values and is achieved using scripting languages like Python and the expertise of data analysts, engineers, and scientists. Techniques such as Principal Component Analysis (PCA) are used for dimensional reduction (Ringnér et al., 2008).

PCA is a dimensional reduction technique that transforms correlated variables into linearly uncorrelated ones (Pearson, 1901; Hotelling, 1993; Jolliffe et al., 2002). PCA reduces the number

of variables and introduces the principal component of the data (**Figure 3**). Each principal component has the highest variance possible and is orthogonal and uncorrelated to each other. PCA reduces the complexity of the data making it easier to analyze and interpret the data and identify patterns, correlations, and anomalies leading to more effective data analytics (GE et al., 2017). PCA has been combined with other techniques, such as clustering, to improve the accuracy and effectiveness of data analytics in the oil and gas industry (Jolliffe et al., 2002).

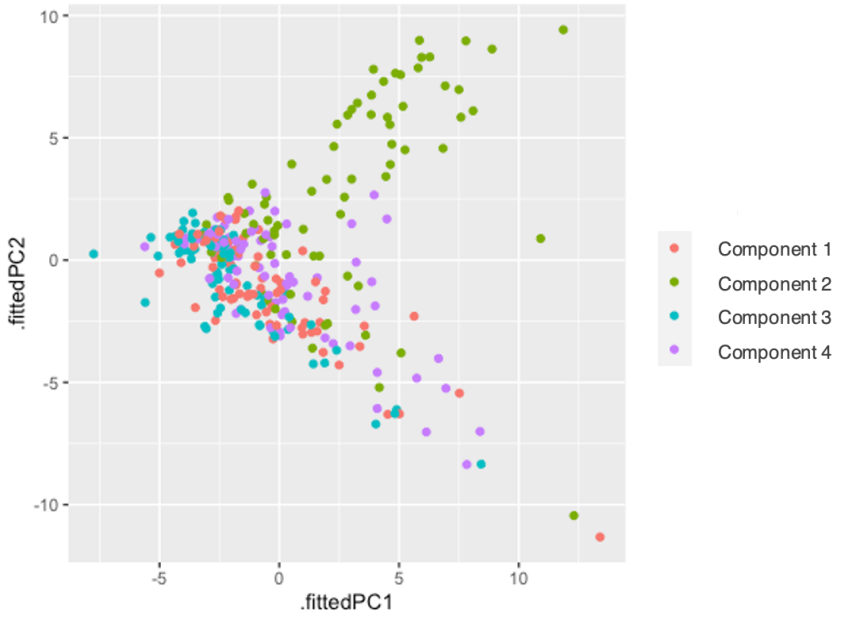


**Figure 3: Principal Component Analysis (Modified from Forecasting.**

The next step is mining. It comprises clustering, classification, association, regression, and anomaly detection (Tan et al. 2006). Cluster analysis groups the items of a data set into comparatively similar groups (Jain et al., 2010). Currently, there are multiple methods for cluster or segmentation analysis (Graham, 2006) and regression and classification. However, the choice of method depends on the characteristics of the data set and the desired outcome. It is important to

consider the suitability of the chosen method for a particular data set, as not all methods may produce accurate results (Jain et al., 2010).

K-means is an unsupervised machine learning algorithm used for clustering data. It was created for signal processing (Lloyd, 1982) and gained popularity due to its ability to manage extensive unlabeled datasets (Macqueen, 1967). K-means clusters an n number of objects (samples) into k numbers of groups based on Euclidean distance (Cai et al., 2022). It tries to find the center of natural clusters in the data by minimizing total intra-cluster variance or the squared error function (**Figure 4**). As **Equation 1** shows:

$$\text{Min} = \sum_{h=1}^{k} \sum_{x \epsilon X_h} ||\text{x} - u_h||^2 \qquad (1)$$

Here, h is the index for each k cluster, where k is the number of clusters. $X_h$ represents the set of all data points in cluster h, while x is a data point in dataset X. The Euclidean distance between data point x and the center of cluster h ($u_h$) is denoted by $||x-u_h||$ (MacQueen, J. B., 1967).

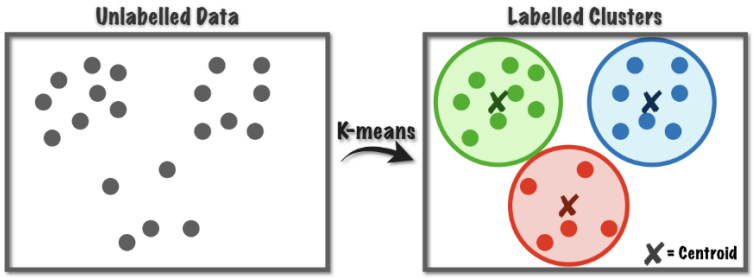


**Figure 4: Schematic of K-means clustering.**

The optimal number of clusters for k-mean is determined based on inter-cluster variance by implementing sum-of-squares within (SSW) (**Equation 2**). The objective is to find the "Elbow"

of the SSW curve (**Figure 5**) to establish the minimum number of clusters that catches the maximum amount of signal from the data (Brownell, 2021).

$$SSW = \sum_{i=1}^{g} \sum_{j=1}^{n_i} (x_{ij} - \bar{x}_i)'(x_{ij} - \bar{x}_i)) \quad (2)$$

Where $x_{ij}$ refers to a data point within a cluster, $\bar{x}_i$ is the mean, g is the total number of clusters, and $n_i$ is the number of data points in the i-th cluster or group (Jain et al., 1999).

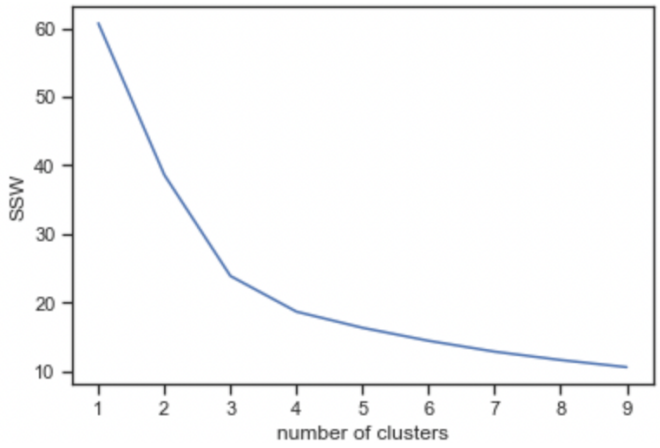


**Figure 5: Optimal number of clusters using the sum of squares within (SSW).**

The Support Vector Machine (SVM) algorithm is a machine learning tool for classification and regression problems (Cortes and Vapnik, 1995). SVM is a linear model that can solve both linear and nonlinear problems and is known for its high precision and relatively low computational requirements. SVM works by finding a hyperplane in N-dimensional space (N being the number of features) that separates two classes of data points (**Figure 6**). The algorithm uses the data points as input and finds a line that separates the classes, maximizing the margin between the two groups.

The resulting hyperplane serves as a decision boundary, classifying the data into two groups. The SVM algorithm has been shown to be effective in a wide range of applications, including image and speech recognition, and has been widely adopted by researchers and practitioners in various fields (Noble et al., 2006).

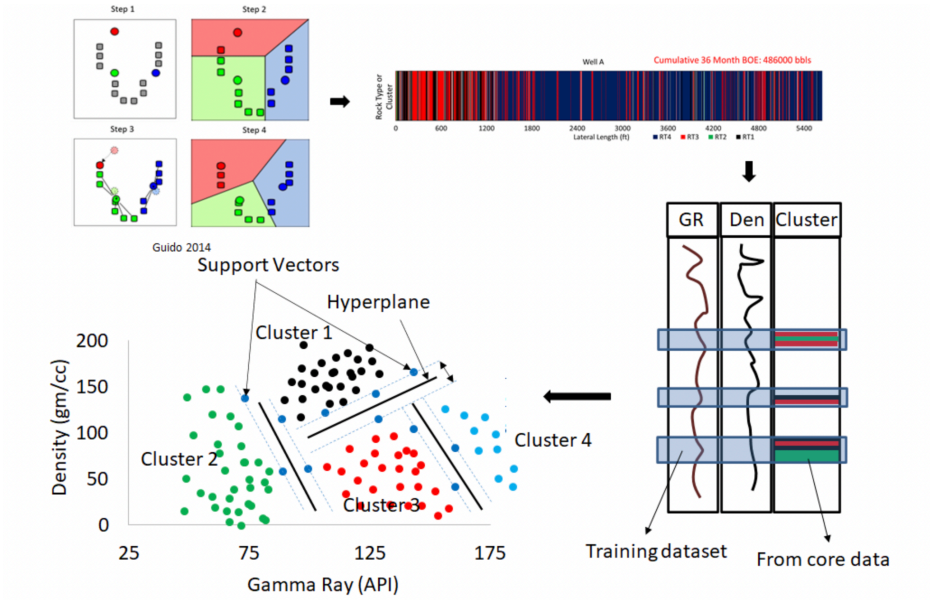


**Figure 6: Support Vector Machine algorithm (Guido 2014).**

The decision tree is a supervised machine learning algorithm that continuously splits the data based on certain parameters. It consists of nodes and leaves, with the latter representing decisions or results and the former being the points where the data is split (Shao-rong, 2007). Each leaf is assigned to a class representing the best goal value and a probability vector indicating the likelihood of the target attribute having a specific value. Decision trees can be understood as a collection of orthogonal hyperplanes. However, simpler decision trees are preferred by decision-makers since they are more easily comprehensible. The complexity of the tree has a significant

impact on accuracy and the stopping criteria and pruning method employed to control the complexity (Breiman et al. 1984).

Random Forest is another supervised machine learning algorithm. It implements multiple decision trees for classification and regression (Zhang and Ma, 2012). Several decision trees are built on randomly selected data points, and the average of the results is selected as the prediction. The random forest algorithm helps to reduce the risk of overfitting, a common problem in decision trees. It also helps to improve accuracy and reduce variance. Random Forest can be used for classification and regression problems and can handle large datasets with high-dimensional features (Hegde and Gray, 2017).

Finally, the results are interpreted and evaluated to support data-driven decision-making and improve the operational effectiveness and overall performance of the companies. Visualization tools are often used in this step.

## 2.3 Rock Typing Workflow

This study follows a workflow that involves multiple steps. Firstly, petrophysical properties are measured on plug samples, including total organic carbon, mineral composition, porosity, seismic response, and mechanical properties. Then, the petrophysical lab datasets including total porosity, TOC and calcite, dolomite, quartz, and clay content, are preprocessed by removing outliers and anomaly values to ensure high accuracy and low associated error. Next, PCA is applied to the selected petrophysical properties to define the principal components, reducing the complexity of the data. The core material is then categorized using clustering techniques (K-means) based on those principal components, resulting in three rock types with

different petrophysical properties. Additional petrophysical data is added to the rock types if available. Next, SVM, decision tree, and random forest are used to upscale the rock types at the log level from the core-based data, verifying the correlation between core- and log-based data for the well. The rock typing exercise is then performed using the triple combo and sonic log data. Following, well log data from neighboring wells are used to carry out the rock typing exercise, defining the rock types for those locations. Finally, the rock types are linked to production to identify the sweet spot in the formation and analyze how different rock types impact production in the area. Additional analyses are carried out to verify the quality of the results and provide robustness to the petrophysical study.

# Chapter 3: Uinta Basin

## 3.1. Study Area Description.

The Uinta Basin is a promising unconventional play in the United States. This basin is located in northeastern Utah, east of the Wasatch Mountains and south of the Uinta Mountains (USGS, 1979). The Basin covers an area of 9,300 square miles and is located 200 miles east of Salt Lake City (**Figure 7**). The extension of tertiary sedimentary rocks delimits it.

The formation began producing gas and oil in significant quantities in 1925 and 1949. The hydrocarbon production in the basin comes mainly from Duchesne and Uintah counties (Source: Utah Department of Natural Resources, NGI's Shale Daily calculations). Hydrocarbon production as of June 2022, is 17,662,335 barrels of oil and 100,973,285 MCF of natural gas, making it the leading producer of hydrocarbons in Utah (Utah Division of Oil, Gas, and Mining, 2022).

According to the Utah Geological Survey, the thickness of conventional and unconventional tight sands and shale formations in the Uinta Basin ranges from 1,300 to 18,000 feet. Vertical wells are the majority in the area, but horizontal drilling is increasing. The Basin has two leading commercial formations; in the north, the Wasatch produces from highly discontinuous sandstones, and in the south, the Green River produces from sandstones, shales, and carbonates.

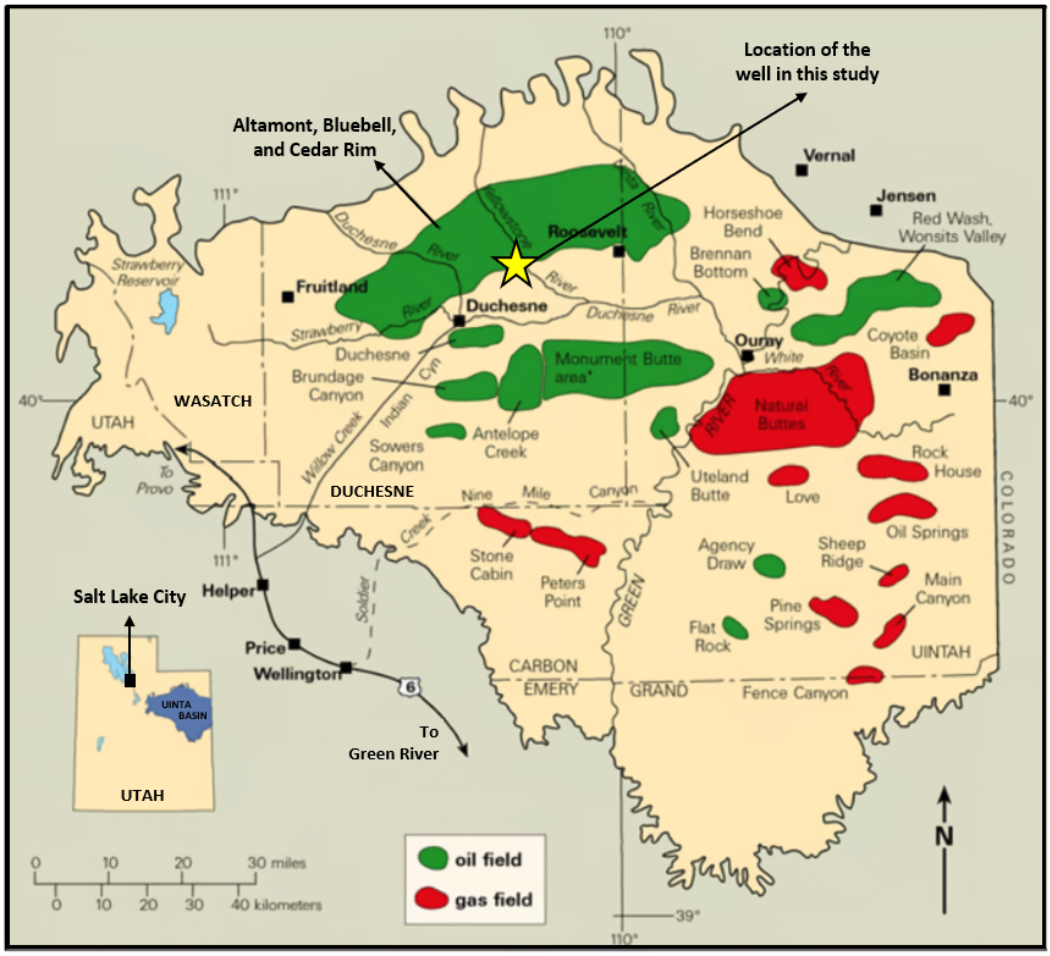


**Figure 7: The map illustrates the boundary of the Uinta Basin in Utah, with Salt Lake City marked as a reference point. The oil-producing wells are predominantly located in the northern region, while gas is frequently found in the south and east. The yellow star indicates the source rock material location for this study, which is situated in the Altamont, Bluebell, and Cedar Rim areas (Utah Geological Survey, Crude Oil).**

## 3.2. Geological Description

In central Utah during the Late Cretaceous Epoch, tectonic activity in the Sevier orogenic belt caused the marine shoreline to recede, forming an internally drained depression. This depression was abundant in marine shale and was covered by coastal sandstone units, followed by paludal and alluvial beds. During the early Tertiary period, the uplift of the Uinta Mountains and

Uncompahgre structure altered the sedimentation patterns of the Cretaceous period, resulting in the formation of the Uinta Basin as we know it today (Yoshida et al., 1995; Johnson et al., 2003; Blackford et al., 2021).

The Uinta Basin is comprised of three distinct facies. The central core is made up of organic-rich lacustrine claystone and mud-supported carbonate, known as the "open lacustrine" facie. The second facie called the "marginal lacustrine," encompasses deltaic, inter-deltaic, and lake-margin carbonate-flat environments and is characterized by sandstone, claystone, and mud- and grain-supported carbonate units. The third and final facie, the "alluvial facies," consists of alluvial claystone, conglomerate, and sandstone beds deposited beyond the marginal lacustrine sediments (Walton, 1994; Roehler, 1993). Fouch (2006) identified six markers within the Green River Formation, starting from the bottom: the lower marker, the Paleocene-Eocene boundary, the top of the carbonate marker unit, the middle marker, the Mahogany oil-shale bed, and the upper marker. The strata closest to the Paleocene-Eocene boundary marker exhibit the highest productivity, and a substantial amount of oil and gas is concentrated near the lower marker.

**Figure 8** illustrates the stratigraphy of the Uinta Basin, depicting the Duchesne, Uinta, Green River facies, Wasatch, Colton, and North Horn formations. The map also shows the depositional environment of each facies, whether it is alluvial, marginal lacustrine, or open lacustrine. Additionally, it displays the markers of the Green River Formation as defined by Fouch (1975). The map also identifies black and yellow waxy oil deposits in the region.

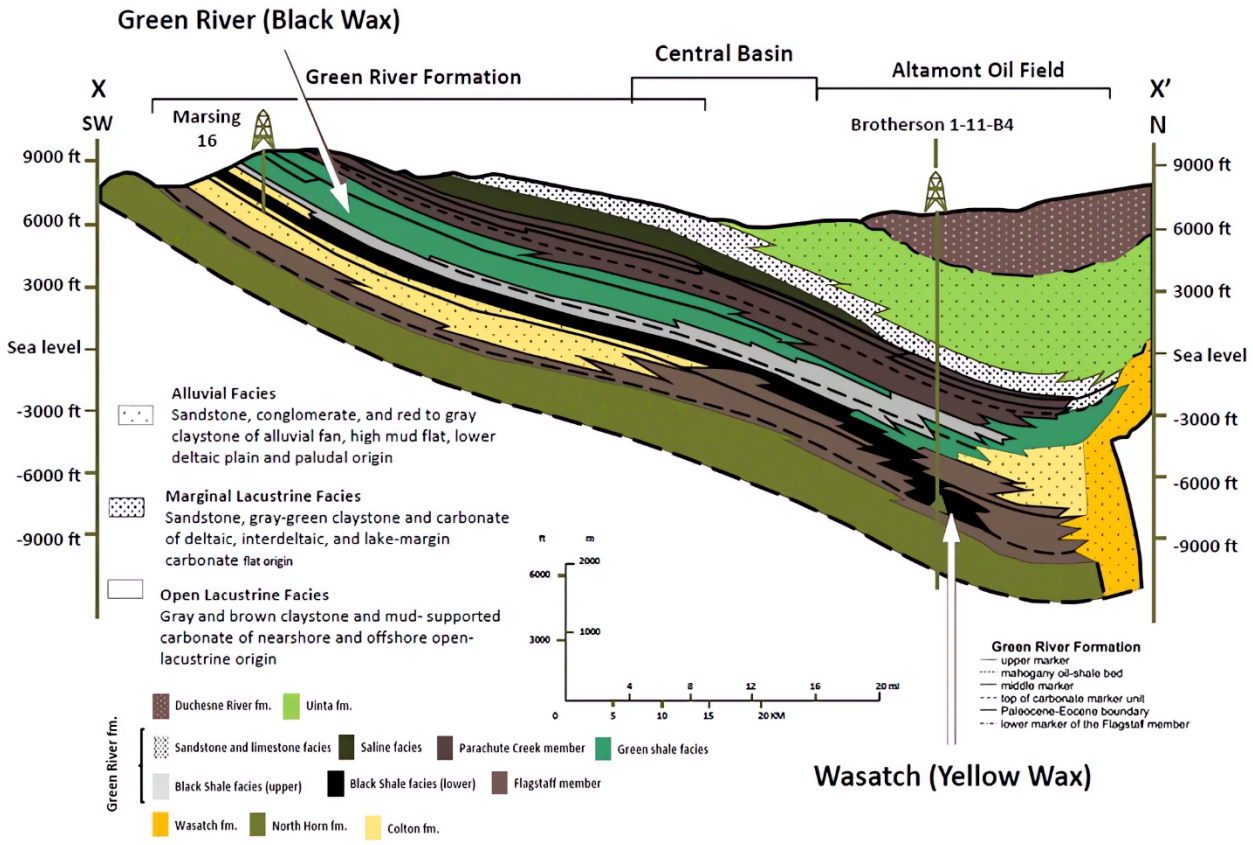


**Figure 8: Generalized structural-stratigraphic cross-section from outcrops on the southwest flank of the Uinta Basin, through Duchesne and Altamont-Bluebell oil fields, to the north-central part of the Basin. This study focuses on the Altamont oil field (Modified from ShaleExperts.com; Fouch (1975)).**

In the Basin, the open lacustrine source rock in the central core is responsible for generating oil and gas. On the south flanks, gas production is dominant in the overbank and channel sandstone facies, while bitumen surrounds the northeast border. The Altamont-Bluebell area primarily depends on overpressure sequences for production, with the marginal lacustrine facies serving as the primary reservoir rock and the source of the most productive fields. Porosity within the delta-front, overbank, and channel sandstone units provides most of the hydrocarbon storage capacity in the deeply buried Tertiary rocks in the western part of the Basin (Chidsey, 2018).

Wells completed in the pressured and over-pressured rocks of the marginal lacustrine facies are known to have a longer productive lifespan than wells in other facies. The alternating marginal and open lacustrine lithofacies provide contrasts in elasticity between the brittle mud-supported carbonates and the relatively ductile claystones of the marginal lacustrine facies. This interbedding of beds of contrasting ductility influences the frequency of fractures, which provide much of the permeability needed to drain the low-porosity reservoir units. Marginal lacustrine facies are known to contain bituminous sandstone accumulations from the Tertiary period. Both carbonate and siliciclastic rocks, deposited as deltaic, interdeltaic, and lake-margin carbonate-flat sediments, form major reservoir bodies rich in hydrocarbons. Although alluvial facies are not typically oil-producing, their relative impermeability in deeply buried Tertiary rocks makes the alluvial overbank and channel-sandstone reservoirs gas-bearing along the south flank of the Basin. Rocks of alluvial origin are hydrocarbon-bearing at Asphalt Ridge in the northeast part of the Basin.

**Figure 9** presents the isopach map of the Uinta Basin, displaying the thickness variation of sedimentary rocks from the top of the Cretaceous layer to the base of the Long Point Bed, a transgressive bed deposited around 53 million years ago during the early Eocene in the Uinta Basin (Johnson, 1985). The map reveals that the thickness of the sedimentary rocks in the Greater Green River Basin increases in the direction of both the Uinta Mountains and the Sevier orogenic belt.

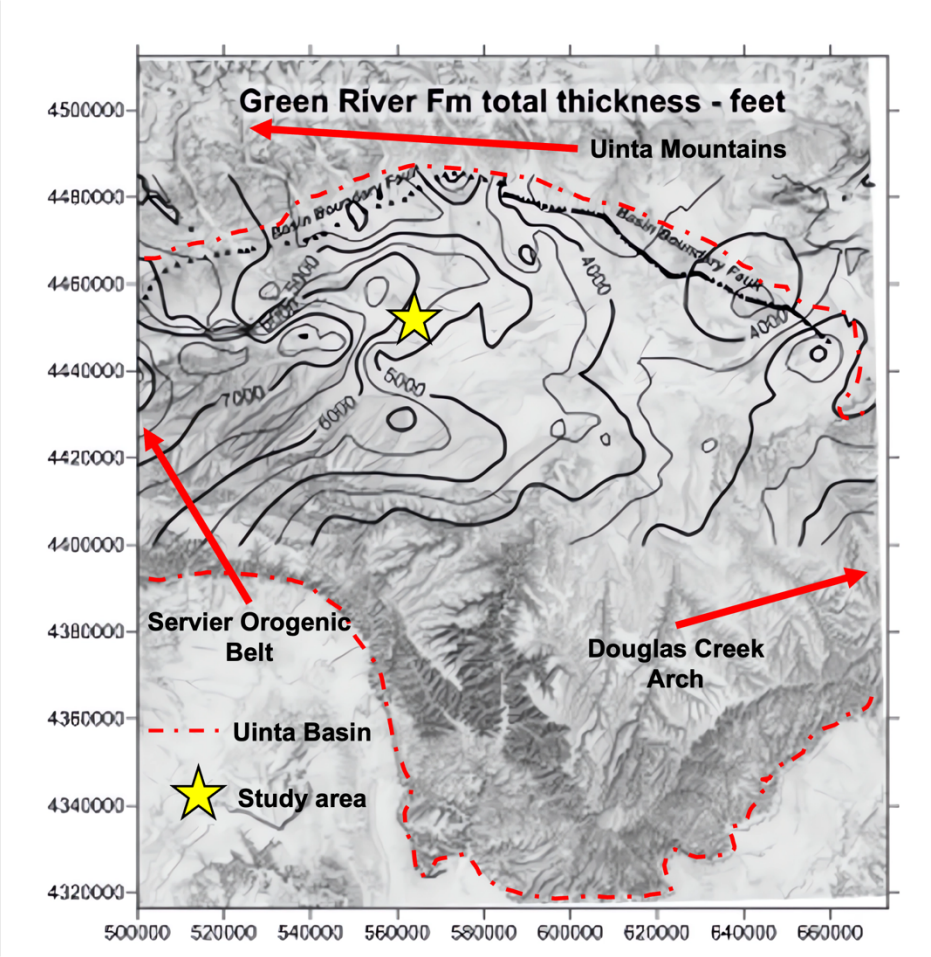


**Figure 9: Isopach map for the entire Green River formation from the base of the Uteland Butte member ("black shale facies") to the top of the formation. Thickness varies from less than 3000 feet in the southeast towards the Douglas Creek Arch (On the border with Colorado) to over 7500 feet in the northwest in the direction of the Uinta Mountains and the Servier orogenic belt. This variation in the thickness affects the spatial distribution of thermal maturity of the Green River source rocks (Modified from Schamel, 2015).**

**Figure 10** presents the vitrinite reflectance trends for the lower part of the Green River Formation (USGS, 2012). According to the map, the northern section of the lower part (Cast Peak and Uteland Butter members) exhibits a higher degree of maturity and falls within the range of the wet-gas to the dry-gas window. Conversely, the southern part of the area is comparatively less mature and falls within the oil and thermal immature windows (Nuccio and Roberts, 2003). In the Altamont-Bluebell and Cedar Rim at a depth greater than 10,000 feet, gas and oil generation from

thermal cracking of the Black Shale facies and more mature parts of the Uinta Basin are the cause of overpressure zones (Schamel, 2015).

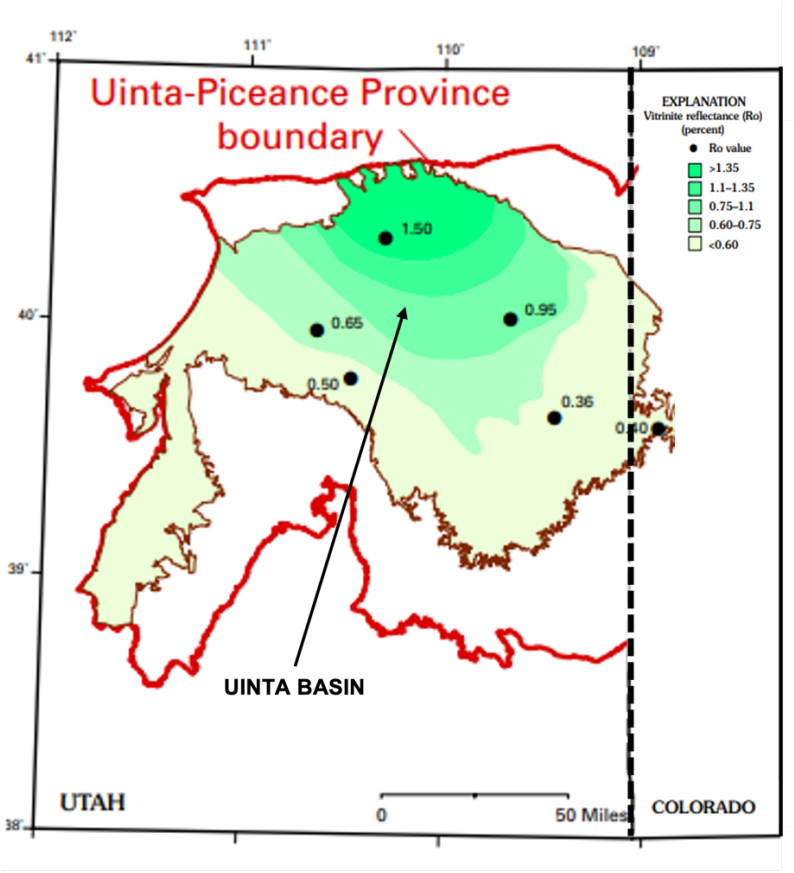


**Figure 10: Vitrinite reflectance (Ro) values trend at the horizon of the lower part of Green River Formation based on five wells (Modified from Nuccio & Robberts, 2003).**

The source rock for this investigation is from the Green River Formation. It is a geologic formation in the western United States, primarily in Utah and Wyoming, with smaller parts in Colorado and Idaho. It is known for its rich fossil beds and its oil shale deposits. The Green River Formation, middle and lower members, can be categorized into five distinct reservoirs: Uteland Butte (also known as the "black shale" facies), Castle Peak, lower Douglas Creek, upper Douglas Creek, and Garden Gulch (or Parachute Creek). These reservoirs are made up of one or more beds

with comparable paleodepositional history, petrography, and diagenesis that are characteristic of each reservoir (Picard, 1995; Craig, 2003).

The core material in this study corresponds to the Castle Peak and Uteland Butte reservoirs (**Figure 11**). The first was formed approximately 50 million years ago during the Eocene Epoch and is composed of several rock units, including interbedded fine-grained lacustrine (lake) shale, sandstone, and limestone. Much of the reservoir is made up of fine-grained shale, which was deposited in a large freshwater lake environment (Chidsey, 1991; Kietzke et al., 1993; Riester et al., 1993; Dembicki et al., 1994;). The sandstone layers in the Castle Peak reservoir were deposited by rivers and deltaic systems that flowed into the lake and are known for their high levels of compaction and abundant feldspar and quartz cementation (Trumbo, 1993; Hintze & Kowallis, 2009; Chidsey, 2018), while the limestone layers represent carbonate deposits formed in shallow lake environments.

The Uteland Butte reservoir comprises various types of rocks such as limestone, dolostone, calcareous mudstone, siltstone, and occasionally sandstone. The limestone beds are mostly grainstone, packstone, or wackestone supported by ostracods or mud. The shallower deposits are predominantly grainstone, whereas argillaceous limestone is common in deeper distal deposits. Some cores have revealed a dolomitized compacted wackestone with ostracods near the top of the Uteland Butte, which contains more than 20% porosity but low permeability (less than one millidarcy). Studies suggest that the reservoir was formed during shoreline retrogradation and lake-level deepening, with sediment consisting of micritic limestone, dolomite, and calcareous mudrocks (Craig et al., 2002). The Uteland Butte is distinctive in that it has a high concentration of carbonate rocks and rare occurrences of siliciclastic rocks, possibly due to rapid lake-level rise or the location of the main inflow into the lake. The Uteland Butte reservoir comprises the oldest

rocks in the Green River Formation, and it is called “black shale” facies due to their dark color and high content of organic matter.

Crouch et al. (2000) reported that the Uteland Butte reservoir, which is almost entirely carbonate and lacks sandstone, has very low oil recovery due to its low permeability of 0.4 to 0.01 millidarcy. Therefore, it is not the primary target of drilling and is considered a secondary objective. The reservoir is oil-producing.

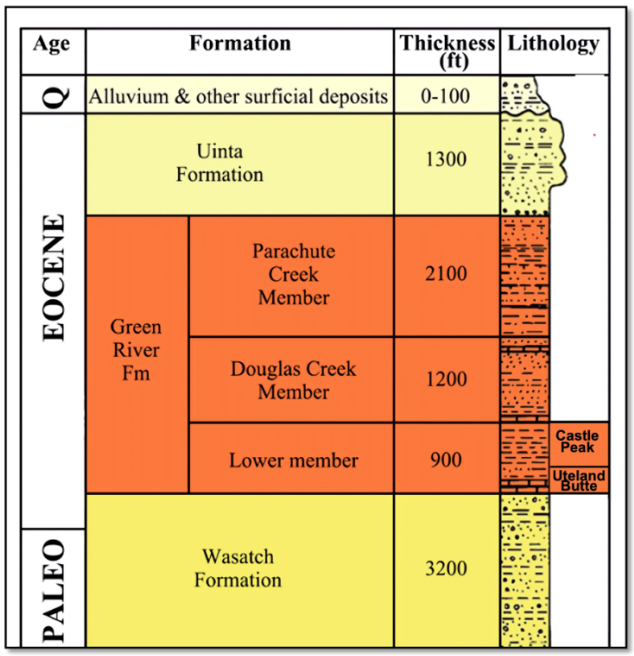


**Figure 11: Stratigraphy column of the Uinta basin from the surface to the bottom of Wasatch Formation, through the Green River formation, including the Castle Peak and the Uteland Butter reservoirs (Modified from Chidsey, 2018).**

The Uinta Basin is known for its high-paraffin crude oil, also known as waxy oil, which presents operational difficulties for regional oil companies. This type of oil tends to solidify when cooled, requiring it to be kept heated throughout its transportation via pipeline, rail, or truck. Shipping waxy crude can be logistically challenging, leading to increased operational costs and a

discounted price for the oil (UGS, 2014). The Green River Formation, located in the Uinta Basin, has been a significant source of hydrocarbon generation for over 50 years. However, the conventional recovery techniques used in the past have focused on interbedded sands or carbonates rocks. Despite extensive research, there is limited understanding of the unconventional crude oil production potential of thinner, organic-rich shale/carbonate units, such as the Uteland Butte member and deep Mahogany zone, making these areas a focus of ongoing exploration efforts.

# Chapter 4: Results and Data Analysis

This study utilized 600 feet of core recovered from a well in the Uinta basin. The upper section was 269 feet, and the lower section was 329 feet thick, with 211 feet missing between the two sections. XRF measurements were made at 5161 discrete depths and LIBS at 1602 depth points. Total porosity was measured at 198, and ultrasonic velocity at 68 discrete depths on plugs. FTIR, TOC, and thermal maturity tests were performed at 208, MICP at 153, nanoindentation at 48, and SEM at 26 depths on small sample pieces. These tests provide valuable information about the elemental composition, mineral content, rock properties, organic content, thermal history, pore structure, fluid saturation, mechanical properties, and microstructure of the formation.

## 4.1. Elemental Composition

The elemental composition of the core was determined using XRF and LIBS techniques. The results showed a considerable variation in the elemental composition with depth for both the upper and lower sections of the core. XRF was used to obtain the concentration of the following elements: manganese, phosphorus, magnesium, aluminum, silica, potassium, calcium, iron, sulfur, uranium, and thorium. These elements allow identifying the main mineral that makes up sedimentary rocks. **Figures 12** and **13** display the XRF elemental profiles for the upper and lower sections, respectively. At the top and bottom, the upper section is rich in silica, commonly associated with minerals such as quartz, feldspar, and different clays (MacKenzie, 1970; Thimm, 2006; Coyle et al., 2014; Mayorga-Gonzalez et al., 2021). High silica concentration could indicate siliciclastic sedimentary rocks, including mudrocks (shales) and sandstones. **Figure 12** (the upper section) shows aluminum-rich zones, which may reveal the presence of aluminum-bearing minerals, such as clay minerals or feldspar (Kodoma et al., 2022). A high concentration of iron at

the top and bottom is seen, which could indicate the presence of minerals such as pyrite ($FeS_2$), commonly found in sedimentary rocks subjected to reducing conditions during diagenesis (Jacobi et al., 2022).

Interbedded silica and calcium-rich layers are presented in the middle part of the upper section, with significant sulfur peaks. High calcium concentrations in a rock could indicate the presence of calcium-rich minerals such as calcite ($CaCO_3$) or anhydrite ($CaSO_4$). These minerals are often associated with sedimentary rocks, such as limestone. Calcium concentration could also suggest that the rocks were formed in a marine environment or a series of interconnected lakes, where organisms can produce calcium carbonate shells that eventually accumulate to form limestone (Morse and Mackenzie, 1990). The combination of high calcium and silica concentrations in the Uinta Basin could suggest the presence of limestone and siliciclastic sedimentary rocks in the region. This interpretation is consistent with the geological history of the basin, which is characterized by a series of ancient lakes and shallow seas that deposited layers of limestone, sandstone, and shale over millions of years (USGS, 1979). High concentrations of sulfur in the Uinta basin could indicate the presence of organic matter that contain sulfur or minerals such as pyrite (Jacobi et al., 2022).

**Figure 13** shows the elemental profile for the lower section. This section is richer in calcium as compared to the upper section. Thin silica streaks are observed throughout the section. Magnesium concentration is significantly high in the lower section, indicating the presence of minerals such as dolomite or magnesite or magnesium-rich clay mineral such as chlorite (Markin et al., 2019). The presence of dolomite ($CaMg(CO_3)_2$) is often associated with marine or lacustrine environments and diagenesis (Wilson et al., 1990; Nader et al., 2007; Budd and Mathias, 2015; Hollis et al., 2017; Al-Ramadan et al., 2019; Koeshidayatullah et al., 2020).

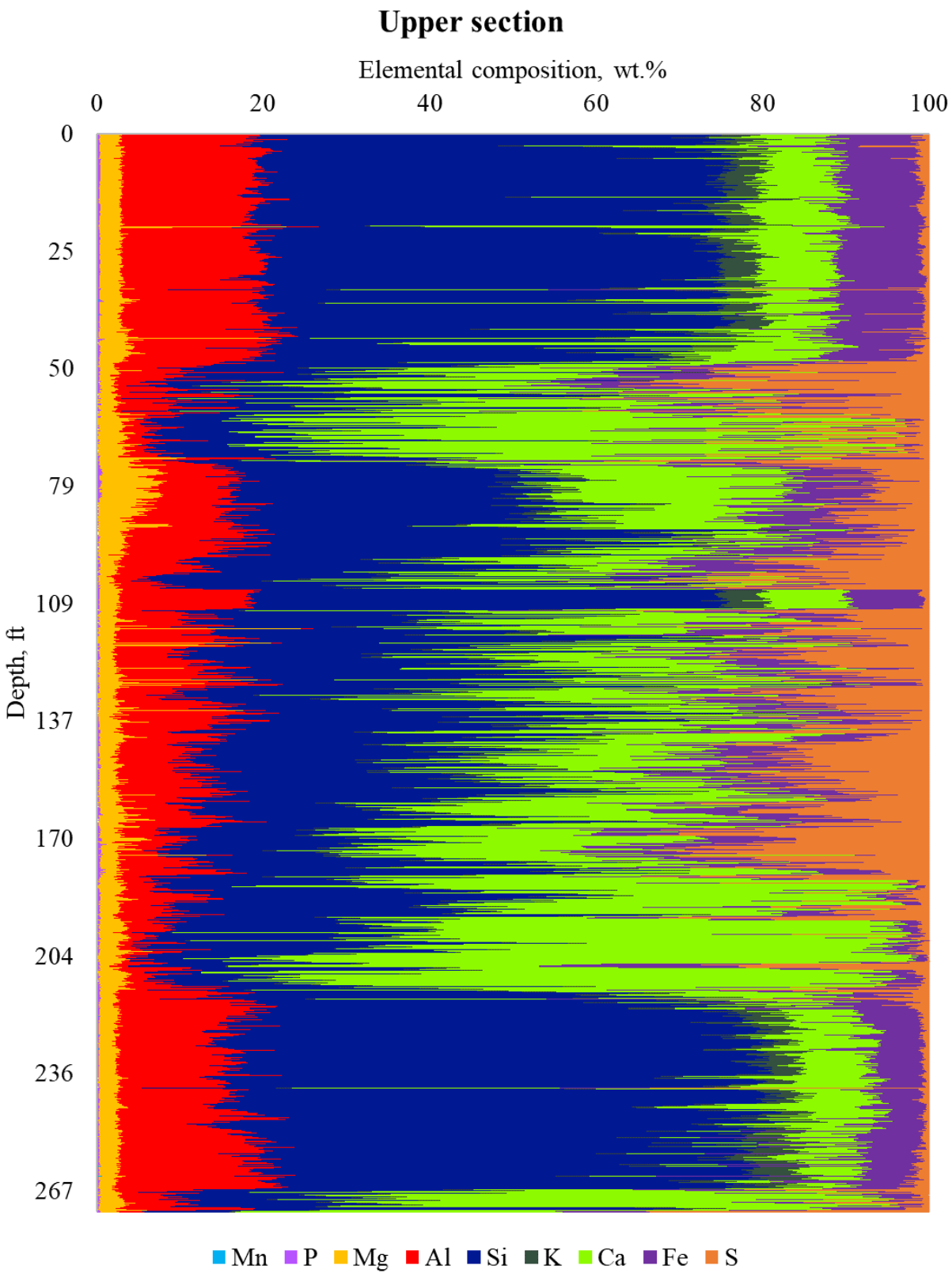


**Figure 12: XRF elemental concentration as a function of depth for the upper interval.**

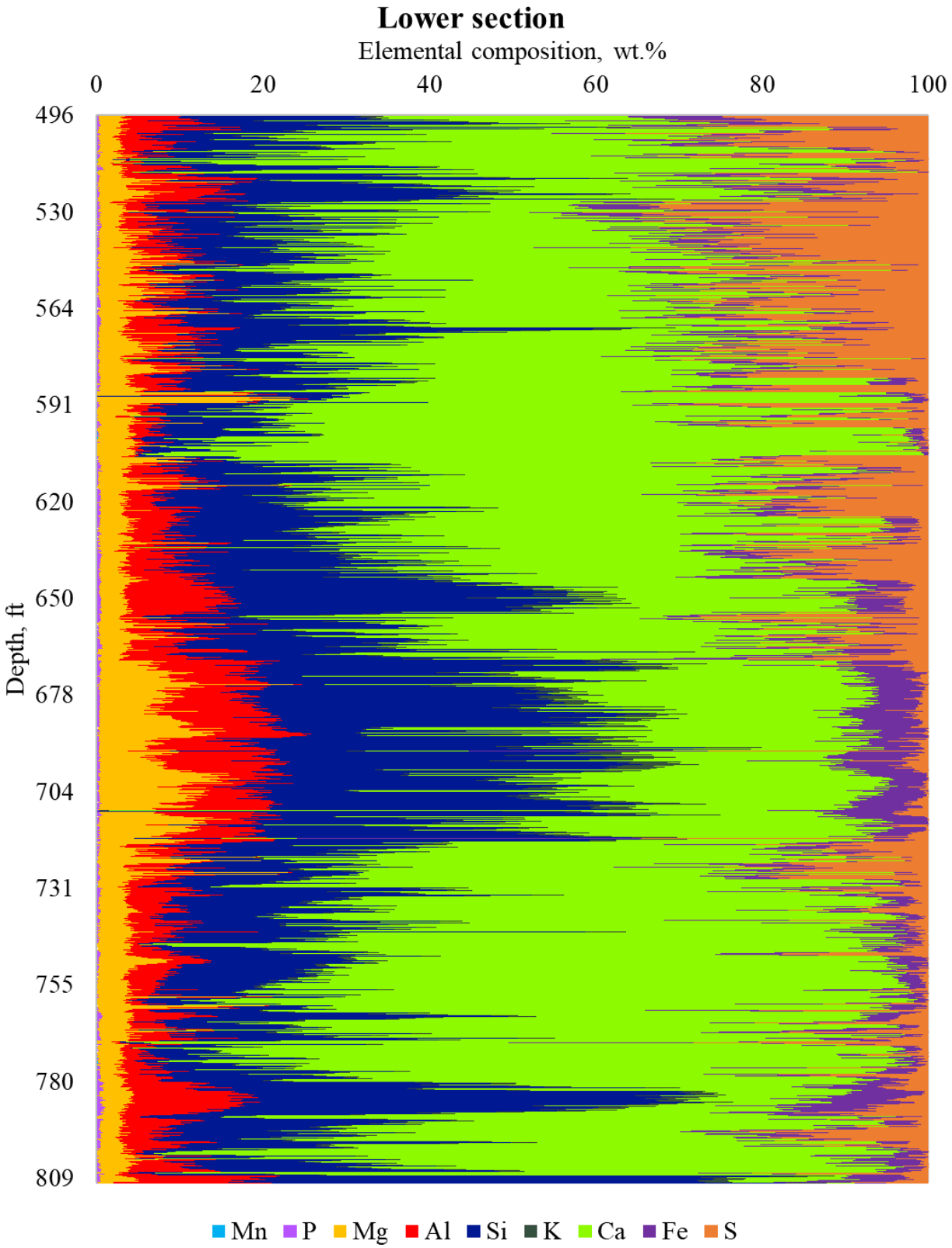


**Figure 13: XRF elemental concentration as a function of depth for the lower interval.**

**Figures 14** and **15** show the elemental profile obtained by LIBS for the core material. It includes all the elements shown in the XRF plus carbon and sodium (light elements that XRF cannot detect). LIBS results closely align with XRF. The upper section is rich in silica with calcium peaks; the aluminum concentration is significantly higher than other elements indicating siliceous-rich rocks. The lower section exhibits layers of calcium and silica with a significant magnesium concentration. This differs from the XRF results for the lower section, where calcium dominates the whole portion. One potential source of error for LIBS calcium estimation is the presence of interference from other elements, such as magnesium (abundant in the lower section). Due to the similar electronic configurations between the two elements (Ca and Mg), LIBS reading of calcium intensity emission lines leads to underestimating the calcium concentration (Cremers & Radziemski, 2006; Harmon et al., 2019).

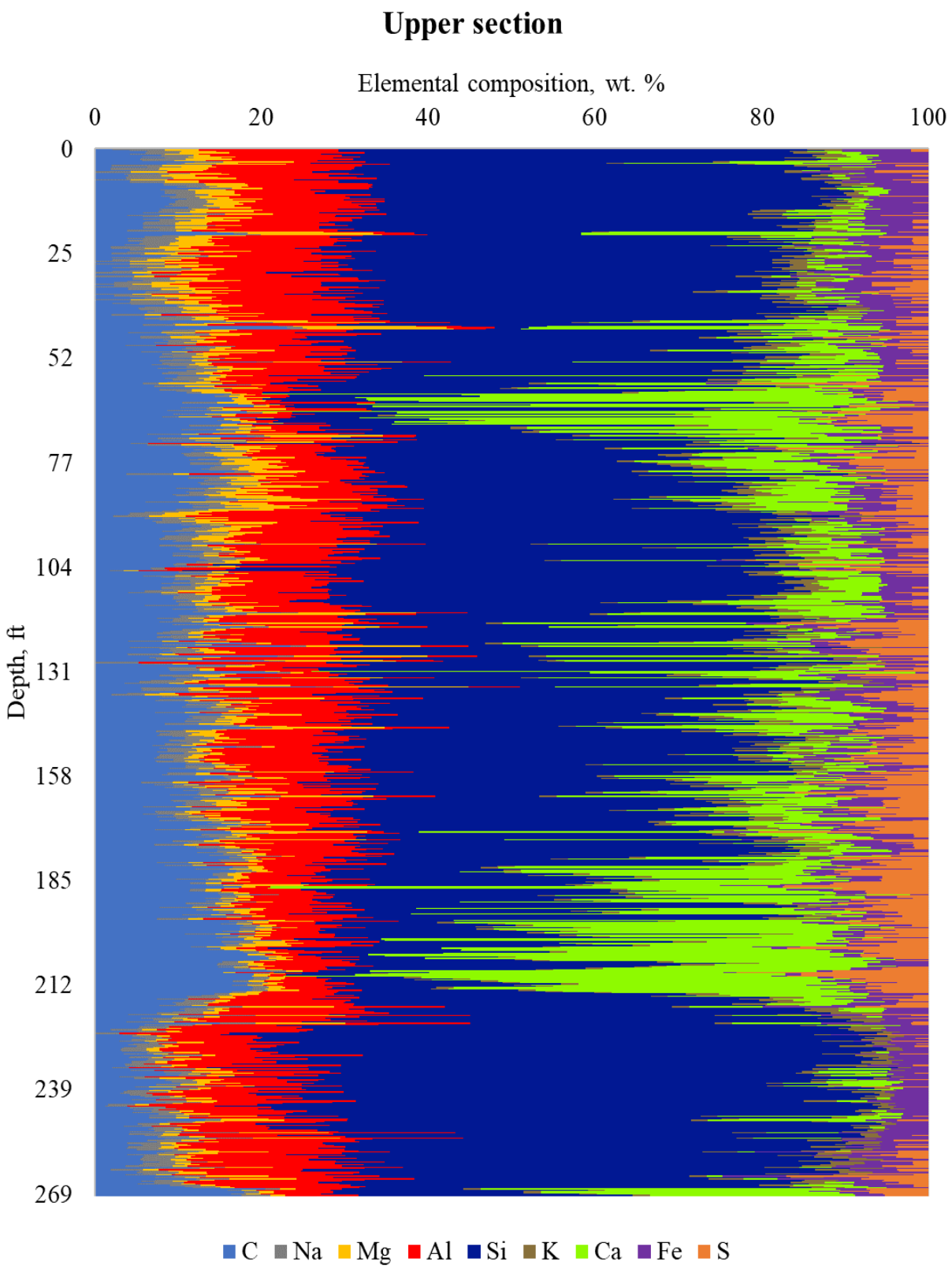


**Figure 14: LIBS elemental concentration as a function of depth for the upper section.**

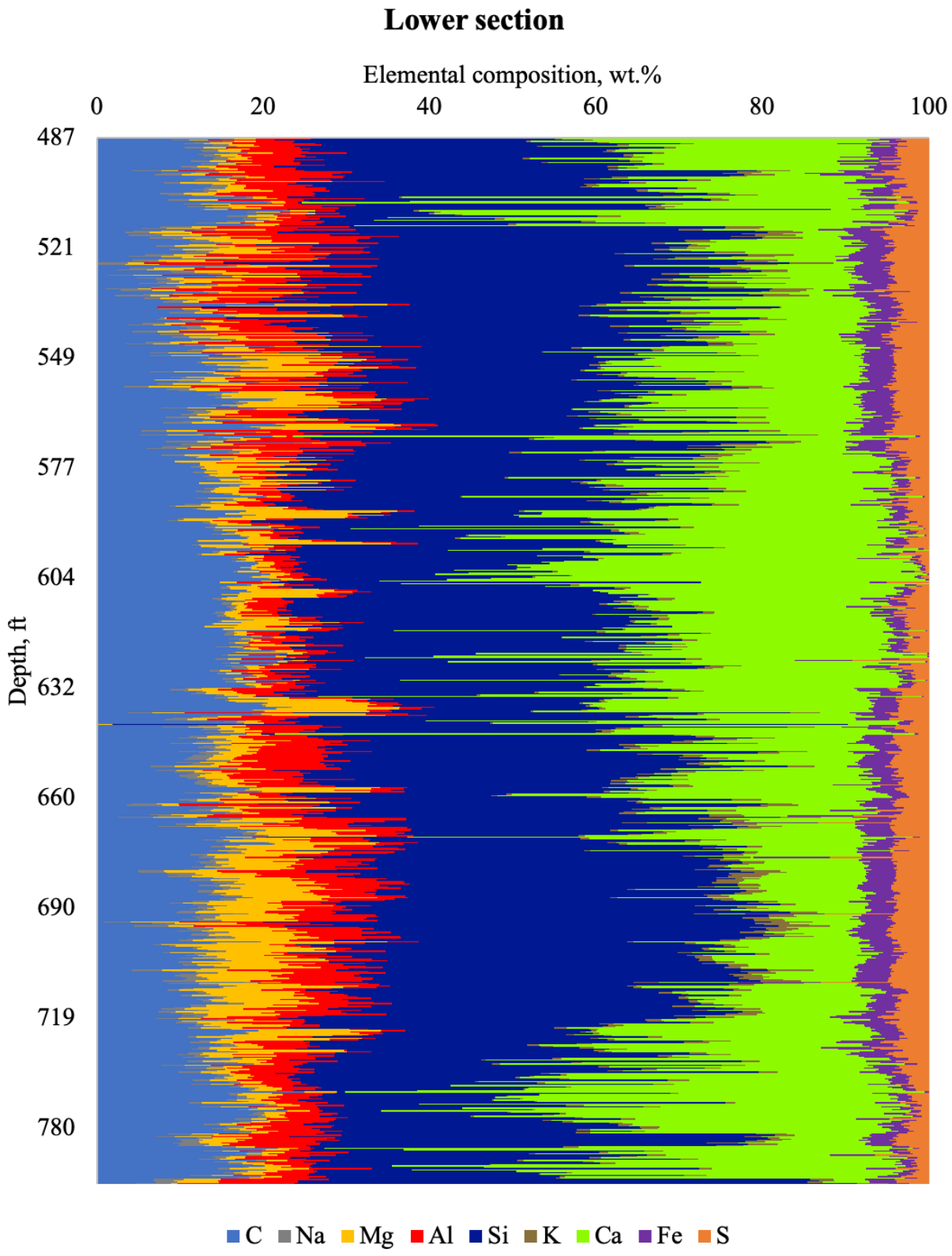


**Figure 15: LIBS elemental concentration as a function of depth for the lower section.**

## 4.2. Total Porosity

The total porosity of the samples was measured using the HPP and NMR techniques on dried plugs. The LPP technique developed by Karastathis (2007) was utilized to corroborate the total porosity results. **Figure 16** presents the total porosity histogram. The results show that total porosity ranges from 2 to 18%, with most samples having values between 6 to 9%.

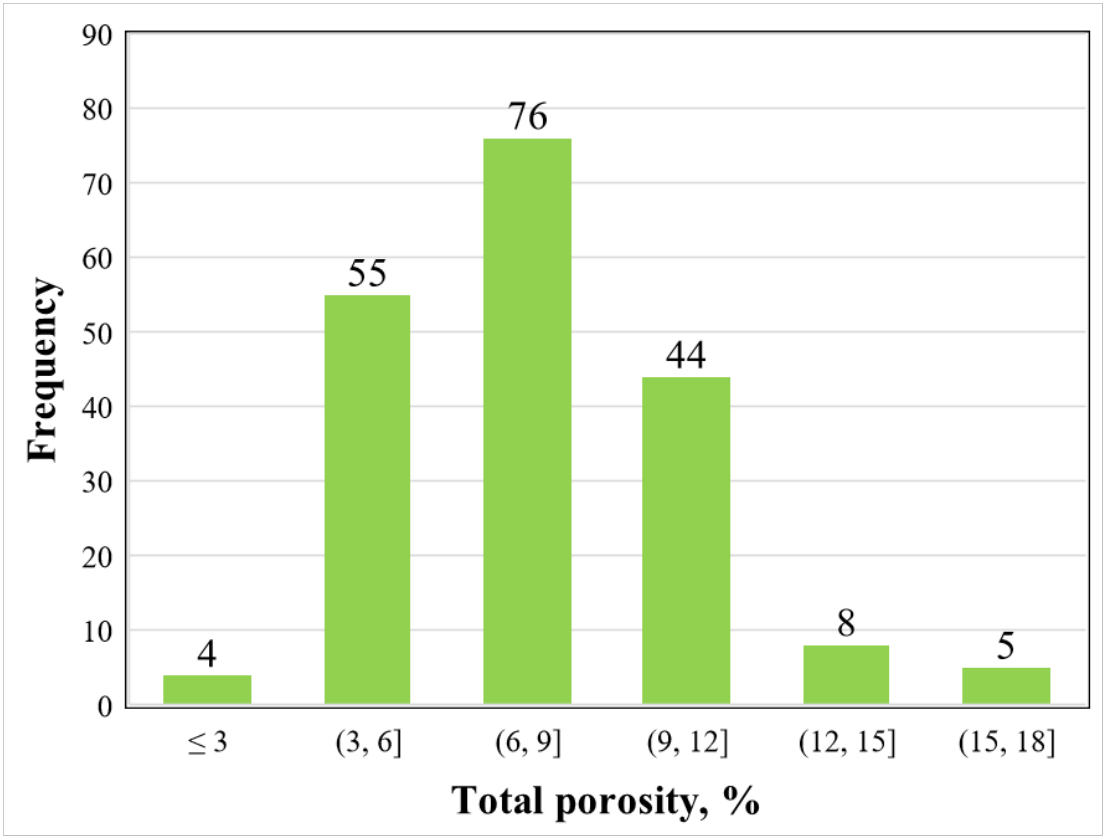


**Figure 16: Total porosity histogram for 192 samples. Total porosity measurements on the core exhibit values from 2.5 to 18%. The average total porosity for the core is 7.6%, with a standard deviation of 2.83.**

**Figure 17** compares total porosity and LPP porosity. In the case of clay-rich samples, both porosity values agree with the difference between the results of the two techniques, about 0.5 % or less. On the other hand, calcite-rich samples can be divided into two clusters. The first one with a difference between the results of less than 0.5 % and the second one with a difference greater

than 1 % (shown in the red circles), which is under the acceptable range. The findings indicate the different origins of the calcite-rich samples in the Uinta Basin. Some samples may have formed from limestone, which accumulated from marine organisms, while others may be evaporites that precipitate from minerals when water evaporates (Earle, 2015). In the case of limestone, water can become trapped during rock formation and remain within the porous system due to the low permeability of the Green River Formation. This can impact the NMR values, potentially leading to overestimating the fluid-in-rock measurements, affecting the total porosity results, and creating a discrepancy between the two techniques. Generally, the total porosity and LPP techniques produce similar results, except for a few calcite-rich samples.

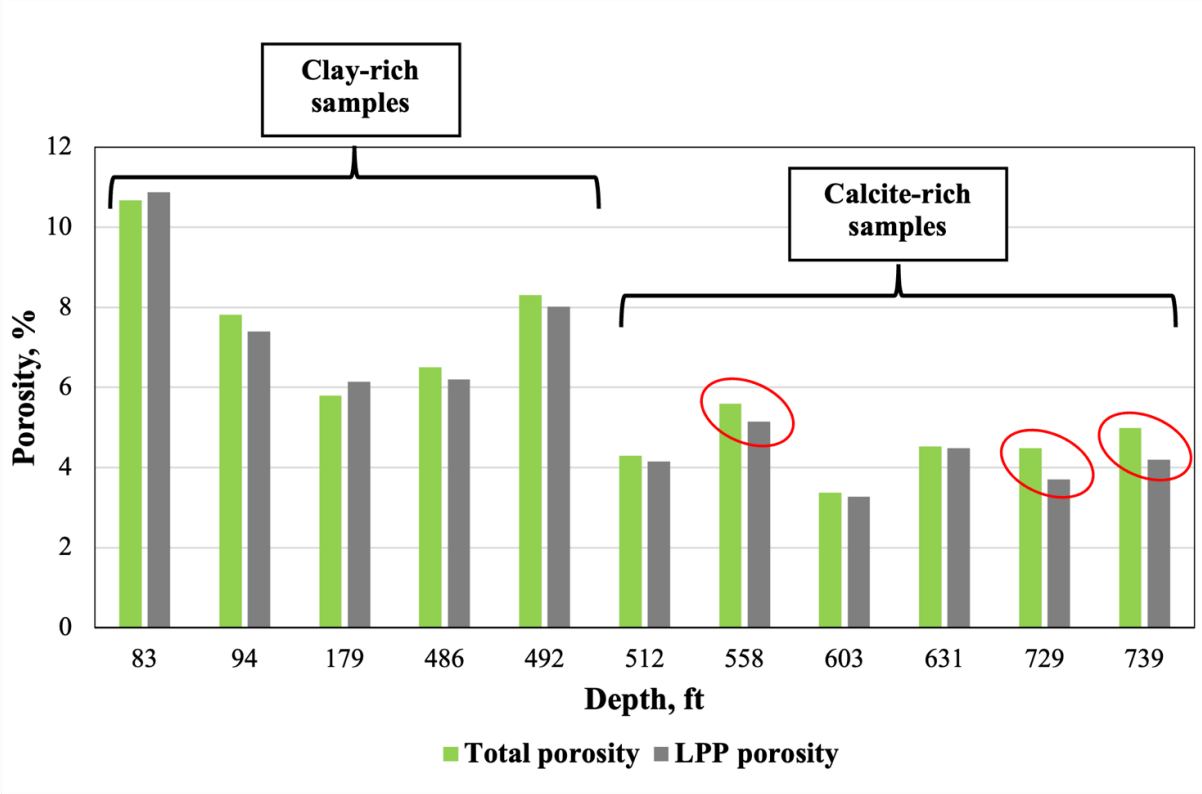


**Figure 17: Comparison between total porosity (HPP+NMR) and LPP porosity results for the Uinta Basin. Red circles indicate calcite-rich samples originated from lithification (limestones).**

## 4.3. FTIR Mineralogy

The FTIR mineral composition profile shows high heterogeneity with depth for the two well intervals. The upper section (**Figure 18**) is rich in clay minerals interbedding with calcite, dolomite, and quartz intervals. High clay content is associated with shale formations. The presence of high concentrations of clay minerals in the Uinta Basin can have several implications. For example, these minerals can affect the pore throat size distribution and total porosity of the rock, which can impact the flow of oil and gas. Clay minerals can also serve as a reservoir for hydrocarbons, and they can provide clues about the history of the basin and the processes that have influenced the formation and migration of oil and gas. The high concentration of quartz in the upper section may indicate the presence of sandstone, which can serve as a reservoir for oil and gas. The quartz matrix provides porosity and permeability for fluid flow.

The lower section (**Figure 19**) has higher calcite and dolomite content than the upper section. The high concentration of calcite in the Uinta Basin may indicate the presence of carbonate rock such as limestone. The high dolomite portions indicate dolostone reservoirs formed when magnesium-rich fluids interact with limestone, replacing some calcium in the limestone with magnesium (Koeshidayatullah et al., 2020).

FTIR mineral concentration agrees with the XRF and LIBS elemental profile. The upper section is rich in silica and aluminum minerals, mainly clays and less frequent quartz-rich portions. On the other hand, the lower section is rich in calcium and magnesium, aligning with the high content of calcite and dolomite.

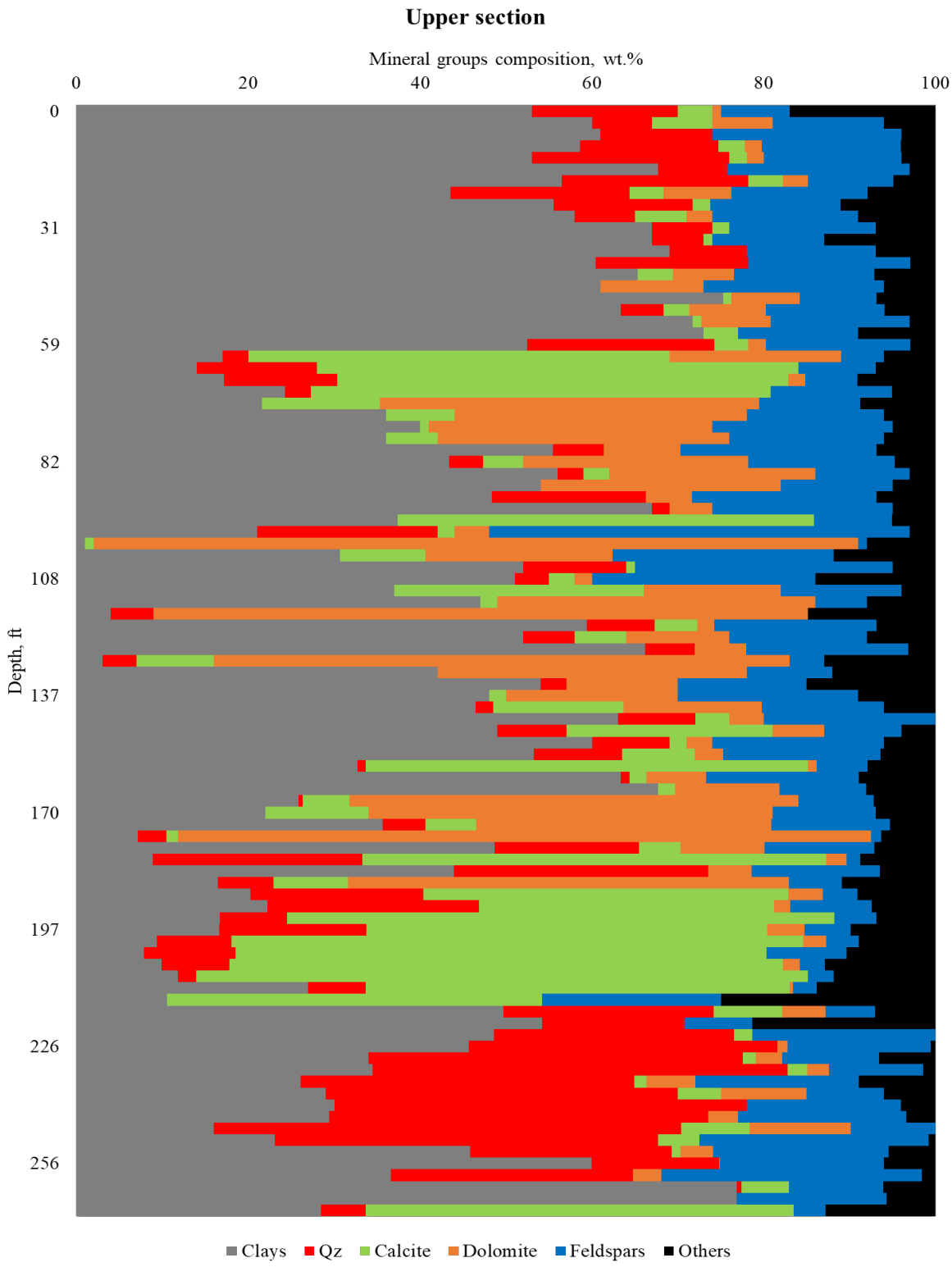


**Figure 18: FTIR Mineral group profile for the upper section of the core material. The upper section is rich in clay minerals. Quartz is significantly high at the bottom portion.**

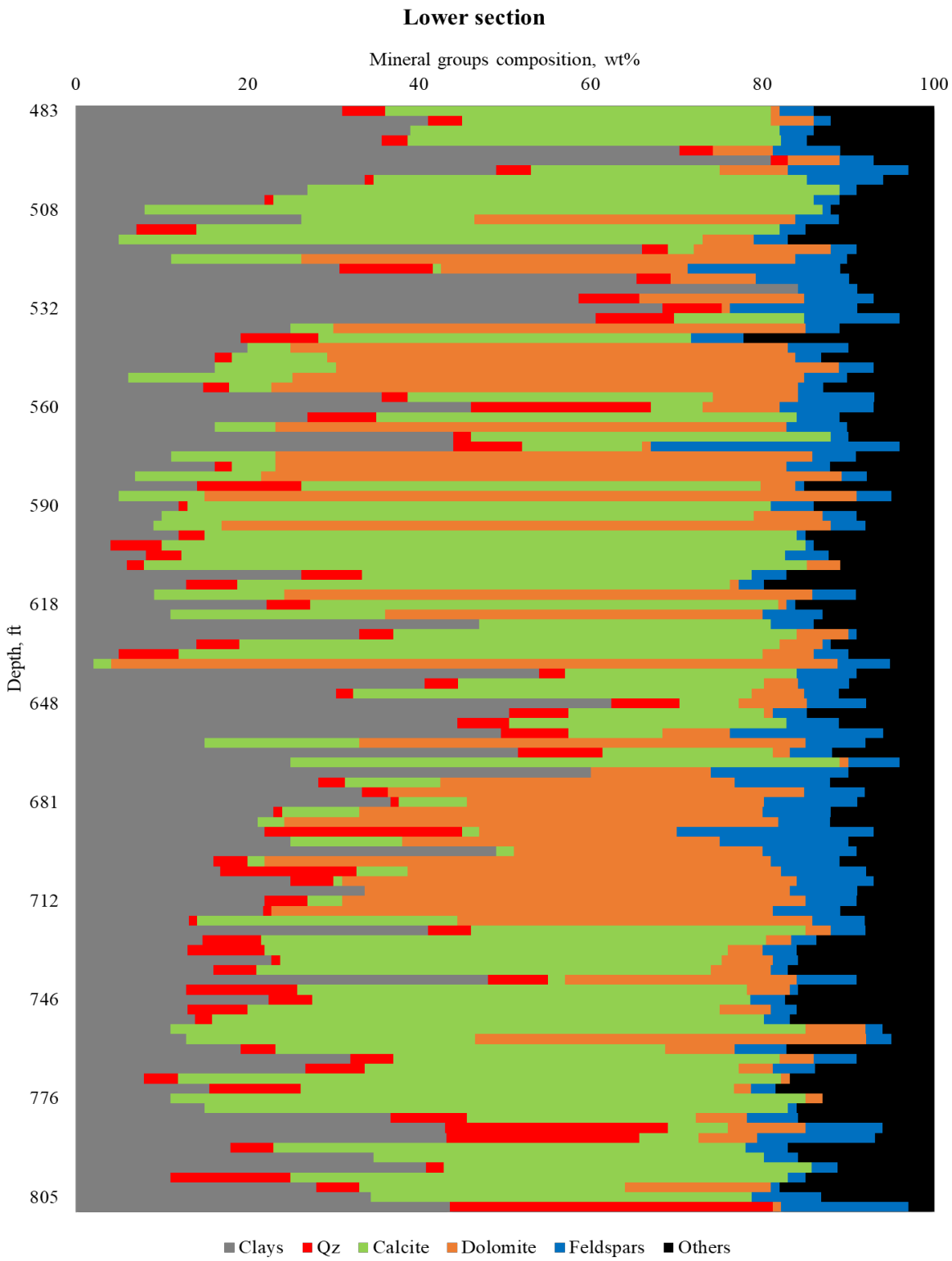


**Figure 19: FTIR mineral group profile for the lower section of the core material. Calcite and dolomite are significantly higher than in the upper section.**

FTIR mineralogy measurement detects clays, carbonates, quartz, feldspars, and other mineral groups. Carbonates include dolomite, calcite, siderite, and aragonite. Others contain minerals such as pyrite and anhydrite. **Figure 20** illustrates the relative distribution of different minerals in the carbonate group, with calcite and dolomite representing the major portion of this group.

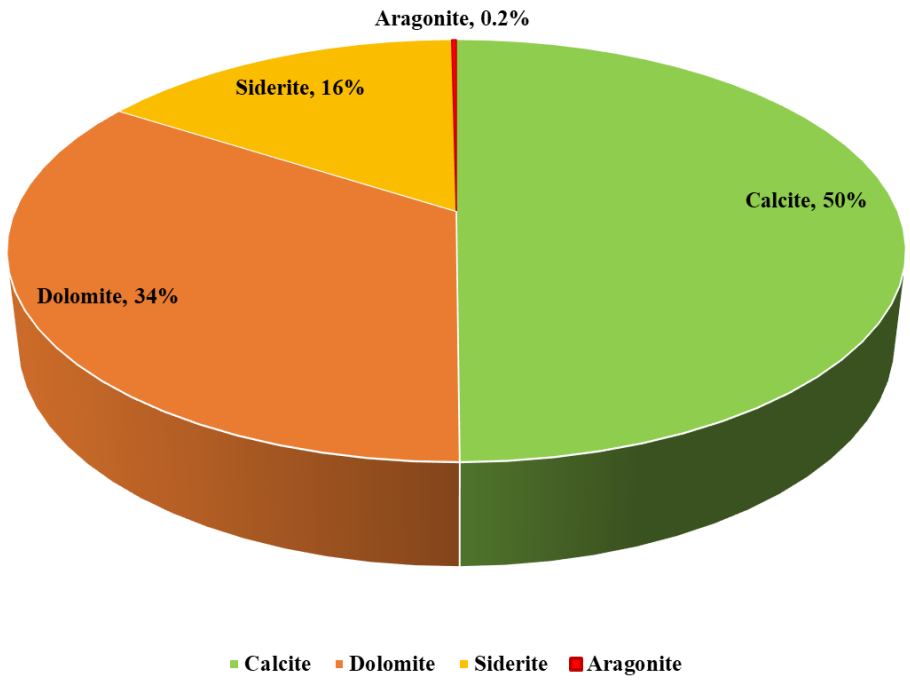


**Figure 20: Break down of carbonate group into different minerals. Calcite is the main carbonate mineral, representing 50% of the total carbonate content.**

The clay mineral group comprises illite, smectite, kaolinite, chlorite, and mixed-layer clays. Illite is the dominant clay mineral in the formation (65%). Illite is associated with sedimentary rocks, especially shales. Illite may precipitate in the pore system of sandstones and carbonates reservoirs restricting the fluid flow, which can affect the total porosity and pore throat size distribution of the formation (Pevear, 199). Kaolinite content is almost null (**Figure 21**).

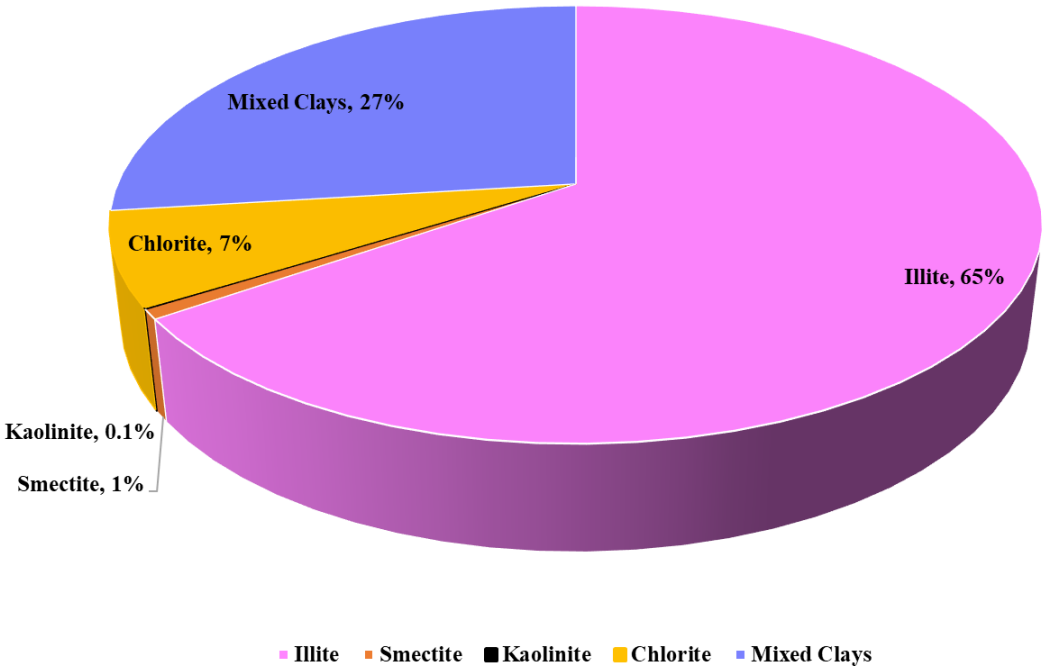


**Figure 21: Distribution of the mineral comprising the clay group. Illite represents 65 % of the whole group in the well.**

Cross-plots visually represent the relationships between various parameters and can help better understand the formation and its characteristics. In the case of the Uinta basin, an inverse relationship between calcite and total porosity is noted in **Figure 22.**

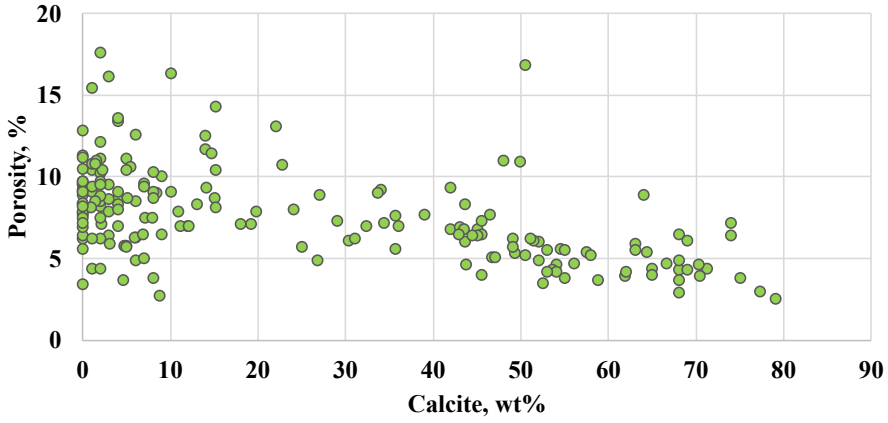


**Figure 22: Total porosity and calcite content show an inverse relationship in the Uinta Basin.**

The relationship between dolomite and total porosity is unclear, **Figure 23.** However, the SEM analysis (see Chapter 5) showed that samples with high dolomite content tend to have well-sorted grains and larger pore throat structures than other samples in the study. In most cases, a weak positive correlation between dolomite content and total porosity is observed when dolomite exceeds 40%, as shown in **Figure 23**.

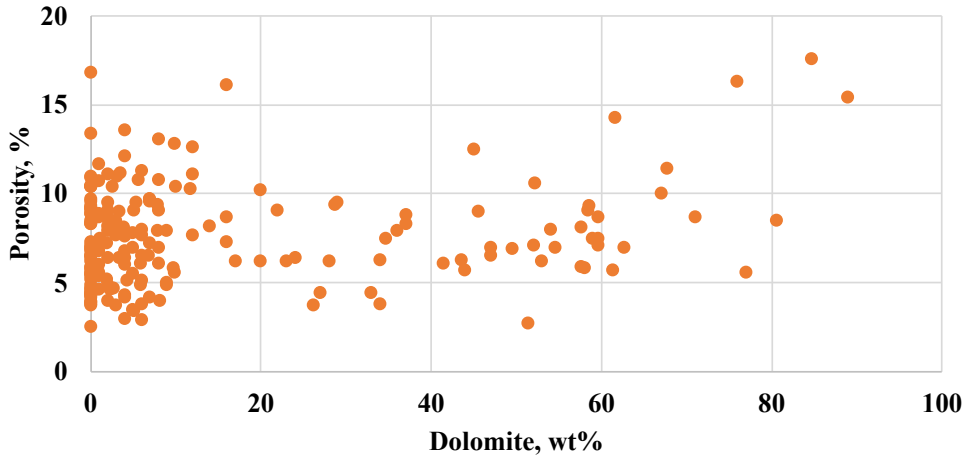


**Figure 23: Total porosity as a function of the dolomite content.**

The analysis also suggests that clay content positively impacts total porosity, with higher clay content generally leading to higher total porosity (**Figure 24**).

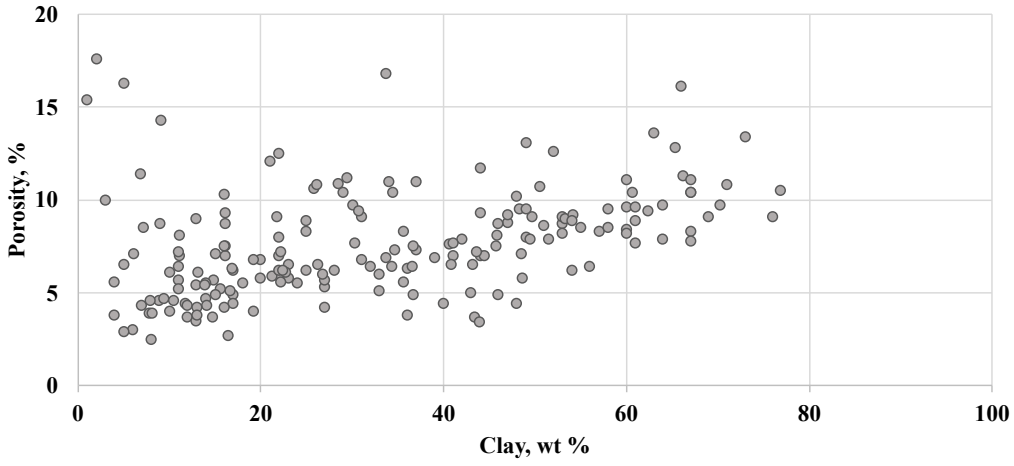


**Figure 24: Positive correlation between total porosity values the clay content.**

## 4.4. TOC and Thermal Maturity

A total of 208 Rock-Eval measurements were carried out in this study to characterize parameters such as TOC, S1, S2, and Tmax (thermal maturity). The results for TOC, S1, and S2 are presented in **Figures 25, 26**, and **27**, respectively.

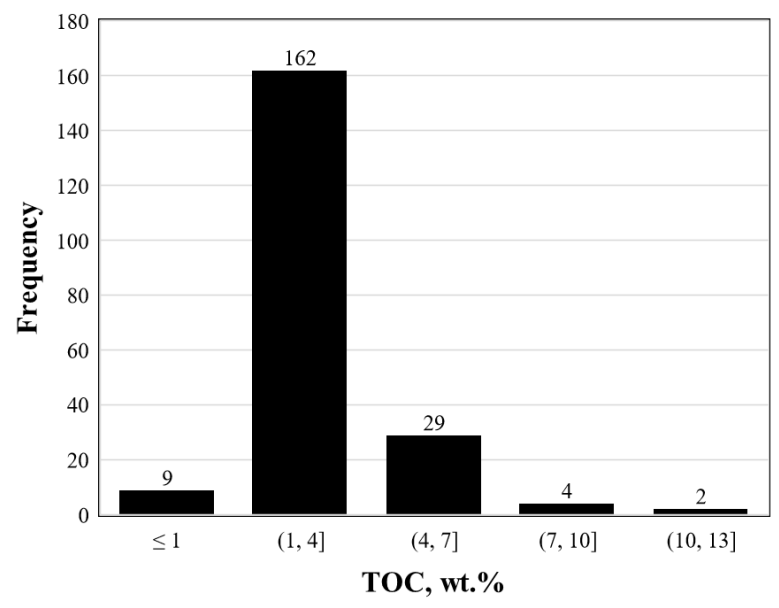


**Figure 25: TOC histogram for 208 samples from the Uinta basin formation. TOC varies from 0.5 to 11 %, (+/-1.3).**

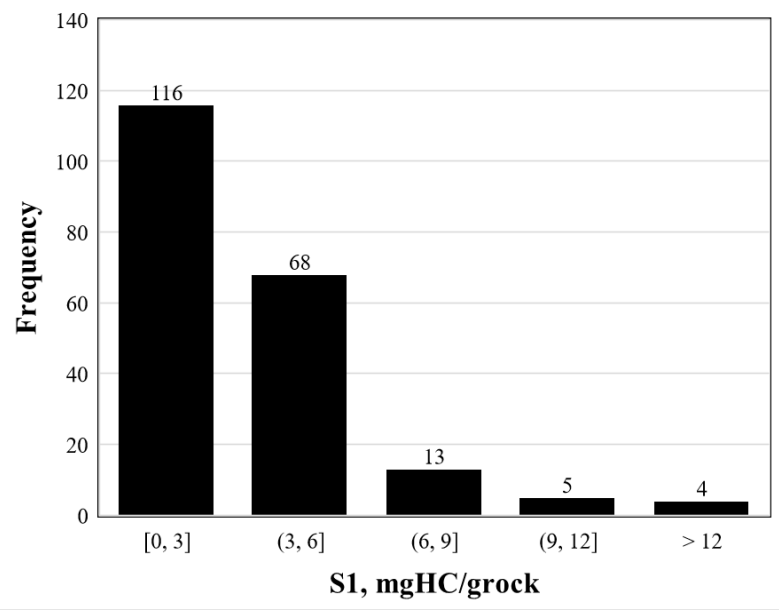


**Figure 26: Histogram of S1. The average value of S1 is 3.2 mgHC/grock (+/-3.2).**

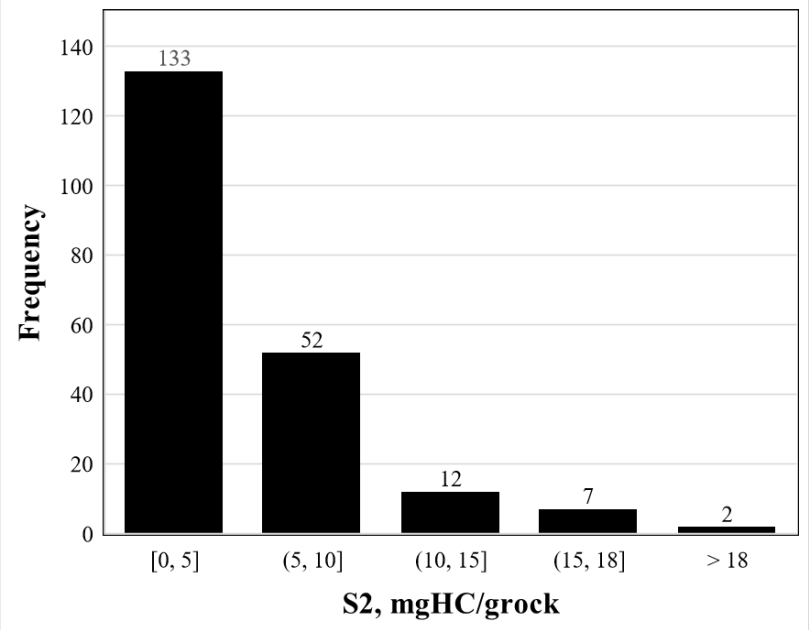


**Figure 27: Histogram of S2. The average value of S2 is 4.9 mgHC/grock (+/- 3.5).**

**Table 1** shows the average values of the SRA parameters:

| Parameter | Average |
|---|---|
| **TOC** | 2.8 |
| **S1** | 3.2 |
| **S2** | 4.9 |
| **Tmax** | 442 |

**Table 1. TOC, S1, S2, and thermal maturity average data for the well. TOC in wt %, S1 and S2 in mg HC/rock, and Tmax in °C.**

Most samples showed TOC values between 2-4, averaging 2.8 wt.% indicating good to very good hydrocarbon generation potential (Law, 1999). $S_2$ values suggest that the formation can be classified as fair source potential with values ranging mainly from 2-5 averaging 4.9 wt. %

(Espitalie, 1982). Regarding Tmax, most samples lie in the oil window maturity (type II kerogen) (Espitalie et al., 1997; Espitalie, 1982; Espitalie et al., 1984, Espitalie et al., 1985, Law, 1999).

**Figure 28** shows TOC, S1, S2, and Tmax as a function of depth (from left to right). TOC tends to be uniform throughout the two intervals; however, it is slightly higher in the upper section, which matches the higher clay content. On the other hand, the lower section, which is carbonate-rich, shows lower values on average.

High values of S1 and S2 are associated with clay-rich rocks that match the high clay content intervals, indicating shale formation. On the other hand, low S1 and S2 values seem to fit with quartz-rich intervals, suggesting sandstone intervals. The carbonate-rich sections interbedded with clay-rich layers may exhibit higher S1 and S2 values due to the higher organic matter input and preservation, which is the case for this study. High TOC values can be associated with high sulfur content, particularly in shale formations. In this case, high values in the middle of the upper section seem to be related to the high sulfur content from XRF and LIBS.

Clay-rich intervals tend to have higher Tmax than quartz- or carbonate-rich ones (Kivi et al., 2017; Vafaie et al., 2015; Wu et al., 2018). This agrees with what we observe; the upper section of the core material, which has higher clay content as compared to the lower section, also has higher Tmax. Quartz-rich rocks tend to have lower thermal conductivities in comparison, which can result in slower heating rates and a delay in the onset of thermal maturation. In the same way, calcite and dolomite can act as thermal sinks, absorbing heat and limiting the degree of thermal maturation that occurs (Robertson, 1988).

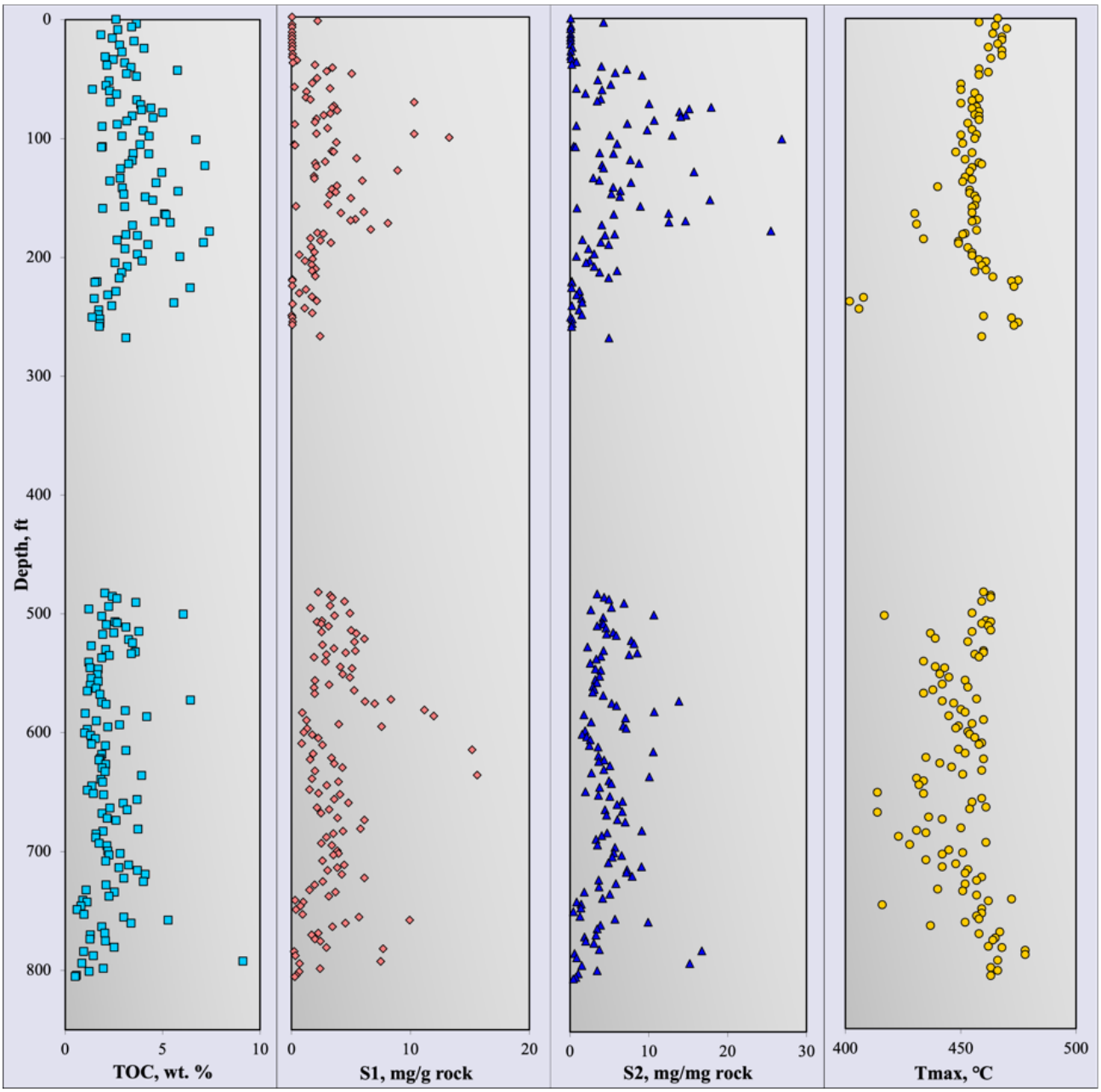


**Figure 28: TOC, S1, S1, and Tmax as a function of depth.**

## 4.5. Mercury Injection Capillary Pressure Measurement

**Figure 29** displays the incremental Hg injection volume curves for different samples in the formation. The curve shape indicates the level of sorting and the pore throat size distribution in

the samples. Sorting refers to the degree to which the pore throat sizes in a sample are similar or different. A well-sorted sample will have a narrow range of pore throat sizes, while a poorly sorted sample will have a broader spectrum. The pore throat sizes control the shape of the intrusion curve. The intrusion starts at a lower pressure in samples with large pore throats, whereas it occurs at a higher pressure in tight samples. Both sorting and pore throat sizes are affected by various factors such as dispositional environment, diagenesis, and pore-filling minerals.

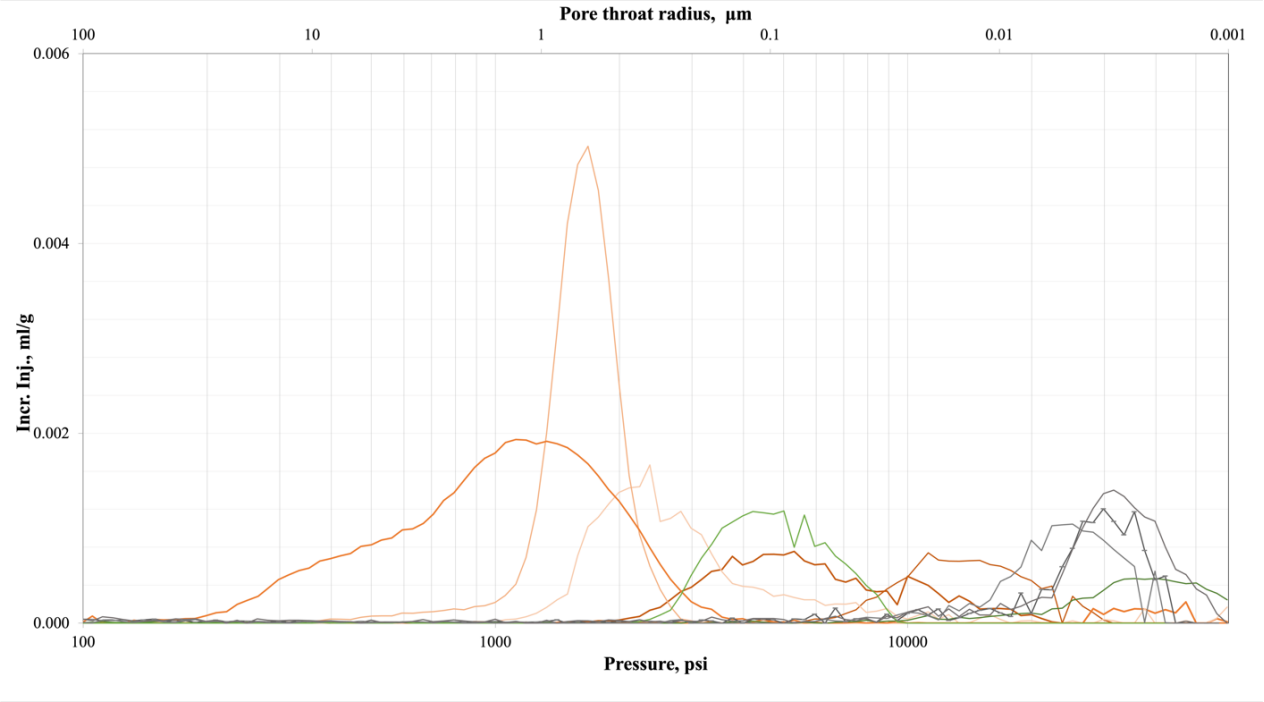


**Figure 29: MICP incremental Hg intrusion curves show the pore throat size distribution for different samples in the well. It indicates the heterogeneity of the Uinta basin.**

**Figure 30** shows MICP data for the dolomite-rich (>50%) and high total porosity (>10%) samples. The Hg intrusion begins at lower pressures, indicating big pore throats. Big pore throats generally have better connectivity which is important for fluid flow in reservoir rocks. However, samples with high dolomite and low total porosity (< 6%) show small pore throats. This difference

can be attributed to the heterogeneity of the Uinta Basin and the different factors that control the rock formation. Narrow and broad distribution are associated with dolomite-rich samples.

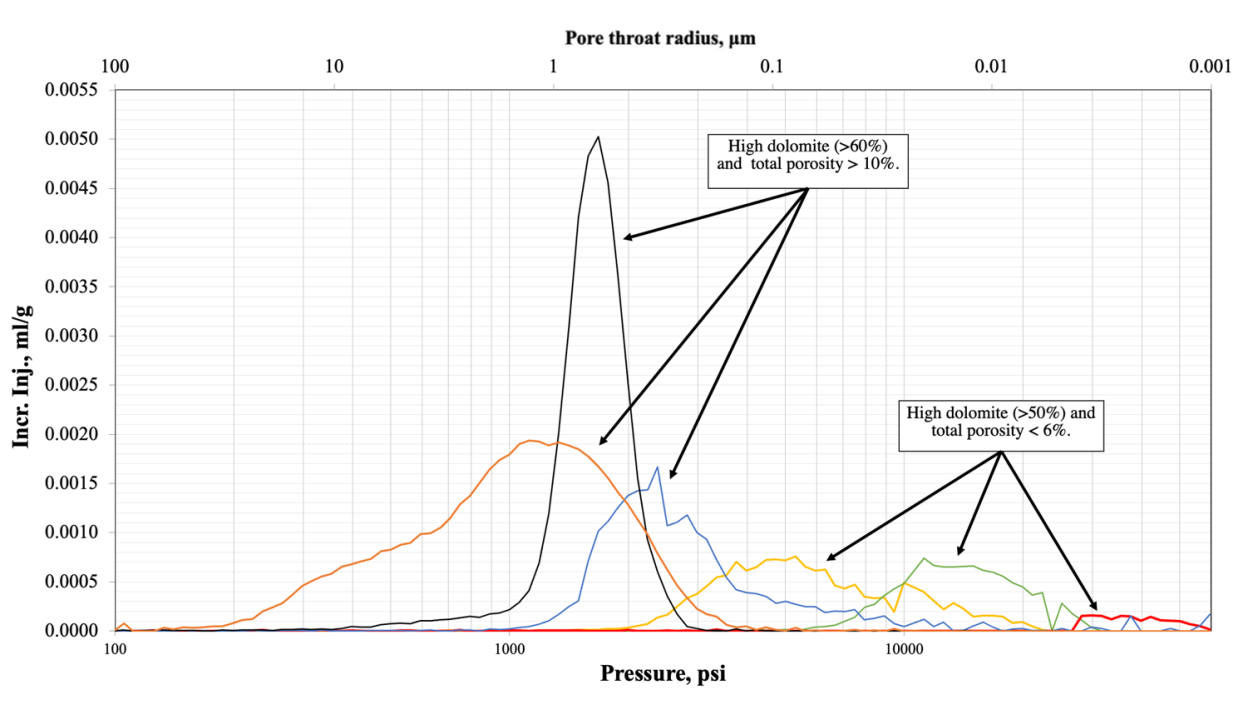


**Figure 30: Hg incremental curves for high dolomite samples (>50%).**

These high dolomite intervals are known as dolomite veins. They can provide pathways for the fluid to flow and for mineral precipitation to occur depending on their size, orientation, and crystal shape, resulting in an increase or having no effect on the pore throat size distribution (Kopaska-Merkel et al., 1994; Ehrenberg, 2004; Wendte et al., 2009; Maliva et al., 2011; Nabawy, 2013; Widodo and Laya, 2017; Tavakoli, 2021). The dolomitized zones tend to have larger pore throats when the dolomite concentration is more than 50%, and a connected intercrystalline pore system is formed through the rock, which can result in pathways for fluids (Tucker and Wright, 1990; Bouch et al., 2004; Machel, 2004; Wang et al., 2015; Tavakoli and Jamalian, 2019; Tavakoli, 2021). However, some studies show that dolomitization did not significantly affect total porosity

or the pore throat size distribution (Halley and Schmoker, 1983; Lucia and Major, 1994; Hood et al., 2004; Lucia, 2004).

**Figure 31** shows the Hg incremental curves for the high quartz samples (>40%). Most of these samples show a bimodal pore throat size distribution Sandstones are generally considered to have larger pores than rocks such as shale. In this case, the small pore throats can be related to the significant presence of clay minerals in these samples, that result in bimodal distribution seen in **Figure 31**. The pore throats associated with the quartz are better sorted than those associated with the clays, showing narrow shapes compared to the broader shape for the clay-rich pore throats.

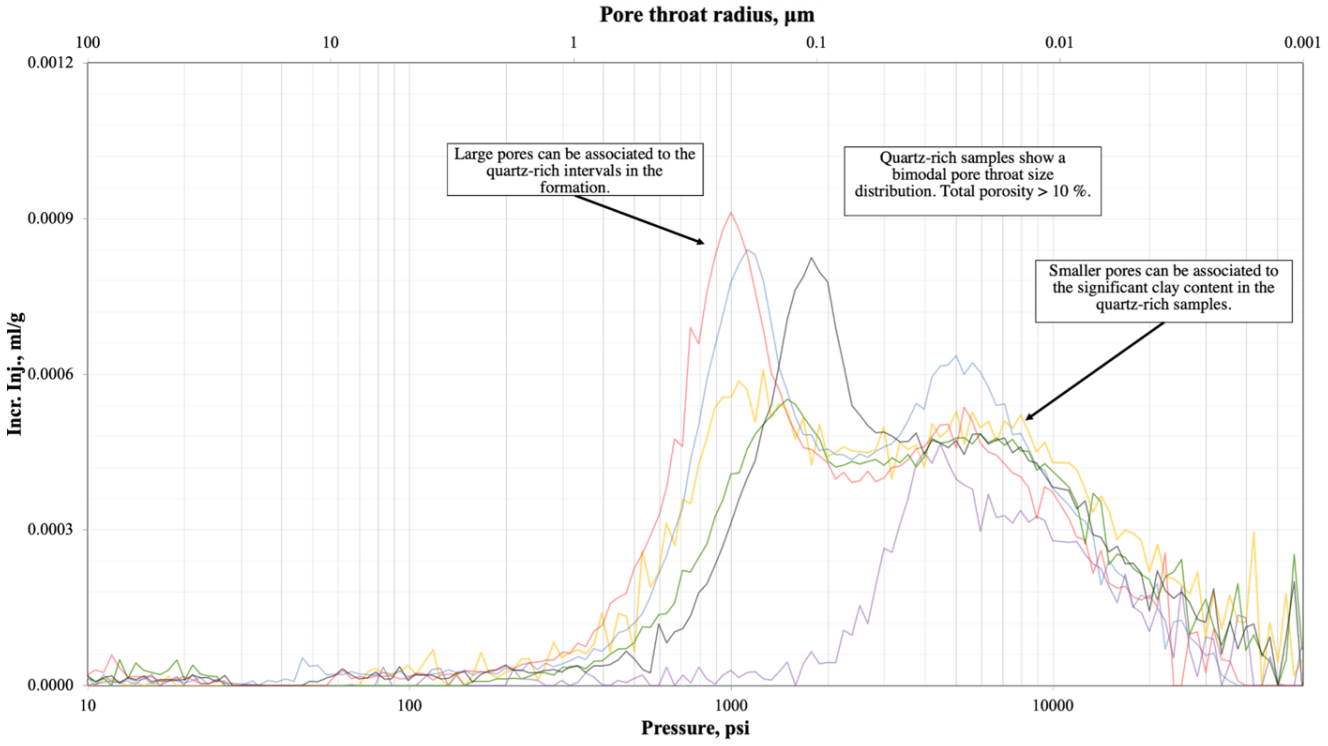


**Figure 31: Hg incremental curves as a function of pressure for high quartz samples (>40%).**

**Figure 32** exhibits clay-rich samples. The samples show a narrow distribution, and the Hg intrusion begins at high pressures, indicating small pore throats. The small pore throats, high TOC, and high total porosity could indicate that the clay-rich intervals act as the source rock in the formation.

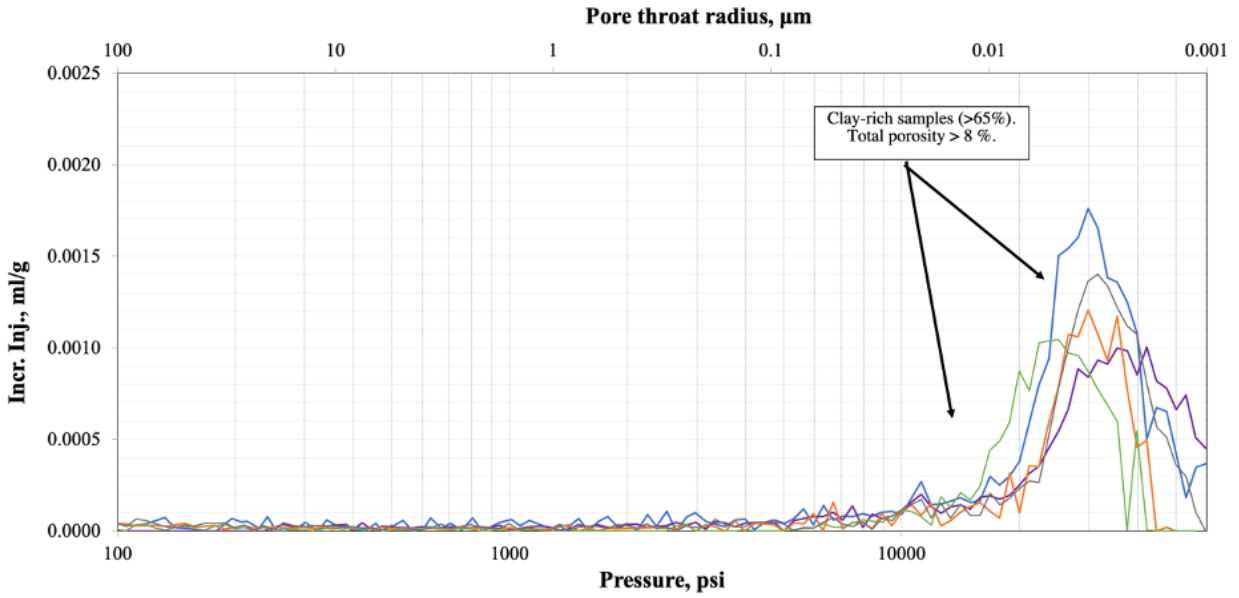


**Figure 32: Hg incremental curves as a function of pressure for the clay-rich samples (>65%).**

**Figure 33** displays the curve shapes and peaks for samples with high calcite content (>65%), indicating narrow and broad shapes and a tendency to small pore throats. Previous results showed that total porosity decreases as a function of the calcite concentration. When calcite precipitation occurs, it can clog or reduce the size of the larger pores creating smaller pore throats, leading to a decrease in total porosity and pore throat sizes and an increase in the heterogeneity of the rock.

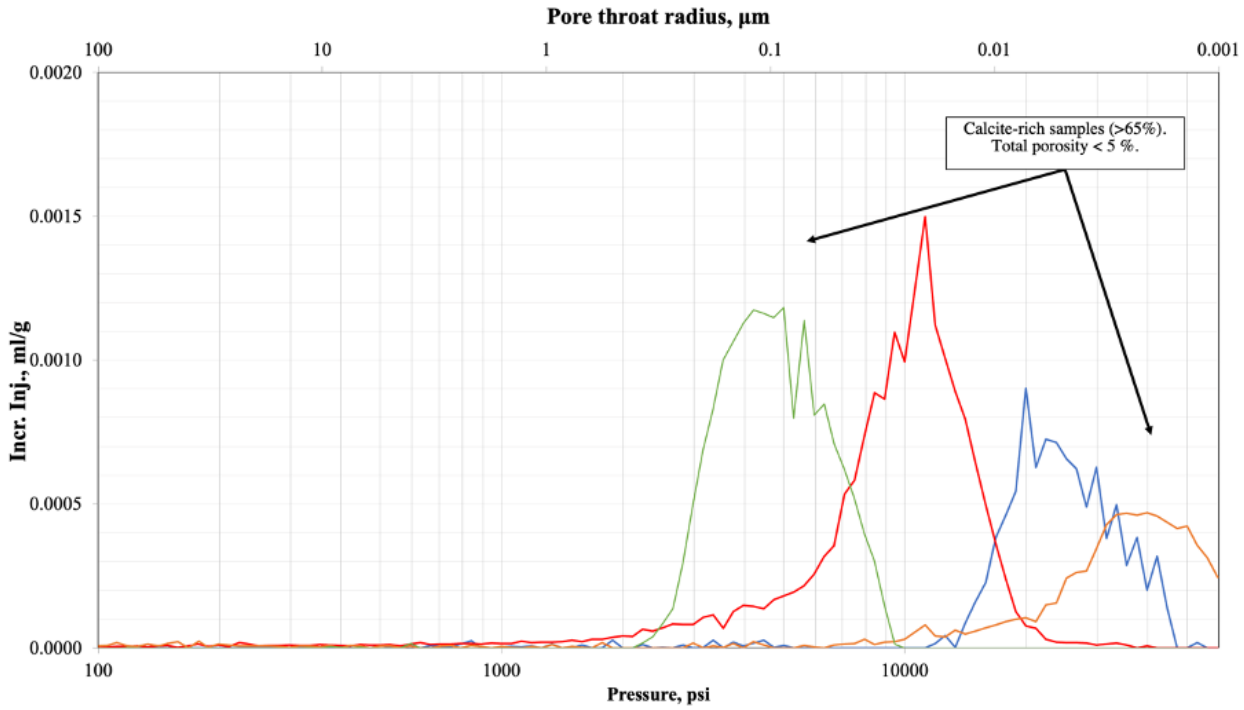


**Figure 33: Hg incremental curves as a function of pressure for the calcite-rich samples (>65%).**

In conclusion, the MICP incremental Hg intrusion curves offer valuable insights into the pore throat size distribution, sorting, and heterogeneity of the Uinta Basin. The shape of the intrusion curve is influenced by various factors such as depositional environment, diagenesis, and pore-filling minerals that affect the pore throat size and sorting. Dolomite-rich samples with high total porosity generally have larger and connected intercrystalline pore systems that serve as pathways for fluid flow. High quartz samples show a bimodal pore throat size distribution with better-sorted and larger pore throats associated with quartz, while clay-rich samples tend to have small pore throats. Calcite-rich samples tend towards small pore throats, decreasing total porosity and pore throat sizes and increasing rock heterogeneity due to clay precipitation. These findings emphasize the importance of understanding the pore structure of reservoir rocks to predict fluid flow and evaluate the potential for hydrocarbon exploration and production.

## 4.6. Chemostratigraphy

Chemostratigraphy is a reservoir correlation technique that utilizes inorganic geochemical data to characterize and correlate sedimentary rocks. The basic principle identifies chemostratigraphy zones or units with unique geochemical features (Ramkumar et al. 2015).

The chemo-facies are defined using elemental data from the XRF technique. Core elements indicated major lithologic patterns, such as mixed clastic and carbonate siltstone/mudstone and shale. The elements Al, K, Ti, Zr, Sr, Ca, Fe, Cu, Zn, Pb, S, Mg, and Si and the elemental ratios Sr/Ca, Si/Ti, Si/Al, Ca/Mg, and Zr/Nb were used to define the chemofacies in this analysis. PCA was used to establish five principal components, and K-means was used to cluster the principal components into three groups representing each chemofacies. Al and K represent the clay content, while Ti and Zr signify the continental-derived sediments (Sageman and Lyons, 2004; Tribovillard et al., 2006). Ca and Sr are indicators of carbonates, and the Sr/Ca ratio shows the degree of diagenesis (Banner, 1995; Hardisty et al., 2021). The Si/Al ratio represents sand/clay concentration in mixed beds. Ca and Mg levels suggest the carbonate zones, and high Ca/Mg peaks indicate a calcite-rich section in a moderately constant calcite/dolomite content (Wu et al., 2015).

**Figures 34** and **35** show the chemostratigraphy profile from the Uinta basin well in this study. **Figure 34** displays the elemental concentration for both intervals and the associated chemofacies. **Figure 35** shows the ratio between the elements that can help to identify the chemofacies.

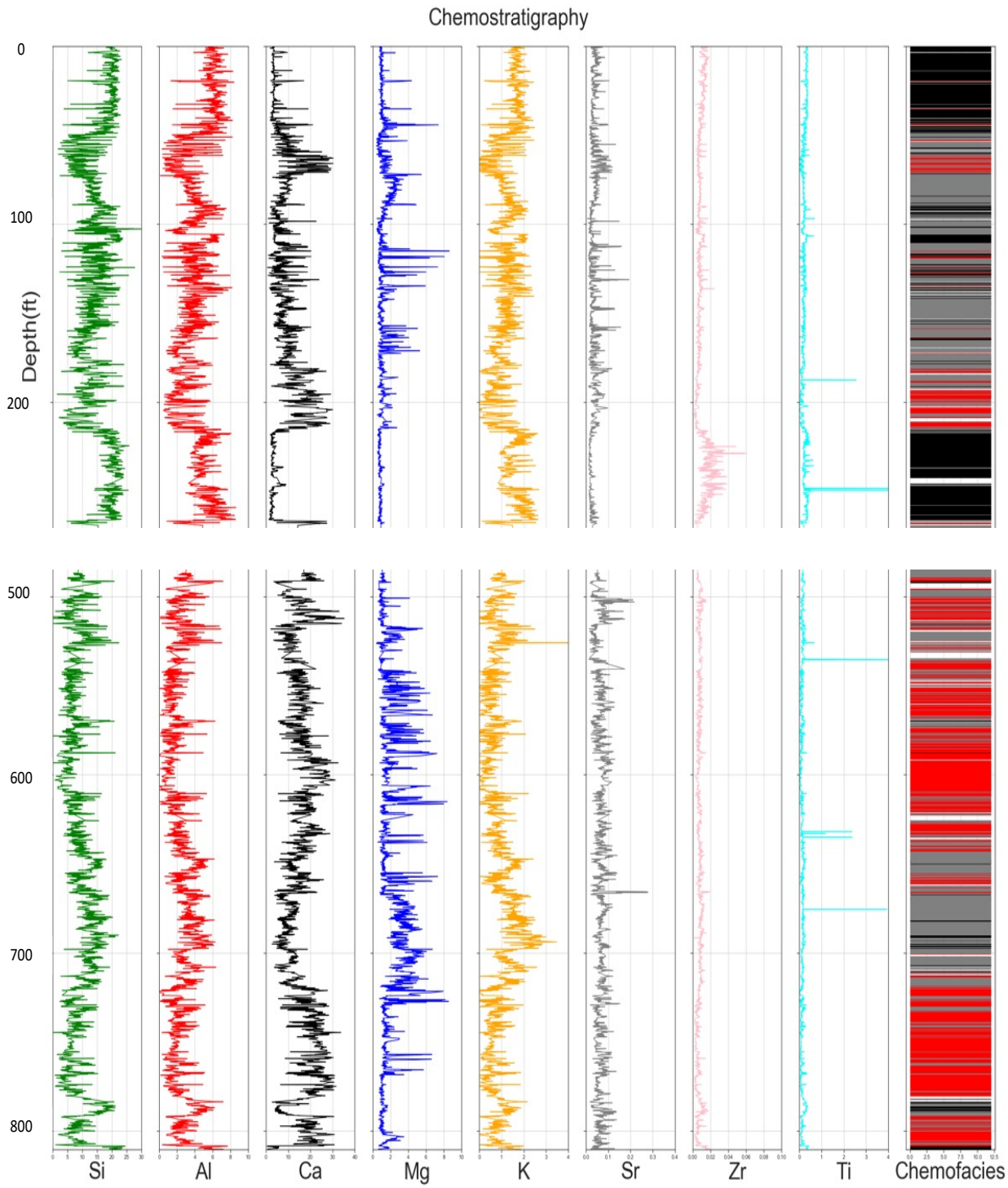


**Figure 34: Chemostratigraphic profile showing the elemental concentration through the two intervals.**

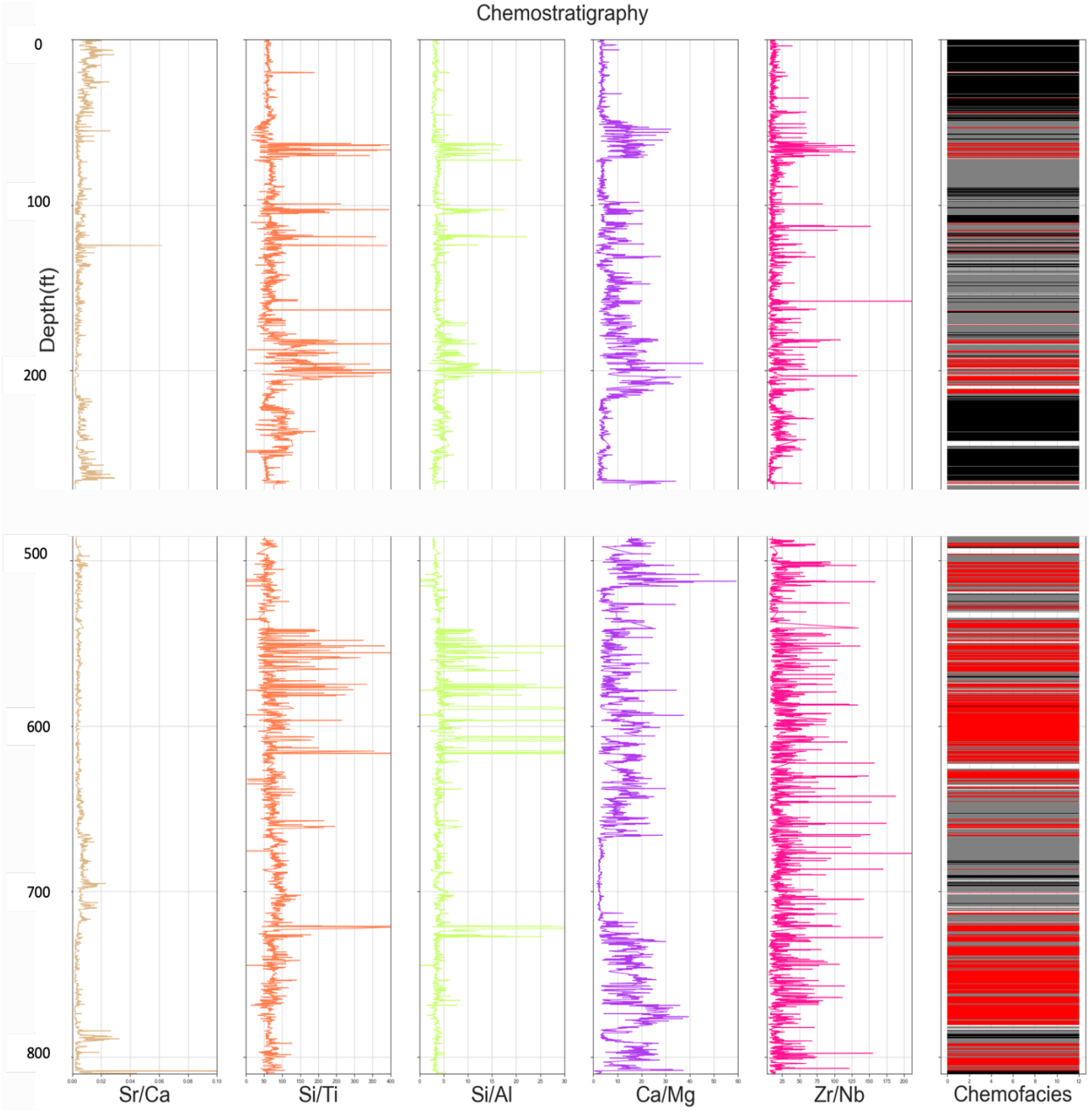


**Figure 35: Chemostratigraphy profile showing chemofacies and mineral ratios that allow identifying the chemofacies in the formation.**

The Uinta Basin consists of three lithofacies (Fouch, 1992), the alluvial, the marginal lacustrine, and the open lacustrine, which can be related to the chemofacies in the sedimentary rocks. The term "chemofacies" refers to the characteristic geochemical signatures of different sedimentary rock types, which can be used to infer the depositional environment and processes

that formed them. The presence or absence of certain elements and their relative abundances can provide insights for classification.

**Figure 36** shows the scatterplot of the three chemofacies defined in this study. Chemofacies 1 (in black) has a high level of aluminum and silica and low levels of calcium, magnesium, and strontium. Heavy metals such as lead, zinc, and copper are presented in relatively high concentrations. This indicates that it was formed in a fluvial environment where erosion and transport of silicate minerals contributed to the sediment composition. Also, Si/Al and Si/Ti ratios are high in these zones, representing the presence of quartz within the sediment (Pearce and Jarvis, 1992; Pearce et al., 1999; Tribovillard et al., 2006; Turner et al., 2015). Chemofacies 1 likely correspond to the alluvial facies.

Chemofacies 2 (in red) may be the open lacustrine facie, characterized by moderate to high levels of calcium and strontium and relatively low levels of aluminum, iron, and silicon. Chemofacies 2 has a higher Ca/Mg ratio than chemofacies 3, indicating that it is rich in calcite (Wu et al., 2015). Chemofacies 3 (in gray) could be the marginal lacustrine facies, which typically have a higher level of aluminum, iron, and silicon and a lower calcium level than the open lacustrine facie.

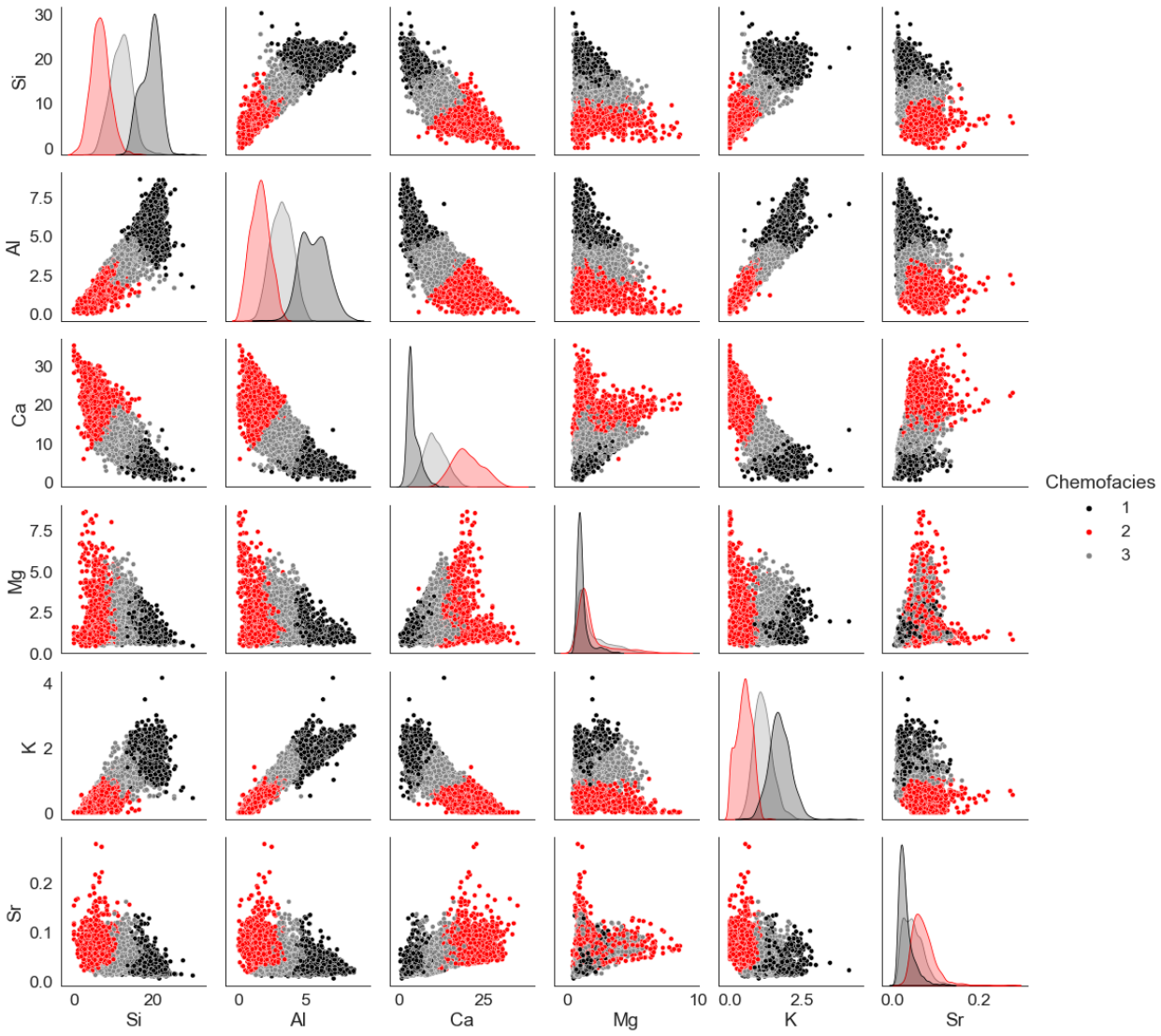


**Figure 36. Scatterplot of the three chemofacies defined in this study. It shows the elements that mainly constitute the chemofacies.**

## 4.7. Core-derived Rock Typing

The petrophysical properties data of the Uinta basin core were thoroughly described, analyzed, and cleaned. These properties included mineral content such as clay, carbonates, feldspars, and quartz, as well as total porosity, TOC, S1, S2, and Tmax. **Figure 37** displays the box plots for some of the petrophysical properties analyzed in this work.

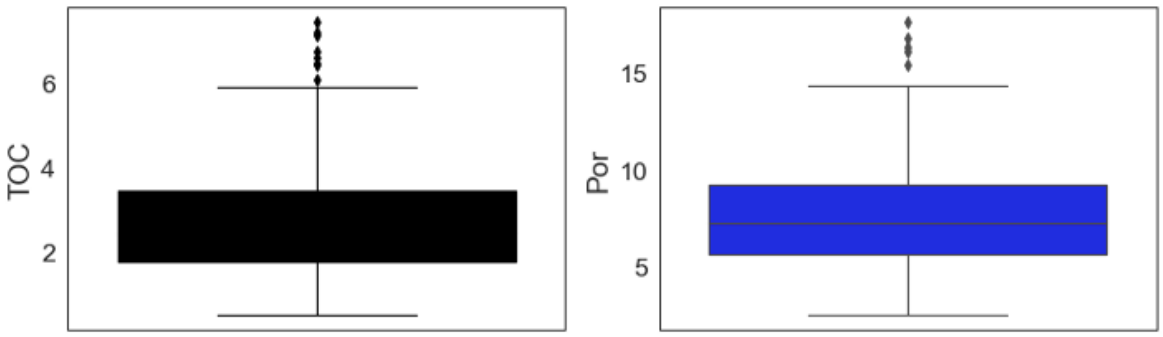


**Figure 37: Boxplots of TOC and total porosity, showing the average value of each property and the outliers.**

The PCA (Principal Component Analysis) algorithm was performed on the petrophysical properties (clay, carbonates, feldspars, and quartz, as well as total porosity, TOC, S1, S2, and Tmax) to decrease the dimensionality for the rock typing. **Figure 38** exhibits that only the five principal components are needed since they explain more than 80% of the variance in the dataset.

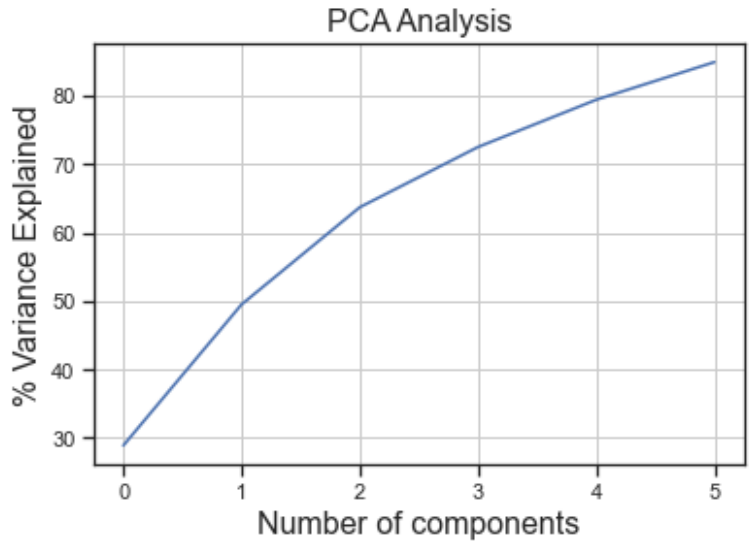


**Figure 38: Principal Component Analysis results.**

SSW method was used to determine the ideal number of clusters for the dataset. **Figure 39** illustrates the SSW results, which show the optimal value between 3 and 4.

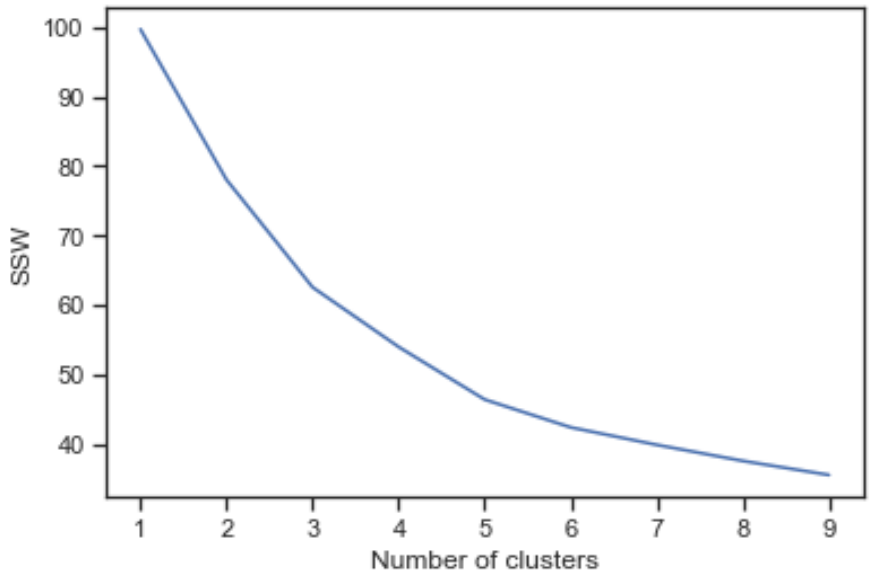


**Figure 39: The optimal number of clusters by implementing SSW. The method identifies that for the data available, three groups are optimal to describe the characteristics of the dataset.**

The k-means clustering technique defined three rock types in the formation, labeled here as RT1, RT2, and RT3. The relative contributions of the rock types 1, 2, and 3 are 37, 42, and 21 %, respectively (**Figure 40**). Each defined rock type has unique petrophysical characteristics such as total porosity, mineralogy, and hydrocarbon generation potential. The total organic carbon embodies the source rock potential of hydrocarbons in the formation. Total porosity is a direct measure of the rock storage capability and can be impacted by the grain size and sorting level. The mineral composition determines the level of brittleness or ductility through a high concentration of either quartz or clay. These petrophysical parameters affect the reservoir performance and well productivity. The characteristics that influence storage and source potential for each rock type in the Uinta group are highlighted (**Figure 41**).

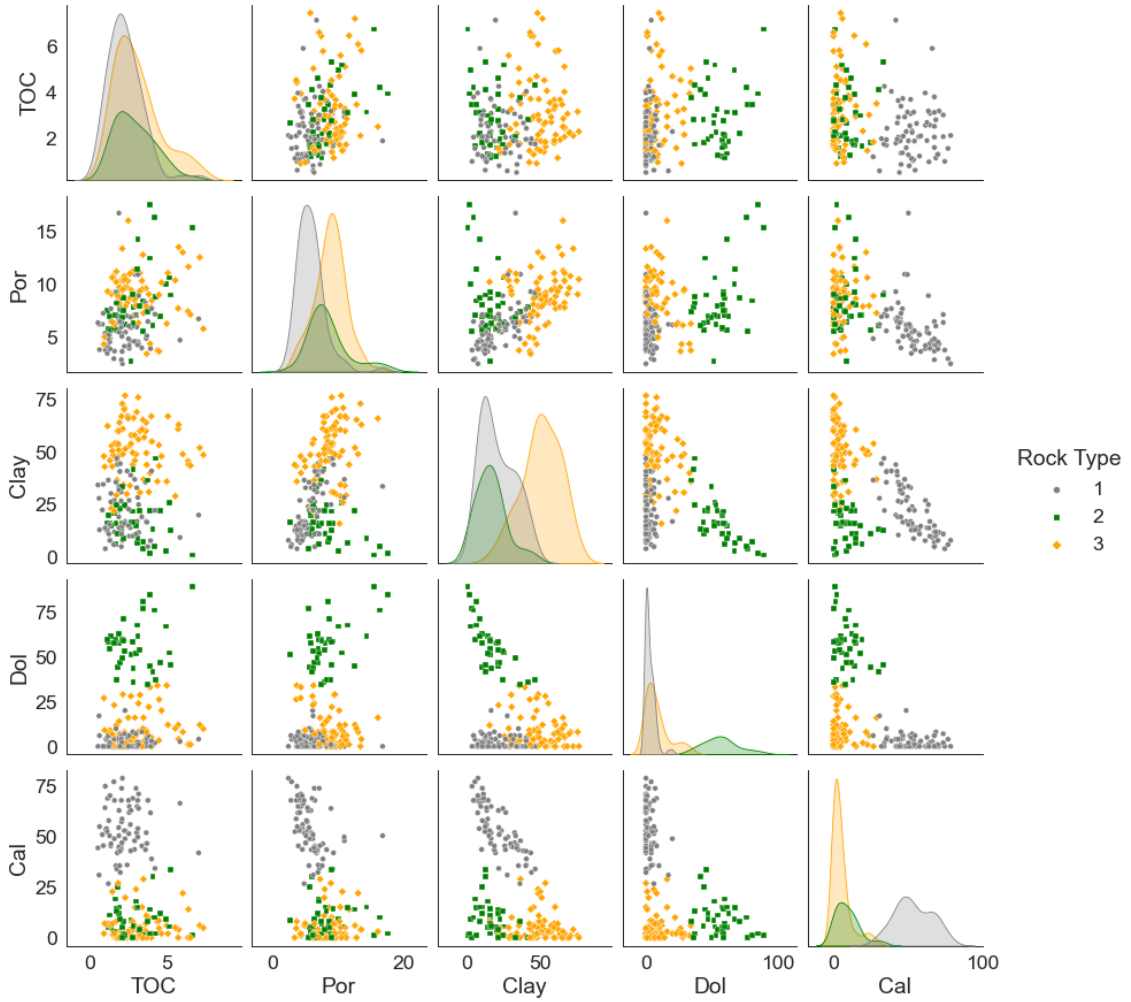


**Figure 40: Scatterplot of the three rock types. It shows the petrophysical properties of each rock type.**

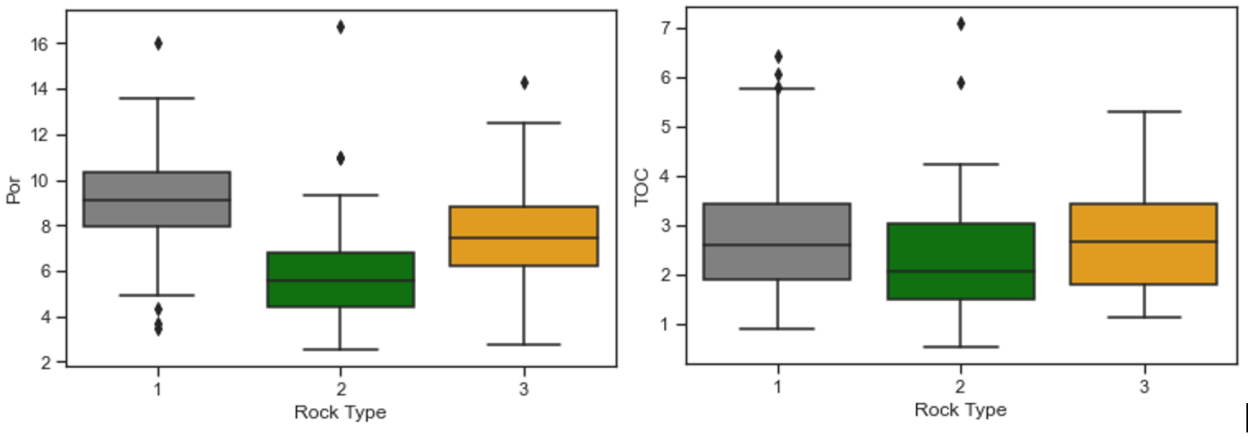


**Figure 41: Parameters governing storage and source potential in the Uinta group. Total porosity in % units and TOC in wt.%.**

RT1 has higher total porosity and hydrocarbon source potential than the other rock types. RT2, on the other hand, has the lowest total porosity and lowest total organic carbon (TOC). **Figure 42** illustrates the average mineral composition of the three rock types in the study area—RT1-siliceous rich, RT2-calcite rich, and RT3-dolomite rich. RT1 dominantly occupies the top section of the core, and most of the bottom section is carbonate-rich rock types, in which calcite-rich and dolomite-rich layers are interbedded. RT1 can be associated with chemofacies 1, RT2 with chemofacies 2, and RT3 with chemofacies 3.

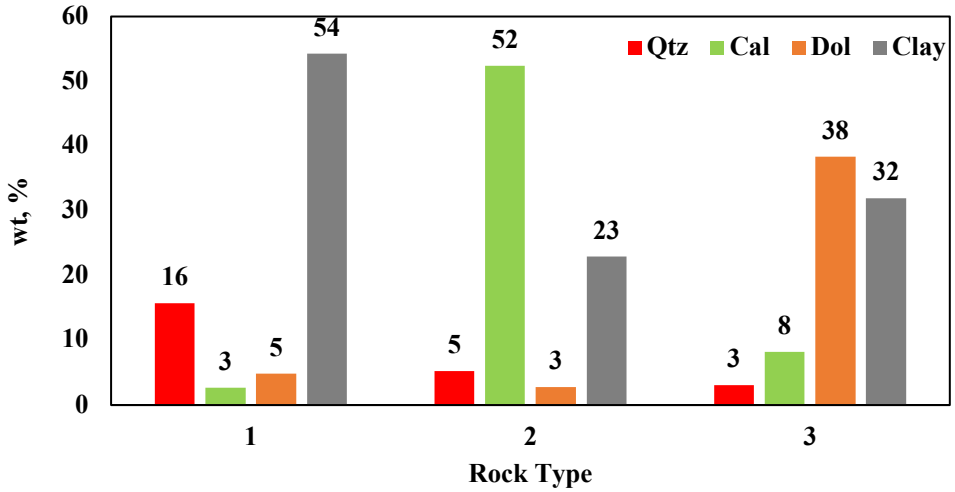


**Figure 42: Average mineral content for three different rock types in the Uinta Basin.**

The rock brittleness, which indicates favorable zones for fracturing (Wang and Gayle, 2009; Li et al., 2013), can be calculated from the mineral profiles of the rock type using **Equation 3** (Wang & Gale, 2009). RT2 is the least brittle due to its low quartz and dolomite content. RT3 has the highest dolomite content and is the most brittle. RT1, on the other hand, has a high concentration of clay, but the quartz content is also considerably high (**Figure 43**).

$$BI_{Wang\ and\ Gale\ (2009)} = \frac{Qz+Dol}{Qz+Ca+Cly+Dol} \qquad \textbf{(1)}$$

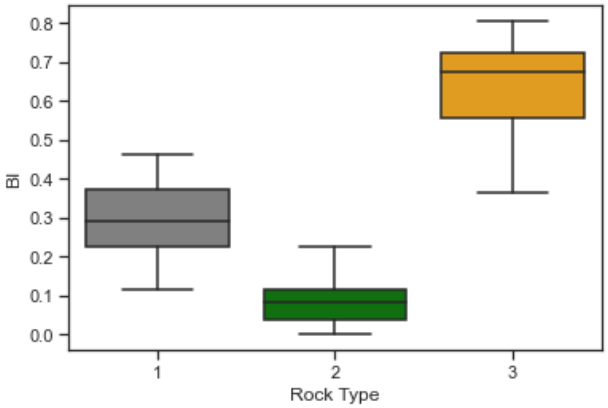


**Figure 43: Brittleness of the three rock types calculated using Equation 3.**

Following the work done by Kale (2010), MICP incremental and cumulative data were normalized using HPP porosity (connected pore volume). MICP data revealed three dominant patterns associated with specific rock types.

Samples identified as RT2 tend to have less intrusion aligning with the high calcite. The extrusion curves for the RT2 samples show that the Hg is trapped in the pore system due to the small pore throat sizes in the samples. RT3 samples are better sorted and have bigger pore throats with the Hg intrusion starting at a lower pressure than other rock types since high dolomite and high total porosity samples tended towards larger pore throats. The presence of clays indicates small pore throat sizes, as **Figure 44** displays. It aligns with the SEM results, having the microstructure confirming this statement. RT1 samples have smaller pore throats than RT3.

Based on the results, it was found that the MICP curve patterns of RT1, RT2, and RT3 displayed in **Figure 44** correspond to 89%, 78%, and 50 % of the cases in each group. Notably, for RT3, 50% of the cases exhibit curves, as displayed in **Figure 44** (at high total porosity), while the remaining samples show a pattern similar to RT2 samples. These results underscore the significance of accounting for total porosity and pore throat size distribution in rock quality assessments.

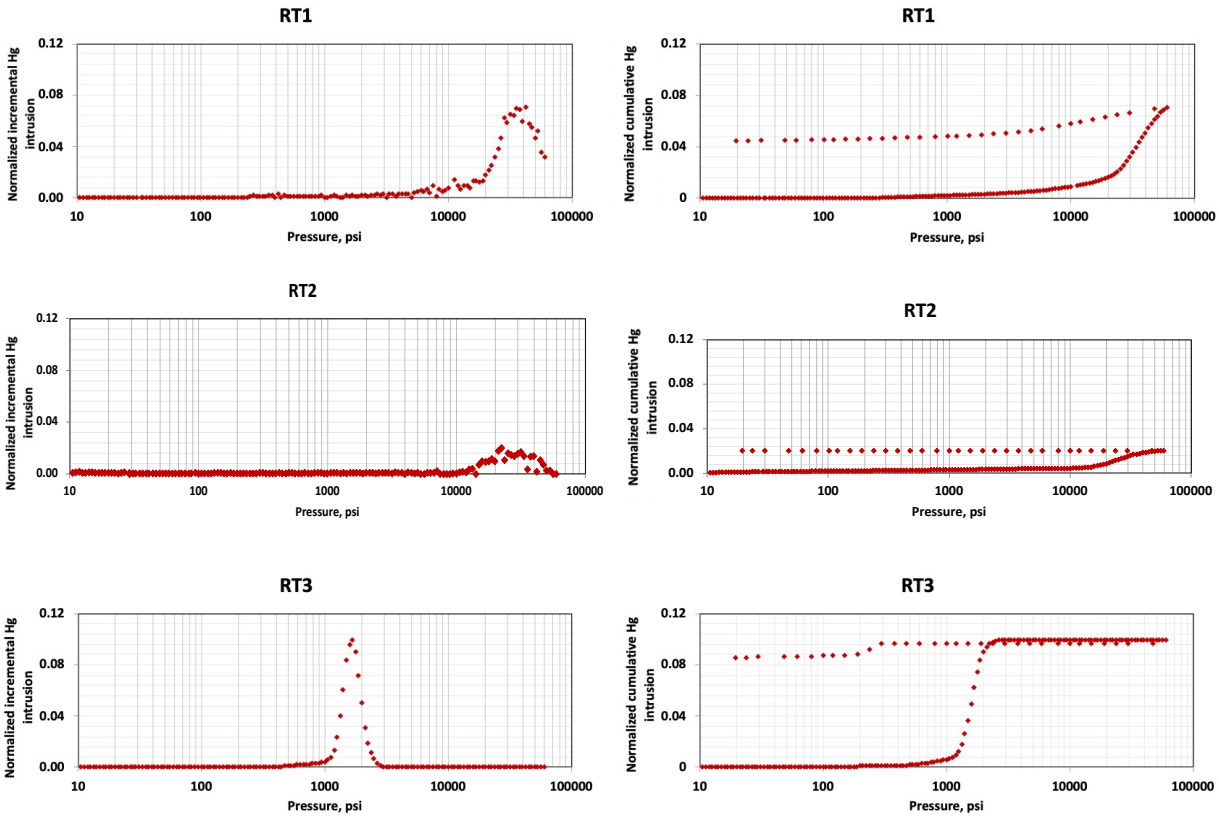


**Figure 44: Incremental and cumulative Hg intrusion curves for samples identify as RT1, RT2, and RT3.**

## 4.8. Extending Core-based Results to Well-log Data

The core material is expensive; hence not all the wells in a field have core material for laboratory petrophysical characterization. Rock typing can be performed using wireline measurements, such as triple combo; however, this identification needs to be verified using core material measurements to enhance the accuracy of the rock typing prediction models.

Gamma-ray, density, photoelectric, neutron porosity, and resistivity logs are available for most of the wells in the Uinta Basin. A sonic log was also available for this study. All six logs

were included to upscale the data. The wireline gamma ray log, and a synthetic gamma ray log created from XRF data were used for depth shifting.

The well log-based petrophysical properties, RT1 and RT3, exhibit similar values of PE, GR, and NPHI. This aligns with the core-based results where RT1 and RT2 show similar values of total porosity and TOC. RT2 presents the lowest gamma ray values in agreement with the lowest clay content and the smallest TOC measured in the lab; PE is high, which aligns with the high calcite percentage (PE=5.08 b/e). RT1 and RT2 exhibit PE values in the clay-and-dolomite-rich rocks range and the highest gamma-ray values associated with the high TOC (**Figure 45**).

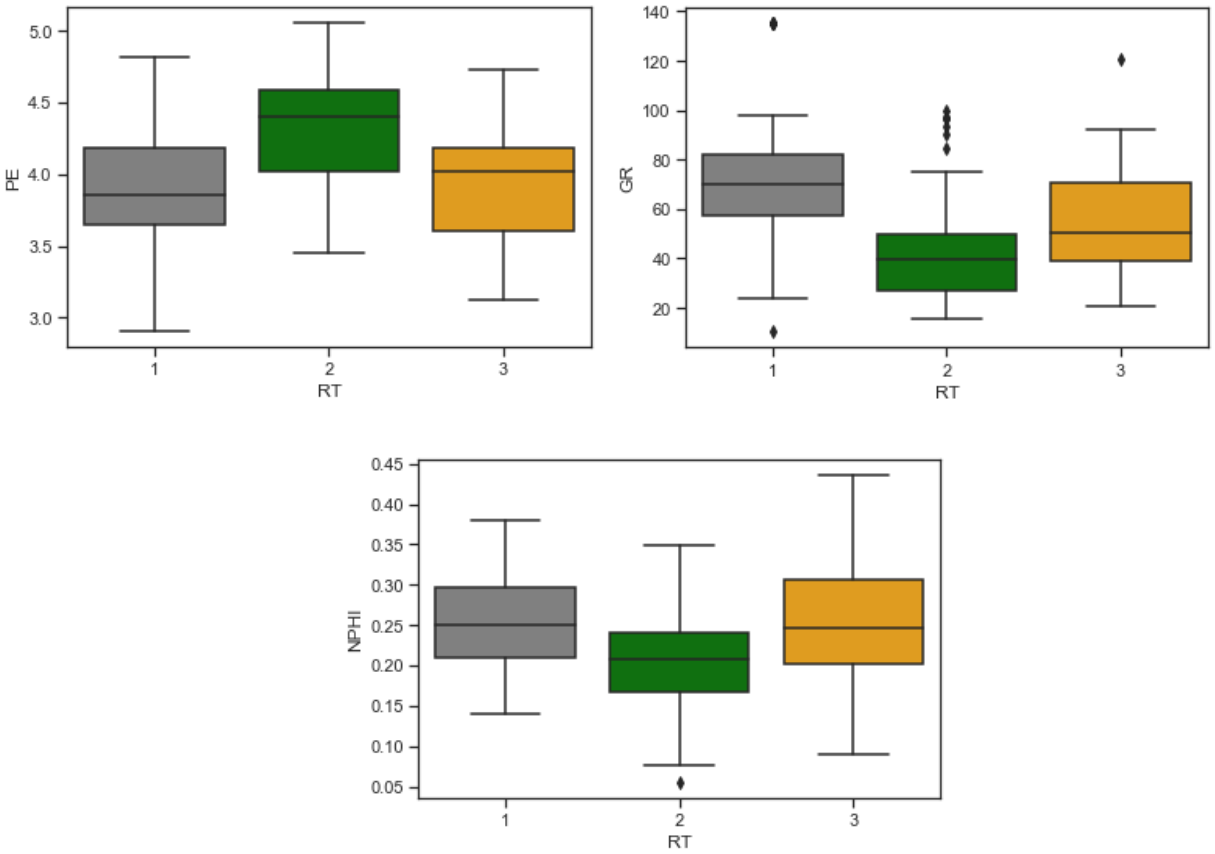


**Figure 45: Petrophysical parameters from the well logs.**

The upscaling performance consisted of extracting the log data, which matched the existing core data in depth. RT1 and RT3 with high total porosity and high TOC are clustered into one

group (RT1) since, from the log well data, both rock types have similar average gamma ray and PE values, as shown in the red circles in **Figure 46**.

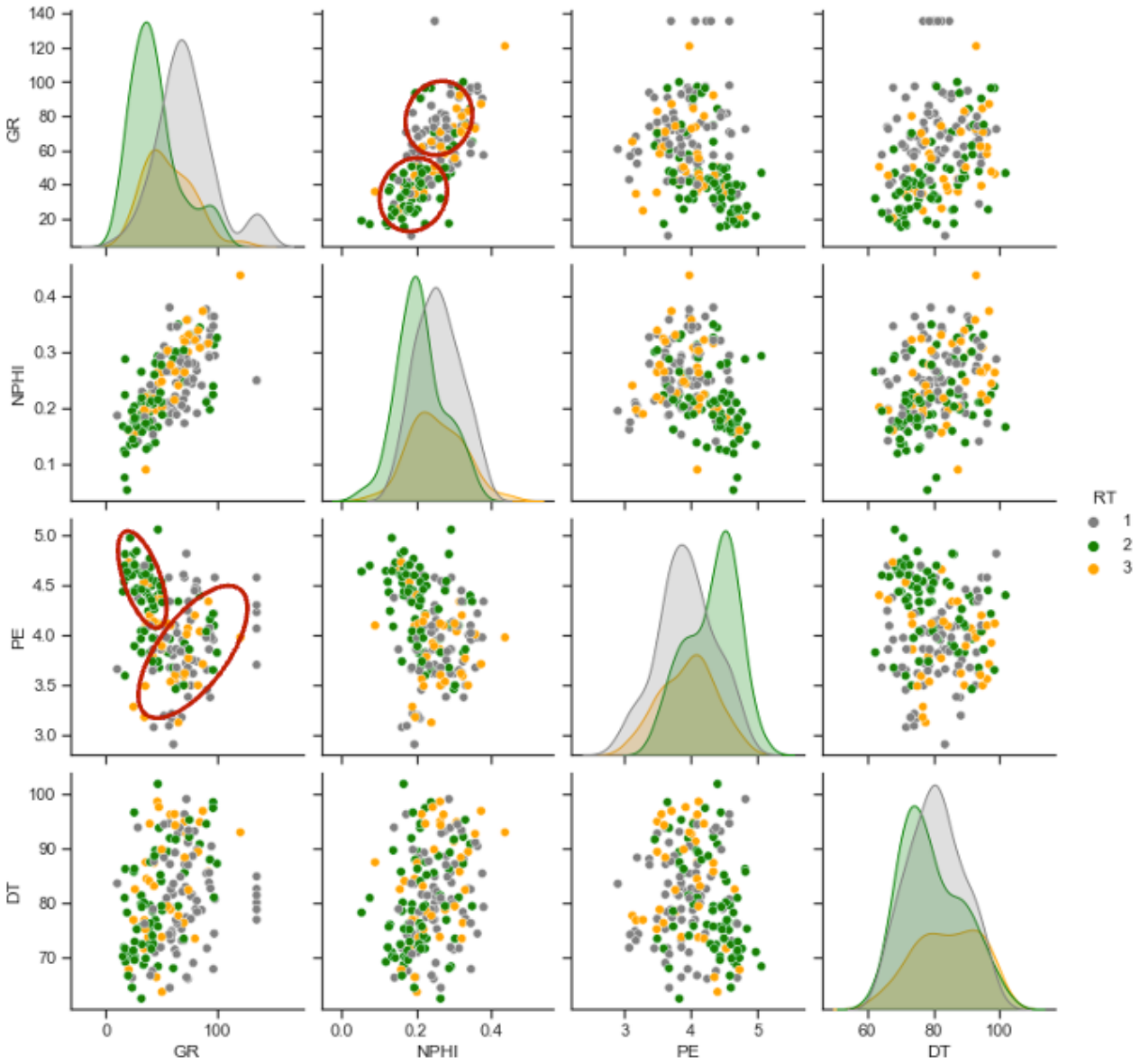


**Figure 46: Scatterplot of the well log data. It shows RT1, RT2, and RT3 logs . RT1 and RT3 have similar values for Gamma-ray, PE and NPHI in most cases. This aligns with core-based results, where RT1 and RT3 have similar values of total porosity and TOC.**

The k-means clustering technique generates the log-based rock types that train the supervised classification models: support vector machine (SVM), decision tree (DT), and random

forest (RF)). The classifier divided the data into train and test datasets. A small portion of the dataset made the predictions to avoid overfeeding the model. Finally, based on the rock types of forecasts by the model and their resemblance to core-based results, they were classified from more to less accurate, having RF and SVM exhibiting the best outcomes at an accuracy of 79% (**Figures 47 & 48**), while for DT it was 74% (**Figure 49**).

| | precision | recall | f1-score | support |
|---|---|---|---|---|
| RT 1 | 0.79 | 0.86 | 0.83 | 22 |
| RT 2 | 0.79 | 0.69 | 0.73 | 16 |
| accuracy | | | 0.79 | 38 |
| macro avg | 0.79 | 0.78 | 0.78 | 38 |
| weighted avg | 0.79 | 0.79 | 0.79 | 38 |

**Figure 47: Random Forest confusion matrix results. It shows an accuracy of 79 % in predicting rock types.**

| | precision | recall | f1-score | support |
|---|---|---|---|---|
| RT 1 | 0.85 | 0.77 | 0.81 | 22 |
| RT 2 | 0.72 | 0.81 | 0.76 | 16 |
| accuracy | | | 0.79 | 38 |
| macro avg | 0.79 | 0.79 | 0.79 | 38 |
| weighted avg | 0.80 | 0.79 | 0.79 | 38 |

**Figure 48: Support Vector Machine confusion matrix results. It shows an accuracy of 79 % in predicting rock types.**

| | precision | recall | f1-score | support |
|---|---|---|---|---|
| RT 1 | 0.75 | 0.82 | 0.78 | 22 |
| RT 2 | 0.71 | 0.62 | 0.67 | 16 |
| accuracy | | | 0.74 | 38 |
| macro avg | 0.73 | 0.72 | 0.72 | 38 |
| weighted avg | 0.73 | 0.74 | 0.73 | 38 |

**Figure 49: Decision tree confusion matrix results. It shows an accuracy of 79 % in predicting rock types.**

There is a fair agreement in rock type identification between using core-derived and log-derived models. The well log data is trained and calibrated using the core-based petrophysical properties. Random Forest or SVM can be implemented to predict the rock types using wireline data in other well in the area. In this case, SVM is implemented.

## 4.9. Linking Rock Types to Production

In this analysis for the Uinta basin, RT1 has the best indicators. It shows the highest porosity and the high source rock potential. The production of five wells around the cored well in this analysis was normalized by zone thickness to assess the impact of the rock types on their productivity. Following the work done by Gupta et al. (2017), the term rock type ratio was established (**Equation 4**).

$$RT_{ratio} = \frac{RT_{i\,(thickness)}}{\sum_{i}^{n} RT_{i\,(thickness)}} \qquad (4)$$

The normalized production corresponds to the cumulative barrel of oil equivalent (BOE) normalized by the perforated lengths. A good correlation between the RT1 ratio and normalized production is noticed (**Figure 50**). It implies that RT1 positively impacts production in the area.

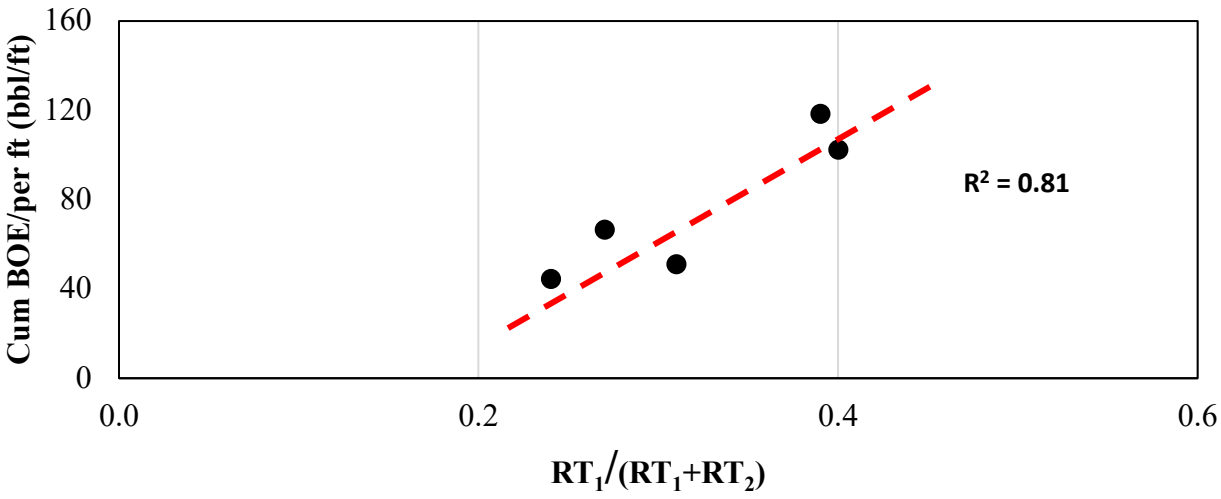


**Figure 50: Normalized production correlated to the RT1 ratio. A positive correlation exists between the RT1 ratio and the normalized cumulative BOE for the wells.**

# Chapter 5: Microstructure impact on Rock Properties in the Uinta Basin

The Scanning Electron Microscope (SEM) is a powerful laboratory instrument used to analyze the microstructure of rocks and identify features that control the system at the nanoscale (Chalmers et al., 2009; Loucks et al., 2009; Curtis et al., 2010; Schieber et al., 2010; Sondergeld et al., 2010). Researchers have proposed classifying pore structures based on SEM images in previous SEM studies. Schieber et al. (2010) proposed three categories for pore structure classification: phyllosilicate framework (PF), carbonate dissolution (CD), and organic matter (OM). PF-pores are commonly found in mudstone facies and are associated with shallow conditions, often containing artifacts such as sand and fossils. CD-pores are widely associated with carbonates and have highly irregular pore shapes. OM-pores are linked to the kerogen type and tend to have elliptical, circular, or irregular shapes. Curtis et al. (2011) found three classes of porosity in the Barnett, Woodford, and Horn River shales, cracklike, phyllosilicate, and organophyllic. The cracklike pores are associated with the cracks that flow through the formation. Phyllosilicate-pores constitute the inorganic matrix. Organophyllic-pores are small and large rounded and can be seen in the kerogen; the organophyllic porosity can positively impact the permeability of the shale formations (Wang and Reed, 2009; Curtis et al., 2012).

The complex microstructure and the different pore-type configurations within the samples directly affect the petrophysical properties of the Uinta basin. Previous studies revealed the high heterogeneity among the formation facies. Deposition and early compaction processes impacted the porosity and pore body structure, resulting in variable mixtures of mineral groups and high variation in pore throat size distribution. Higher dolomite content tends to result in better sorting, higher total porosity, and larger pore throats, while higher calcite content tends to decrease total

porosity values and reduce pore throat sizes. Clay-rich samples tend to have high total porosity, small pore throat size, and well-sorted pore systems.

The microstructural analysis of the core samples from the Uinta basin was carried out using SEM. A total of 26 samples were selected based on their macro-petrophysical properties, such as mineral composition and total porosity. Priority was given to samples with high dolomite content and high total porosity values. To prepare the samples for imaging, rock pieces were mechanically polished to create a flat surface. The samples were then polished with sandpaper up to 1500 grit in deionized water.

Further ion milling was carried out to ensure a planar surface and reduce the roughness of the samples. Backscattered electrons were used for atomic number contrast in all imaging to improve the visualization of the minerals in the samples. Energy Dispersive Spectroscopy (EDS) was used to determine the spatial mineralogy of the samples.

The results of the SEM analysis show a high degree of variability both between and within samples. **Figure 51** depicts six samples that showcase the wide range of microstructural diversity found among the depths at the same magnification. Scale bars are included in the bottom right corner of all SEM images for size comparison. Sample 522 illustrates the high heterogeneity in some samples, where larger quartz and Na-feldspar grains contain small dolomite grains. The space between the largest grains is mainly filled with clays (illite) and a few smaller grains. Most of the sample porosity is predominantly in these clay and smaller grain-filled regions. Conversely, sample 615 demonstrates a microstructure dominated by smaller dolomite grains, resulting in a highly porous (14%) dolomite matrix with heterogeneous porosity distribution.

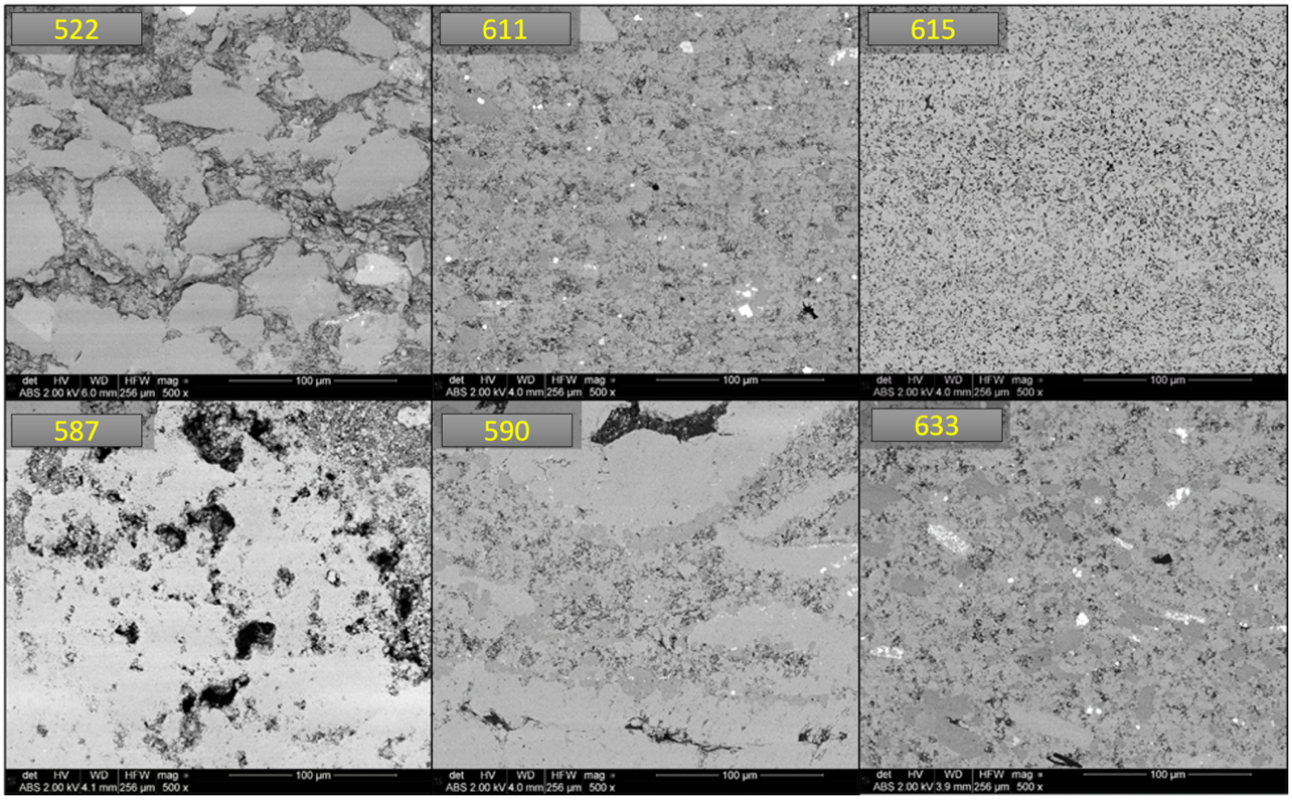


**Figure 51: SEM images at the same magnification of samples from the Uinta Basin, Utah (Courtesy Dr. Mark Curtis).**

This is further confirmed by micro–X-ray Computed Tomography (µ-XCT) images, which uses X-ray scanning to recreate a 3D model. Images of sample 615 revealed the presence of pores as large as hundreds of microns. It also shows the heterogeneity within the sample, indicating the presence of calcite veins and quartz minerals in the dolomite matrix (**Figure 52**).

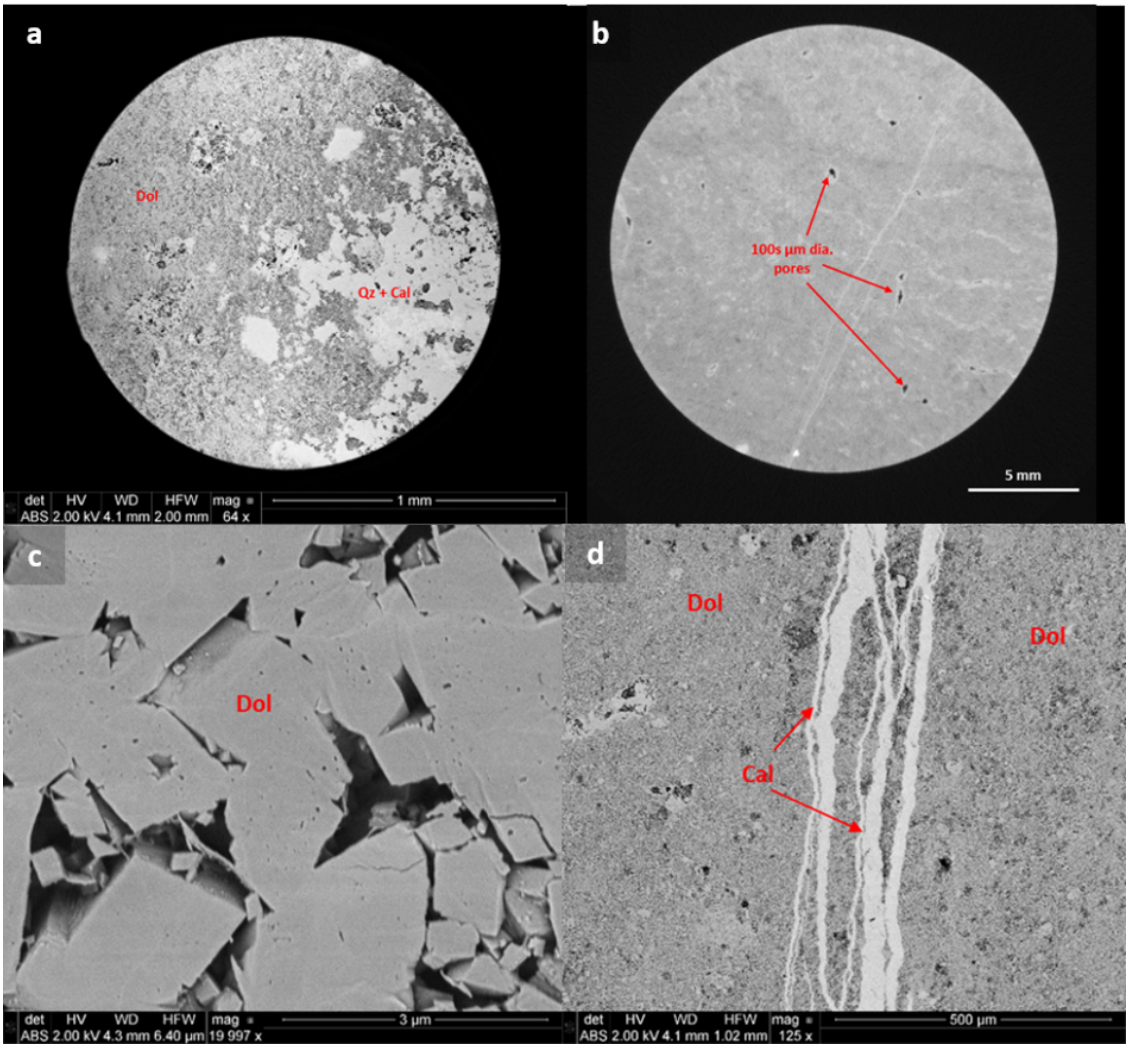


**Figure 52: SEM images from the Uinta basin. This is a high-dolomite content sample. a) Low magnification SEM image of microstructural heterogeneity within the 615-sample. Pores on the order of 10s of microns in diameter can be seen. b) µ-XCT image of the sample showing large pores on the order of 100s of microns in diameter. c) High magnification SEM image of smaller (<3 µm) diameter pores in the dolomite matrix of the sample. d) Calcite veins running through the dolomite matrix of the sample (Courtesy Dr. Mark Curtis).**

High-resolution imaging analysis showed that in specific samples with high TOC (>5%) and uniform distribution of organic material, nanopores within the organic material contribute to the porosity values (**Figure 53**). The organic porosity may be responsible for the clay-rich and

high TOC samples having higher total porosity. Conversely, this effect was not observed when organic material, possibly a solidified bitumen, flowed into the rock (**Figure 54**).

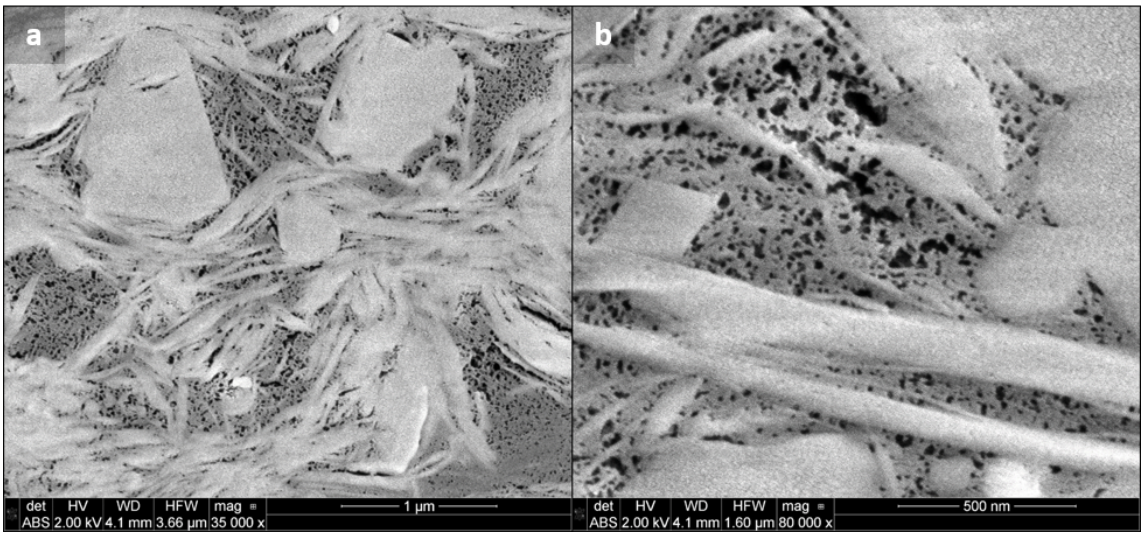


**Figure 53: a) SEM image of nanopores in organic matter of the 500-sample, b) high-resolution SEM image of the nanopores (Courtesy Dr. Mark Curtis).**

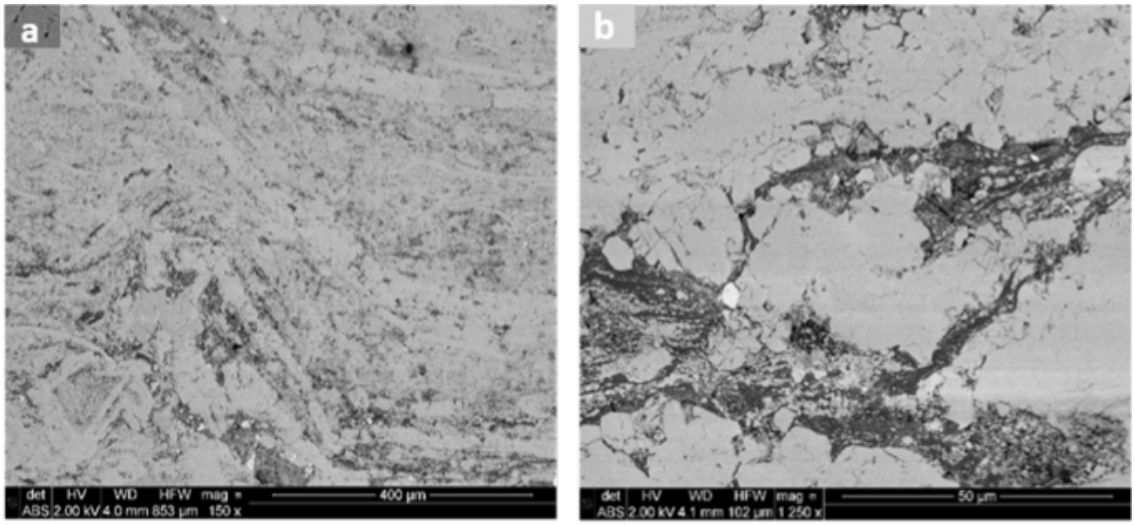


**Figure 544: a) Solidified bitumen that flowed into the 515-sample, and b) high-resolution SEM image of the nanopores (Courtesy Dr. Mark Curtis).**

**Figure 55** shows two samples, calcite-rich and dolomite-rich, with similar porosity, with grain radius from 1 to more than 5 µm in diameter for both groups. The dolomite-rich sample shows a bigger grain radius than the calcite-rich, which aligns with the previous analysis. **Figure**

**55a** shows the pore system in dolomite-rich samples, which have big pore throats and well-sorted systems, agreeing with the high total porosity and MCIP results. **Figure 52b** shows the clay minerals found in the pores of the calcite-rich samples.

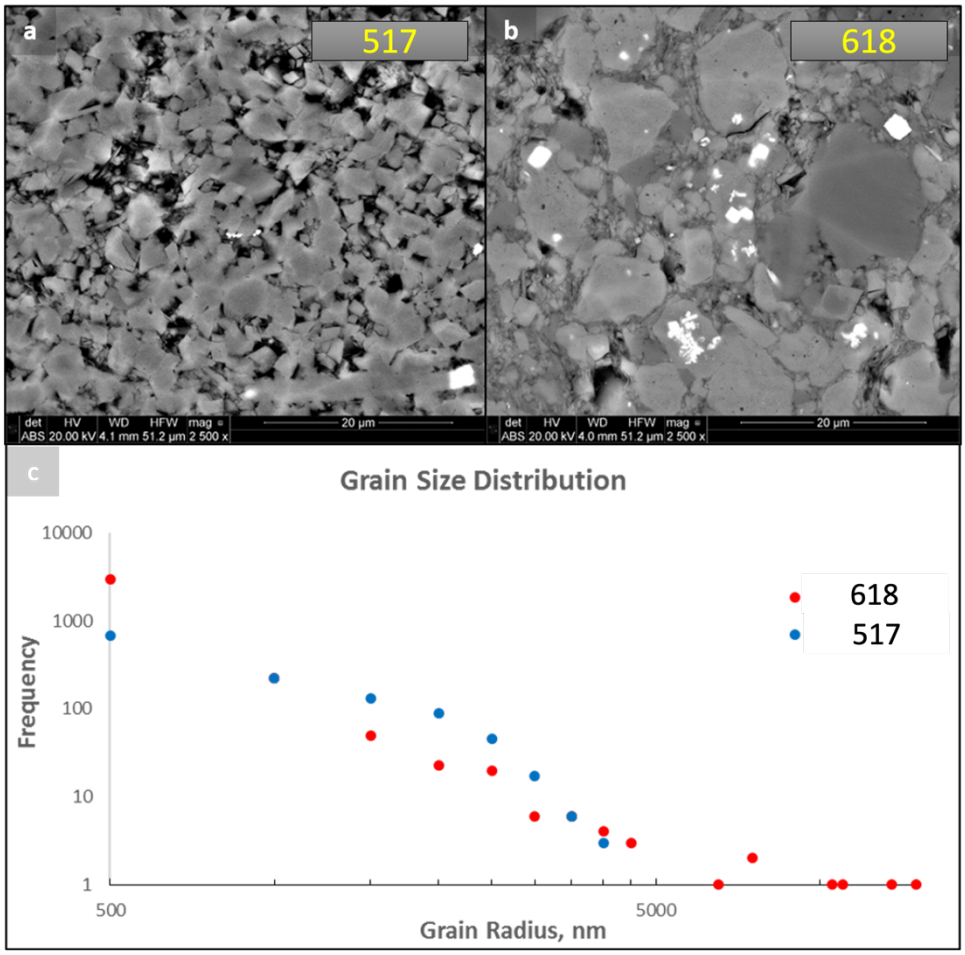


**Figure 55: SEM images and grain radius frequency for two samples in the formation. a) SEM image of the 517-sample, which is dolomite rich. b) SEM image of the 618-sample, which is calcite rich. Note the variation in grain size compared to the dolomite-rich sample. c) Grain size distribution derived from the SEM images (Courtesy Dr. Mark Curtis).**

Combining the Mercury Injection Capillary Pressure (MICP) technique with SEM imaging makes it possible to understand better the microstructure of the samples. **Figure 56** shows the incremental Hg intrusion curves and the SEM images from two dolomite-rich samples with high and low clay concentrations. The results indicated that the clay content highly reduces the pore

throat size in the rocks. The low clay content sample exhibits more well-sorted pore systems, and pores appear primarily open (**Figure 56a**)—Contrarily, higher the clay content in dolomite-rich samples, smaller the pore throats (**Figure 56c**).

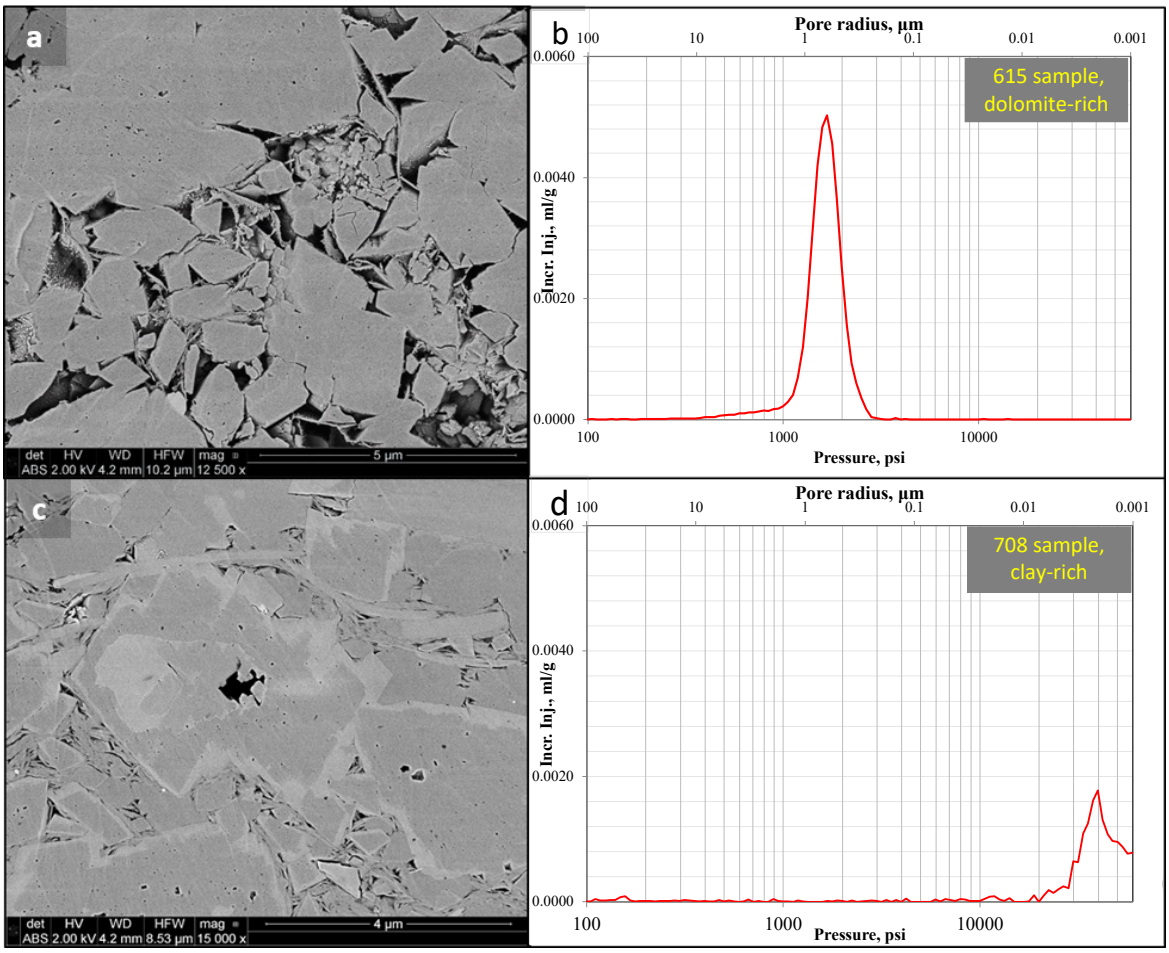


**Figure 56: Comparison of samples microstructure and MICP results. a) SEM image of the 615 sample, which has a clay content of 9%. b) Incremental MICP plot for the 708-sample showing a peak pore throat radius between 50-60 nm. c) SEM image of the sample with a clay content of 37%. d) Incremental MICP plot for the 708-sample showing a peak pore throat radius between 2-3 nm (Courtesy Dr. Mark Curtis).**

Broadly, samples with a relatively high clay content had smaller pore throats, whereas those with a higher dolomite content had larger pore throat radii. Zoned dolomite crystals and pyrite-replacement of fossils were identified as evidence of diagenesis, plus some sporadic evidence of dolomite dissolution was observed in a few samples. **Figure 57** shows an example.

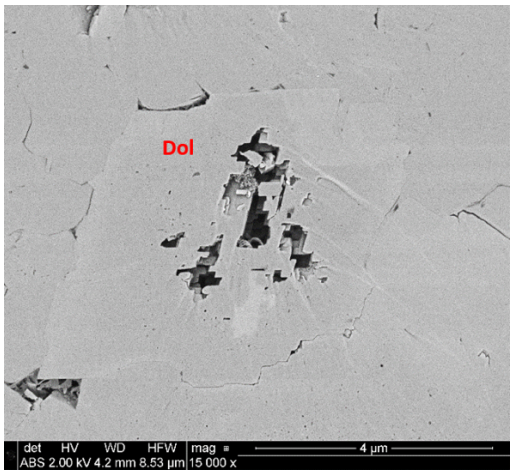


**Figure 57: Dissolution of the dolomite in the 554-sample (Courtesy Dr. Mark Curtis).**

## 5.1. Relating Rock Types to SEM Images

SEM imaging allows for identifying the specific microstructure that impacts the rock macro-properties, such as total porosity and TOC. The previous analysis established that RT1, RT2, and RT3 have different mineral compositions, total porosity, TOC, and pore throat size distribution. SEM imaging of the three rock types aligns with the lab results (**Figure 58**). The main minerals align with the results from SEM; RT1 is clay-rich with significant traces of quartz, has the highest total porosity, high TOC, and the highest fraction of movable hydrocarbons. RT1 SEM images show many fractures (**Figure 58a**) and more organic matter compared to RT2 and RT3. The organic matter hosted nanopores that may increase the total porosity (**Figure 58b**). In **Figure 58b,** pyrite grains are observed (in white) that match the high sulfurs and iron content associated with the RT1 intervals. RT2 is calcite-rich and shows the lowest total porosity and TOC. RT2 SEM images show the highest heterogeneity of the group (**Figure 58c**). RT3 samples (dolomite-rich), when exhibiting high total porosity, show smaller grains than RT1 and RT2, and the total porosity is mostly heterogeneously distributed throughout the entirety of the samples aligning with MICP pore throat size distribution results (**Figures 58e & 58f**). Thus, the different rock types obtained

from macroscopic petrophysical properties have completely different microstructures and are characteristically different.

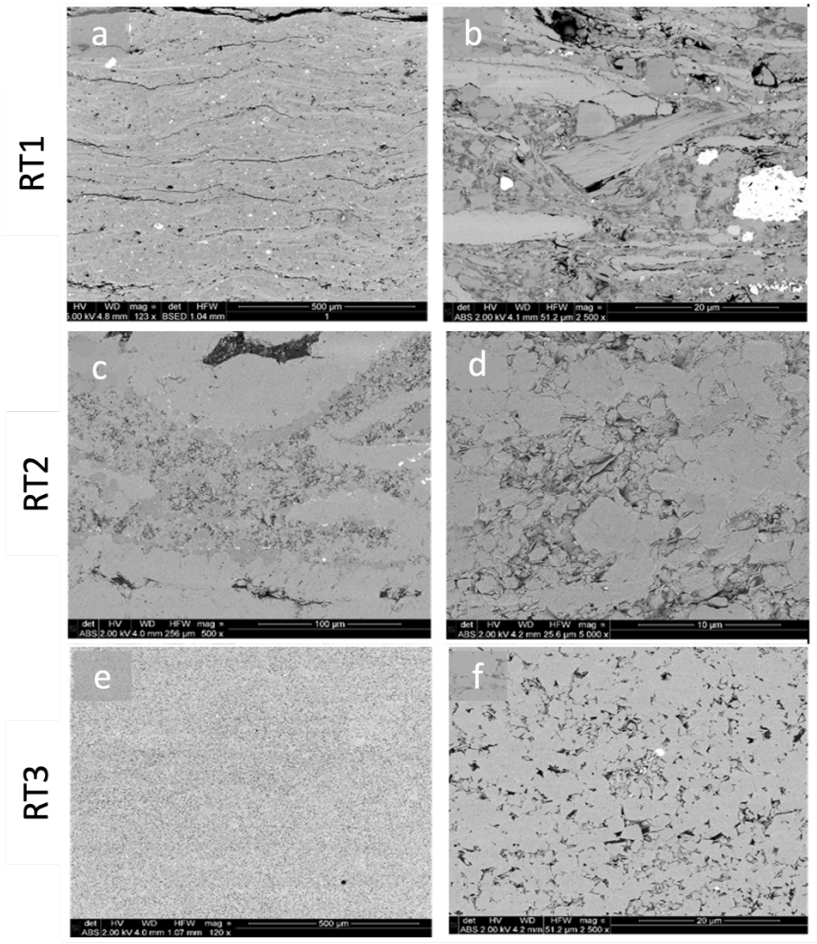


**Figure 58: SEM images of the three rock types in the Uinta Basin. RT3 is the best, having better-sorted grains, higher porosity, and high TOC. Calcite-rich RT2 is the worst, with the lowest storage capacity. (Courtesy Dr. Mark Curtis).**

Cross-plots of porosity vs. TOC and clay content were examined to determine which pore type dominates the porous structure. **Figures 59** and **60** show the total porosity cross-plots with TOC and clay concentration for the Uinta Basin samples. Clay content positively impacts the total porosity, with can be related to organic porosity. There is no correlation between TOC and total

porosity; this is likely because in the Uinta Basin, both organic and inorganic porosity are abundant, and neither dominates. This is evident in the SEM images in **Figure 61**.

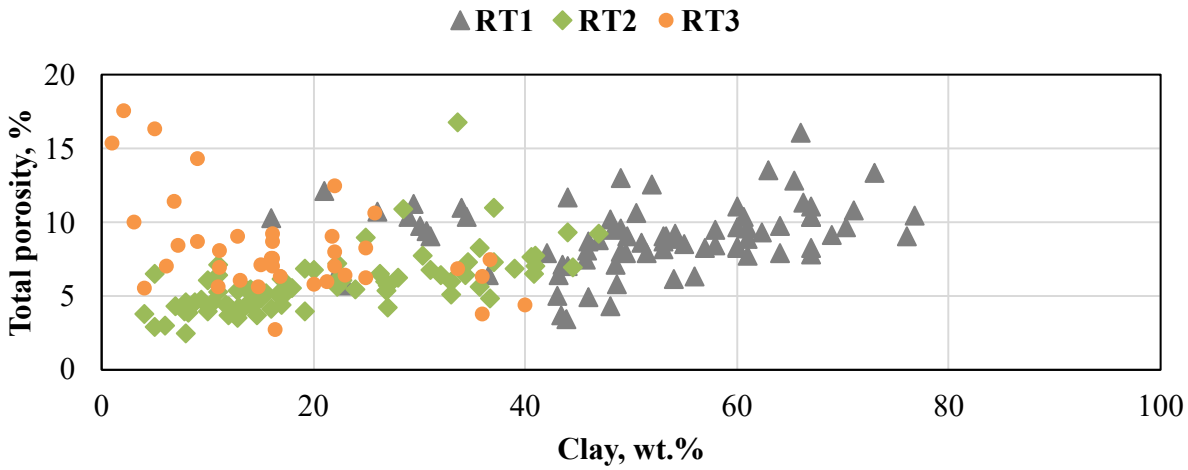


**Figure 59: Total porosity as a function of the clay concentration in the Uinta Basin. Positive correlation when clay wt.% is more than 20%.**

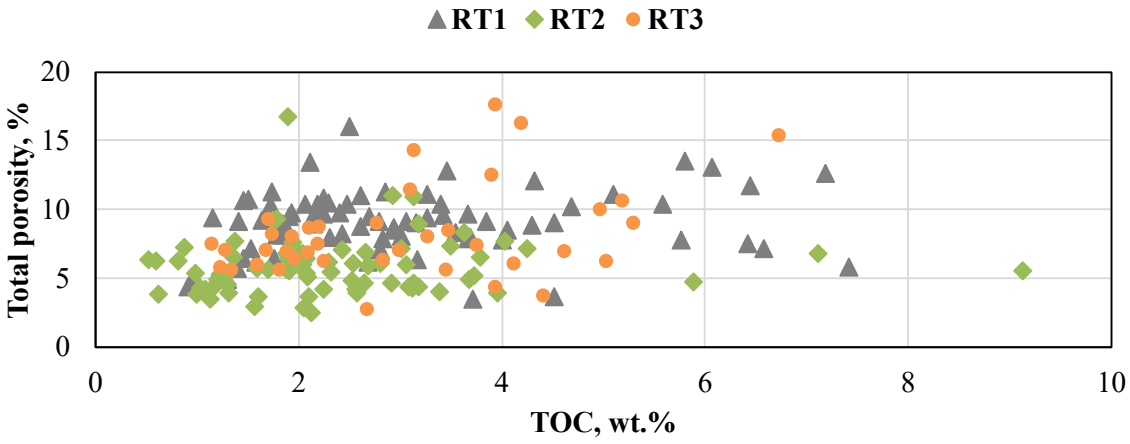


**Figure 60: Total porosity as a function of the TOC. No correlation is seen.**

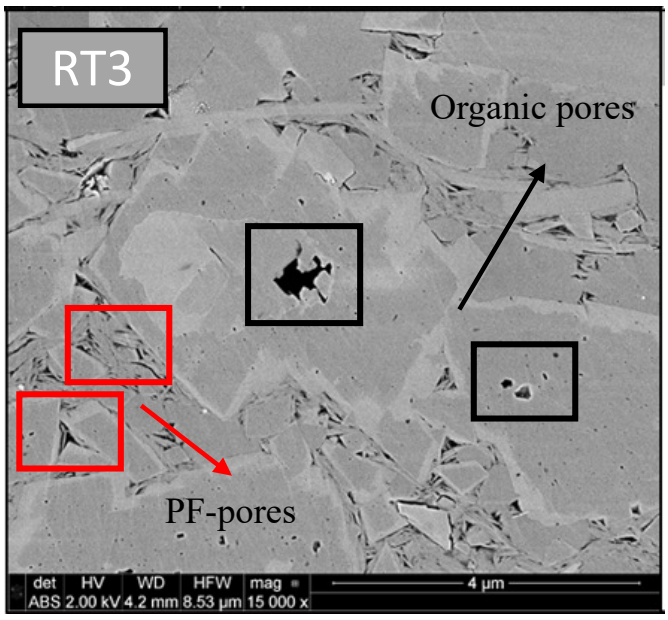


**Figure 61: SEM images from RT3 in the Uinta Basin. Images show abundant organic and inorganic pores.**

**Figure 62** shows the total porosity as a function of calcite content. There is an inverse correlation. It is especially evident when calcite content exceeds 40%, negatively impacting the total porosity. This can be related to clay minerals appearing to occlude the pore space among the calcite grains.

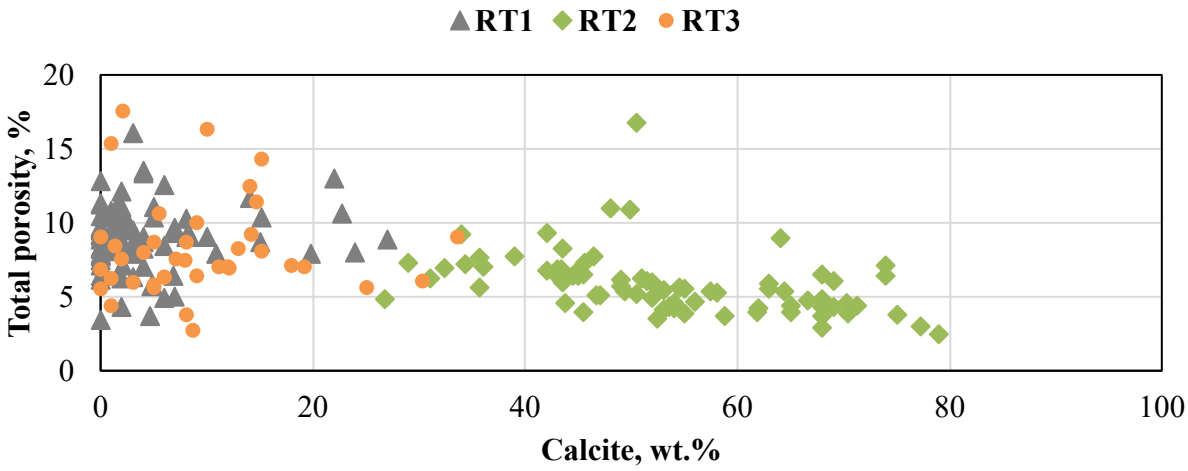


**Figure 62: Total porosity as a function of the calcite concentration.**

**Figure 63** shows the correlation between dolomite and total porosity. The high values in total porosity for dolomite are associated with the well-sorted pore system. **Figure 64** exhibits the SEM images of two dolomite-rich samples with high total porosity that confirm this statement.

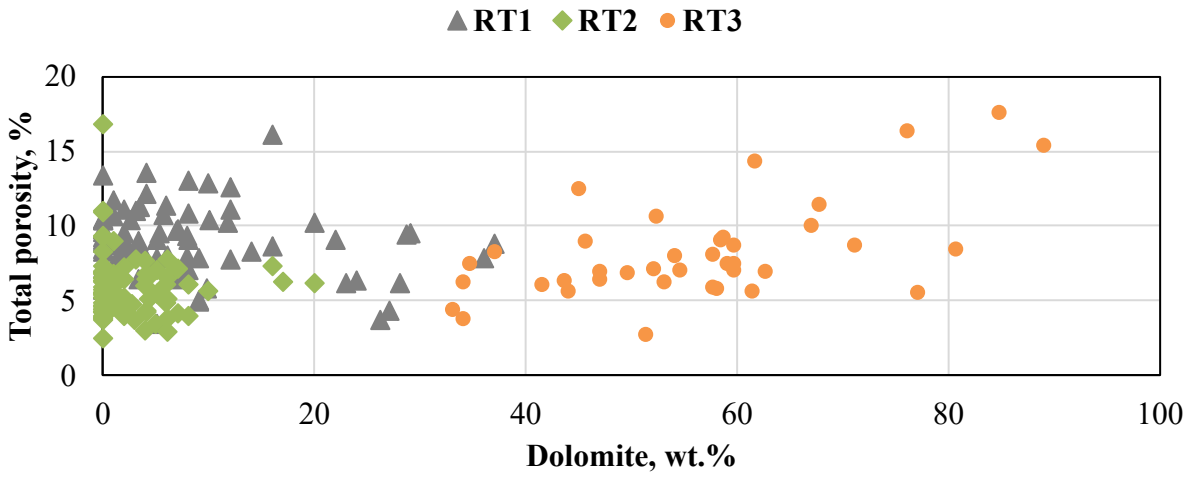


**Figure 63: Total porosity as a function of the dolomite concentration. It shows a weak correlation, significantly above 60 % in dolomite.**

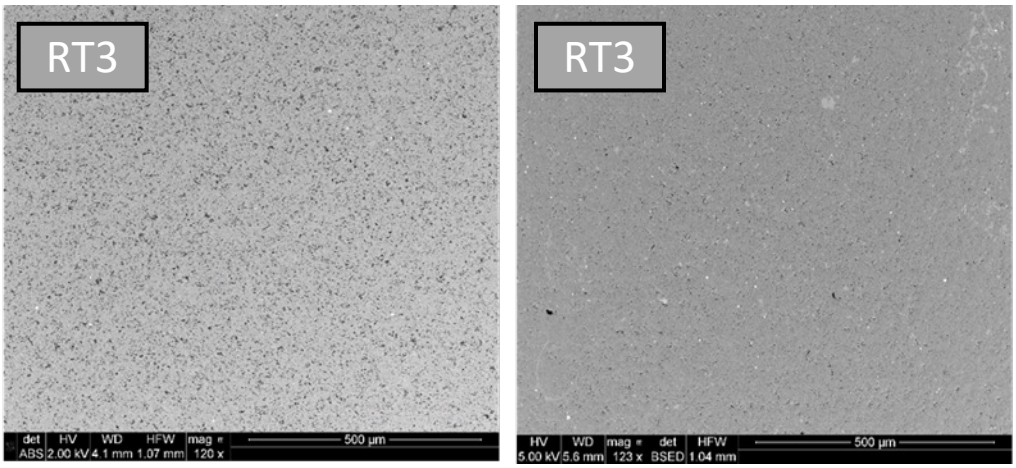


**Figure 64: SEM images for two different RT3 samples. Both show a well-sorted pore system that positively impacts the total porosity values.**

In conclusion, microstructural analysis of rock samples plays a crucial role in characterizing petrophysical properties, such as mineral composition, porosity, and pore throat size distribution, which are important for identifying and quantifying critical parameters in oil and gas formations. Local circumstances, such as kerogen type and centralized compaction, influence petrophysical properties. SEM allows the identification of features that control the rock system at the nanoscale. The SEM images of samples from the Uinta Basin show a high degree of variability both between and within samples. The complex microstructure and different pore-type configurations within the samples directly affect the macro-petrophysical properties of the Uinta basin. Deposition and early compaction processes impacted porosity and pore body structure, resulting in variable mixtures of mineral groups and high variation in pore throat size distribution. Higher dolomite content tends to result in better sorting and higher total porosity, while higher calcite content tends to decrease total porosity values and reduce pore throats. Clay-rich samples tend to have high total porosity, small pore throat size, and well-sorted pore systems.

# Chapter 6: Conclusions

The results from this study, which analyzed 208 samples from the Lake Fork Ranch in the Uinta Basin in Utah, align with the previous classification of the formation as highly complex and heterogeneous. The unique microstructure, high anisotropy, variation in organic material source quality and quantity, and irregular lithology resulted from the various geological processes the Uinta group underwent during its formation. Geologists in the area have identified three primary depositional environments and seven markers, all of them which distinctive macrostructural properties. These factors create challenges in developing and executing a proper exploitation plan for the fields in the region.

Reservoir engineers and petrophysicists collaborate to overcome these difficulties, performing machine learning algorithms on core-derived and well-log-derived data to classify the formation facies (reflecting pore structure and geometry, mineralogy profile, flow units, and source potential), estimate rock quality, and identify the ideal drilling and completion location.

Due to its relatively easy implementation but valuable contributions to field development, rock typing has gained popularity in the oil and gas industry. It is currently at a crucial stage in reservoir characterization by associating petrophysical properties to flow units knowns as rock types. Each rock type singularly possesses peculiar characteristics and impacts the whole reservoir system and, thus, the productivity of the well. Kale et al. (2010) demonstrated that rock types could be linked to lithofacies, and Gupta et al. (2017) also demonstrated that rock types could be associated with production and identify sweet spots.

The workflow followed in this study verified the correlation between core properties measured in the lab and the data from the wireline survey (triple combo) using data mining tools available such as K-mean, SVM, and PCA. It allows for handling bulky amounts of data and

turning it into purposeful insights automatically and effectively, meaning that this work can be applied to any other formation quickly and easily with minor changes.

This study used machine learning techniques to define three main rock types (RT1, RT2, and RT3) in the formation, each with a specific mineral composition, source potential, and storage capacity. RT1 was identified as clay-rich, RT2 calcite-rich, and RT3 as dolomite-rich. The relative contribution of types 1, 2, and 3 is 37, 42, and 21 %, respectively, to the total studied material. The top section of the analyzed core is dominantly occupied by RT1, which generally has good porosity and relatively higher TOC. Most of the bottom section is carbonate-rich rock types, in which calcite-rich and dolomite-rich layers are interbedded.

RT3 has total porosity and TOC values similar to RT1, displaying high total porosity and the highest source rock potential, but it is less common. RT2 is the less favorable, having low porosity and low TOC values. In RT3, an anomaly caused by the dolomite content was particularly important in this study since it seems to have samples with high dolomite content showing low and high total porosity. The main reason is the dolomite dissolution and the distinct depositional environments (open lacustric and marginal lacustric) in which the formation was formed. SEM analyses suggested that a fraction of porosity is associated with organic matter; however, most of the porosity was found in the inorganic mineral matrix. SEM imaging observed large variations in the microstructure. Some samples showed significant heterogeneity in the microstructure at a given depth. SEM-based porosity estimates support the high values observed in RT3 samples from total porosity measurements. RT3 samples had more well-sorted grains than RT2 samples. MICP data align with SEM images; RT1 samples have small pore throats and narrow distribution. RT2 samples exhibit narrow and broad pore size distribution curves that tend to small pore throats. In the case of RT3, at high total porosity values, the dolomite-rich samples show large pore throats.

The workflow implemented in this study allows petrophysicists to identify and define patterns and correlations in the petrophysical data that lead to meaningful insights for reservoir development. For example, RT2 is probably not a good reservoir and may not be worth investing money and time in those intervals. Contrarily, RT1 and RT3 have good for storage and have higher organic material. RT1 samples show high TOC, high total porosity, and small pore throats, suggesting that RT1 could be associated with the source rock in the Uinta Basin. RT3 at high total porosity values can be related to high conductivity zones.

Since core-derived studies are time-consuming and expensive, log-derived rock typing can help reservoir or production engineers optimize perforation intervals and fracture stage count. This study proved a fair agreement in rock type identification between core-derived and log-derived models, which suggests that logs can be used to derive rock types. After linking the rock types to the production, RT1 shows a positive correlation with the well productivity, meaning that rock typing workflow can be applied to different well in the Uinta Basin to identify RT1.

The Uinta basin leads the hydrocarbon production in Utah. The study provides a comprehensive core analysis dataset, highlighting the vertical complexity of the Uinta group. It also validated the agreement between the core and log data, making it possible to quickly interpret the wireline data at the site.

# References


Amaefule, J. O., Altunbay, M., Tiab, D., Kersey, D. G., & Keelan, D. K. 1993. Enhanced Reservoir Description: Using Core and Log Data to Identify Hydraulic (Flow) Units and Predict Permeability in Uncored Intervals/Wells. Presented at Annual Technical Conference and Exhibition, Houston, Texas, 3-6 Oct. SPE 26436. http://dx. doi:10.2118/26436-MS.

Amin, S., Wehner, M., & Heidari, Z. 2016. Rock Classification in the Eagle Ford Shale through Integration of Petrophysical, Geological, and Geochemical Characterization. Presented at the 57th Annual Logging Symposium, 25-29 Jun, Reykjavik, Iceland.

Aminzadeh, F., Tafti, T. A., & Maity, D. 2013. An integrated methodology for sub-surface fracture characterization using microseismic data: A case study at the NWW Geysers. Computers & Geosciences, 54, 39-49. https://doi.org/10.1016/j.cageo.2012.10.013.

Aranibar, A., Saneifar, M., & Heidari, Z. 2013. Petrophysical Rock Typing in Organic-Rich Source Rocks Using Well Logs. Presented at the SPE Unconventional Resources Technology Conference, Denver, CO, 12–14 August. SPE-168913-MS. http://dx.doi.org/10.2118/168913-MS.

Bailey, S. 2009. Closure and Compressibility Corrections to Capillary Pressure Data in Shales. Oral presentation given at the DWLS 2009 Workshop, Beyond the Basics of Capillary Pressure: Advanced Topics.

Ballard, B. D. 2007. Quantitative Mineralogy of Reservoir Rocks Using Fourier Transform Infrared Spectroscopy. Paper presented at the SPE Annual Technical Conference and Exhibition, Anaheim, California, USA. doi: https://doi.org/10.2118/113023-STU.

Banner, J. L. 1995. Application of the Trace Element and Isotope Geochemistry of Strontium to Studies of Carbonate Diagenesis. Sedimentology, 42, 805-824.

Barach, B., Jaafar, M., Gaafar, G., Agi, A., Junin, R., Sidek, A., Gbadamosi, A., Yakasai, F., Oseh, J., & Gbonhibor, J. 2022. Development and Identification of Petrophysical Rock Typing for Effective Reservoir Characterization. Paper presented at the SPE Nigeria Annual International Conference and Exhibition, Lagos, Nigeria, August 2022. doi: https://doi.org/10.2118/211918-MS

Bouch, J. E., Milodowski, A. E., & Ambrose, K. 2004. Contrasting patterns of pore-system modification due to dolomitization and fracturing in Dinantian basin-margin carbonates from the UK, vol. 235. Geological Society Special Publication, pp. 325–348.

Breiman, L. (1984). Classification and Regression Trees (1st ed.). Routledge. https://doi.org/10.1201/9781315139470

Chalmers, G., Bustin, R. M., & Powers, I. (2009). A pore by any other name would be as small: The importance of meso- and microporosity in shale gas capacity (abs.). AAPG Search and Discovery article 90090. Retrieved from http://www.searchanddiscovery.com/abstracts/html/2009/annual/abstracts/chalmers.htm (accessed November 11, 2009).

Chon, T.S., & Park, Y.S. 2008. Self-Organizing Map, In Encyclopedia of Ecology, edited by Sven Erik Jorgensen and Brian D. Fath, *Academic Press, Oxford*, Pages 3203-3210, ISBN 9780080454054, http://dx.doi.org/10.1016/B978-008045405-4.00907-1.

Cortes, C. & Vapnik, V. 1995. Support-vector networks. *Machine Learning*. 20 (3): Book Pg. 273–297. doi: 10.1007/BF00994018.

Cortez, M. 2012. Chemostratigraphy, Paleoceanography, and Sequence Stratigraphy of the Pennsylvanian – Permian section in the Midland basin of the West Texas, with focus on the Wolfcamp formation. MSS Geology Thesis, The University of Texas at Arlington, Arlington, Texas.

Craig, D., Chidsey, T., McClure, K., Bereskin, R., & Deo, M. 2003. Reservoir Characterization of the Lower Green River Formation, Uinta Basin, Utah. Utah Geological Survey.

Coyle, S., & Kyle S. "Rock-Type Model Characterization of Composition and Fabric in the Haynesville Shale." Paper presented at the 2014 SEG Annual Meeting, Denver, Colorado, USA, October 2014.

Curtis, M., Cardott, B., Sondergeld, C. & Rai, C. 2012. Development of organic porosity in the Woodford Shale with increasing thermal maturity. *Int. J. Coal Geol.* 103, 26–31.

Curtis, M., Sondergeld, C., Ambrose, R. & Rai, C. 2012. Microstructural investigation of gas shales in two- and three-dimensions using nanometer-scale resolution imaging. *AAPG Bull.* 96, 665–677.

Dang, S., Gupta, I., Chakravarty, A., Bhoumick, P., Taneja, S., Sondergeld, C., & Rai, C. 2017. Recovering Elastic Properties From Rock Fragments. *Petrophysics* 58: 270–280.

Dang, S., Sondergeld, C., & Rai, C. 2019. Interpretation of Nuclear-Magnetic-Resonance Response to Hydrocarbons: Application to Miscible Enhanced-Oil-Recovery Experiments in Shales. SPE *Res Eval & Eng* 22: 302–309. doi: https://doi.org/10.2118/191144-PA.

Davies, D. K., Williams, B. P. J., & Vessell, R. K. 1993. Reservoir Geometry and Internal Permeability Distribution in Fluvial, Tight, Gas Sandstones, Travis Peak Formation, Texas. *SPE Reservoir Engineering*. http://dx.doi:10.2118/21850-PA.

Earle, S. 2015. Chemical Sedimentary Rocks. In Physical Geology. Open Textbook Library. https://geo.libretexts.org/Bookshelves/Geology/Book%3A_Physical_Geology_(Earle)/06%3A_Sediments_and_Sedimentary_Rocks/6.02%3A_Chemical_Sedimentary_Rocks.

Effenberger, A. J. & Scott, J. R. 2010. Effect of Atmospheric Conditions on LIBS Spectra: Sensor 2010, 10, 4907-4925, https://www.ncbi.nlm.nih.gov/pmc/articles/PMC3292154.

Ehrenberg, S. N. 2004. Porosity and Permeability in Miocene Carbonate Platforms of the Marion Plateau, Offshore NE Australia: Relationships to Stratigraphy, Facies and Dolomitization, vol. 235. Geological Society Special Publication, pp. 233–253.

Ehrenberg, S. N., Eberli, G. P., Keramati, M., & Moallemi, S. A. 2006. Porosity-permeability relationships in interlayered limestone-dolostone reservoirs. AAPG (Am. Assoc. Pet. Geol.) Bull. 90(1), 91–114.

Elzarka, M. H., & Younes, M., A., A. 1987. Generation, migration, and accumulation of oil of El-Ayun Field, Gulf of Suez, Egypt. Geology Department, Faculty of Science, Alexandria University, Alexandria, Egypt. Marine and Petroleum Geology, 1987, Vol 4.

Espitalie, J., Madec, M., Tissot, B., & Leplat, P. 1977. Source Rock Characterization Method for Petroleum Exploration. Paper number OTC 2935 presented at the Offshore Technology Conference, Houston, Texas.

Espitalie, J. 1982. Syntheses Geologiques et Geochimie 7020 dated April 28, 1982. Institut Francais du Petrole.

Espitalie, J., Marquis, F., & Barsony, I. 1984. Geochemical Logging. In K. J. Voorhees (Ed.), Analytical Pyrolysis Techniques and Applications (pp. 276-304). London: Butterworths.

Espitalie, J., Deroo, G., & Marquis, F. 1985. Rock-Eval Pyrolysis and its Applications. Institut Francais du Petrole, Geologie No. 27299, Project B41 79008.

Fouch, T., & Dean, W. 1982. Lacustrine and associated clastic depositional environments. In Sandstone Depositional Environments (P. A. Scholle and D. Spearing, eds.): Amer. Assoc. Petroleum Geologists Memoir 31, p. 87-114.

Fouch, T., Nuccio, V., Osmond, J., MacMillan, L., Cashion, W.B., & Wandrey, C. 1992. Oil and gas in uppermost Cretaceous and Tertiary rock, Uinta basin, Utah: in Fouch, T.D., Nuccio, V.F., and Chidsey, T.C., Jr.; Hydrocarbon and mineral resources of the Uinta basin, Utah and Colorado: Utah Geological Association, Guidebook 20, p.9-47.

Fred T. MacKenzie; Diagenesis of Shaly Rocks. *AAPG Bulletin* 1970; 54 (5): 858. doi: https://doi.org/10.1306/5D25CAF3-16C1-11D7-8645000102C1865D.

Guido, S. 2014. K-Means Clustering with Scikit-Learn. Presentation uploaded on Slideshare.net. Web Address: https://www.slideshare.net/SarahGuido/kmeans- clustering-with-scikitlearn (accessed Mar 2023).

Gunter, G. W., Finneran, J. M., Hartmann, D. J., & J. D. Miller. 1997. Early Determination of Reservoir Flow Units Using an Integrated Petrophysical Method. Paper presented at the SPE Annual Technical Conference and Exhibition, San Antonio, Texas. doi: https://doi.org/10.2118/38679-MS

Gupta, N. 2012. Multi-scale characterization of the Woodford shale in West-central Oklahoma from Scanning electron microscope to 3D seismic, PhD Dissertation, Oklahoma U., Norman, Oklahoma.

Gupta, I. 2017. Rock Typing in Organic Shales: Eagle Ford, Woodford, Barnett and Wolfcamp Formations, Master Thesis, Oklahoma U., Norman, Oklahoma.

Han, H., Dang, S., Acosta, J., Fu, J., Sondergeld, C., & Rai, C. 2019. X-Ray Fluorescence and Laser-Induced Breakdown Spectroscopy for Advanced Rock Elemental Analysis. Paper presented at the SPE/AAPG/SEG Unconventional Resources Technology Conference, Denver, Colorado. doi: https://doi.org/10.15530/urtec-2019-1072.

Hay, J. L., a& Pharr, G., M. 2000. Instrumented Indentation Testing. ASMM Handbook, 232-243.

Hardisty, L., Pranter, M., Devegowda, D., Marfurt, K., Sondergeld, C., Rai, C., Gupta, I., Han, H., Dang, S., McLain, C., & Larese, R. 2021. Stratigraphic variability of Mississippian Meramec chemofacies and petrophysical properties using machine learning and geostatistical modeling, STACK trend, Anadarko Basin, Oklahoma, *Interpretation* 9: T987-T1007.

Hegde, C., Gray, K.E., 2017. Use of machine learning and data analytics to increase drilling efficiency for nearby wells. J Nat Gas Sci Eng 40, 327–335. https://doi.org/10.1016/j.jngse.2017.02.019

Douglass, E. 1914. Geology of the Uinta Formation. Geological Society of America Bulletin, 25(1), 417-425. https://pubs.geoscienceworld.org/gsa/gsabulletin/article/25/1/417/2762/geology-of-the-uinta-formation

Hintze, L. F., & Kowallis, B. J. 2009. Geologic history of Utah; a field guide to Utah's rocks. Brigham Young University Department of Geology.

Holmes, M., & Dolan, M. 2014. A comprehensive Geochemical and Petrophysical Integration Study for the Permian Basin. Oral presentation at the Geoscience Technology Workshop, AAPG, Houston, Texas, 4-5 September.

Jacobi, D., Longo, J., & Rodriguez, J. 2022. The Significance of Accessory Minerals in Source Rocks: A Provenance Study of the Origin of Anatase and Pyrite and Their Relationship to the Chemistry of Organic Matter. Paper presented at the SPE/AAPG/SEG Unconventional Resources Technology Conference, Houston, Texas, USA. doi: https://doi.org/10.15530/urtec-2022-3721226.

Jarvie, D. M. 1991. Total Organic Carbon (TOC) Analysis. In: Merrill, R.K., Ed., Treatise of Petroleum Geology, Handbook of Petroleum Geology, Source and Migration Processes and Evaluation Techniques, AAPG Press, Tulsa, 113-118.

Johnson, K. R., Reynolds, M. L., Werth, K. W., & Thomasson, J. R. (2003). Overview of the Late Cretaceous, early Paleocene, and early Eocene megafloras of the Denver Basin, Colorado. Rocky Mountain Geology, 38(1), 101-120. https://doi.org/10.2113/gsrocky.38.1.101.

Junck R., & Benson D. 1973. A High-Resolution Pulse Transmission Technique for Determining Ultrasonic Velocities, *Review of Scientific Instruments*, Volume 44, pp.1044-1048.

Kale, S. 2009. Petrophysical Characterization of Barnett Shale Play, Master Thesis, Oklahoma U., Norman, Oklahoma.

Kale, S., Rai, C., & Sondergeld, C. 2010. Rock Typing in Gas Shales. Presented at SPE Annual Technical Conference, Florence, Italy, 19-22 September. SPE 134539. http://dx.doi:10.2118/134539-MS.

Karastathis A. 2007. Petrophysical Measurements on Tight Gas Shale. Master Thesis, University of Oklahoma, Norman, Oklahoma.

Kenyon, W. E., P. I. Day, C. Straley, and J. F. Willemsen. 1988. A three- part study of NMR longitudinal relaxation properties of water-saturated sandstones, SPE Form. Eval., 3(3), 622–636, doi:10.2118/15643-PA

Kietzke, K. K., & Wilde, D. 1993. Depositional facies and cyclic sequences in the Eocene Green River Formation, southwestern Wyoming. Sedimentary Geology, 85(1-4), 125-148.

Knackstedt, M. A., Latham, S.J ., Sheppard, A. P., Sok, R. M., & Kumar, M. 2010. Rock Typing Across Disciplines. Presented at SPWLA 51st Annual Logging Symposium, 19- 23 June, Perth, Australia.

Kodama, H., & Grim, R. E. 2022. Clay mineral. Encyclopedia Britannica. https://www.britannica.com/science/clay-mineral

Koeshidayatullah, A., Corlett, H., Stacey, J., Swart, P., Boyce, A., & Hollis, C. 2020. Origin and evolution of fault-controlled hydrothermal dolomitization fronts: A new insight. Earth and Planetary Science Letters. https://doi.org/10.1016/j.epsl.2020.116291.

Kopaska-Merkel, D. C., Mann, S. D., & Schmoker, J. W. 1994. Controls on reservoir development in a shelf carbonate: Upper Jurassic Smackover Formation of Alabama. AAPG (Am. Assoc. Pet. Geol.) Bull. 78(6), 938–959.

Kumar, V., Curtis, M., Gupta, N., Sondergeld, C., & Rai, C. 2012. Estimation of Elastic Properties of Organic Matter and Woodford Shale Through Nanoindentation Measurements. Paper

presented at the SPE Canadian Unconventional Resources Conference, Calgary, Alberta, Canada, October. doi: https://doi.org/10.2118/162778-MS.

Law, C. 1999. Evaluating Source Rocks, Chapter 6, AAPG special volumes, Petroleum Geology/Handbook of Petroleum Geology: Exploring for Oil and Gas Traps, Pages 6-1 - 6-41, Edited by Edward A. Beaumont and Norman H. Foster.

Lieber, R. & Dunn, J. 2013. A Proposed Petrophysical Rock Typing Workflow for an Unconventional Mudstone Reservoir – Example from the Niobrara of the DJ Basin. Presented at the SPWLA 54th Annual Logging Symposium, 22-26 June, New Orleans, Louisiana.

Lucia, J., Kerans, C., & Jennings, J. 2003. Carbonate Reservoir Characterization. *J Pet Technol* 55 (2003): 70–72. doi: https://doi.org/10.2118/82071-JPT.

Li, H., Hart, B., Dawson, M., & Radjef, E. 2015. Characterizing the Middle Bakken: Laboratory Measurement and Rock Typing of the Middle Bakken Formation. Presented at SPE Unconventional Resources Technology Conference, San Antonio, Texas, 20-22 July. http://dx.doi: 10.2118/178676-MS.

Liu, M., Lu, C., Tieu, K. A., Peng, C. T., & Kong, C. (2015). A combined experimental-numerical approach for determining mechanical properties of aluminum subjects to nanoindentation. Scientific reports, 5(1), 1-16.

Lloyd, S. P. 1957. Least square quantization in PCM. Bell Telephone Laboratories Paper. Published in journal much later: Lloyd., S. P. (1982). Least squares quantization in PCM. *IEEE Transactions on Information Theory*. 28 (2): 129–137. doi:10.1109/TIT.1982.1056489.

Lopez, L. A. 2016. Understanding Organic Matter Structural Changes with Increasing Thermal Maturity from Oil Shale Plays through SEM imaging. Presented at the Unconventional Resources Technology Conference, San Antonio, Texas, 1-3 Aug 2016.

Loucks, R. G., Reed, R. M., Ruppel, S. C., & Jarvie, D. M. 2009. Morphology, genesis, and distribution of nanometer-scale pores in siliceous mudstones of the Mississippian Barnett Shale. Journal of Sedimentary Research, 79, 848–861. doi:10.2110/jsr.2009.092.

Maliva, R. G., Budd, D. A., Clayton, E. A., Missimer, T. M., & Dickson, J. A. D. 2011. Insights into the dolomitization process and porosity modification in sucrosic dolostones, Avon Park Formation (Middle Eocene), East-Central Florida, U.S.A. J. Sediment. Res. 81(3), 218–232.

Markin, A. N., Trukhin, I. S., Polyakova, N. V., Zadorozhny, P. A., and S. V. Sukhoverkhov. 2019. Study of the formation of carbonate scale in oilfield equipment of the Piltun-Astokhskoye field (Sakhalin Island) (Russian). *OIJ* 2019: 90–93. doi: https://doi.org/10.24887/0028-2448-2019-4-90-93.

MacQueen, J. B. 1967. Some Methods for classification and Analysis of Multivariate Observations. Proceedings of 5th Berkeley Symposium on Mathematical Statistics and Probability. University of California Press. pp. 281–297.

Mattaboni, P. and Schreiber, E. 1967. Method of pulse transmission measurements for determining sound velocities. Journal of Geophysical Research, 72(20), pp.5160-5163.

Mayorga-Gonzalez, L., & Sonnenberg, S. 2021. High-Resolution Reservoir Characterization of the Lewis Shale, Greater Green River Basin, Wyoming. Paper presented at the SPE/AAPG/SEG Unconventional Resources Technology Conference, Houston, Texas, USA. doi: https://doi.org/10.15530/urtec-2021-5653.

Merletti, G.D., Spain, D.R., Pour, R.A., & Zett, A. 2014. Understanding Depositional And Diagenetic Processes Improve Petrophysical Rock Typing Workflows in Tight Gas Reservoirs. Presented at SPWLA 55th Annual Logging Symposium, 18-22 May, Abu Dhabi, UAE.

Mighani, S. 2014. Microseismic Rock Tensile Failure Related To Improving Hydraulic Fracturing, M.S. thesis, University of Oklahoma.

Nielsen, F. 2016. Hierarchical Clustering. In: Introduction to HPC with MMPI for Data Science. Undergraduate Topics in Computer Science. Springer, Cham. https://doi.org/10.1007/978-3-319-21903-5_8

Nuccio, V. F., & Robberts, P. 2003. Maturation and source rock mapping of the Uinta Basin, Utah and Colorado. American Association of Petroleum Geologists Bulletin, 87(10), 1491-1515.

Oleson, N. E. 1986. Petroleum geology of the Eocene lower Green River Formation, Duchesne and Uintah counties, Utah. M. S. Thesis, Baylor University, 173p.

Opencv. 2017. Introduction to Support Vector Machines. Web Address: http://docs.opencv.org/2.4/doc/tutorials/ml/introduction_to_svm/introduction_to_svm.ht ml (Accessed Mar 27, 2017).

Pearce, T. J., Wray, D. S., Ratcliffe, K. T., Wright, D. K., and Moscariello, A. 2005. Chemostratigraphy of the Upper Carboniferous Schooner Formation, Southern North Sea, in Collinson, J.D., Evans, D.E., Holliday, D., and N. Jones, (eds) Carboniferous Hydrocarbon Geology: The Southern North Sea and Surrounding Onshore Areas, Yorkshire Geological Society Occasional Publication 7, pp 147-164.

Pearce, T. J., and Jarvis, I. 1992. Applications of Geochemical Data to Modelling Sediment Dispersal Patterns in Distal Turbidites: Late Quaternary of the Madeira Abyssal Plain, Journal of Sedimentary Petrology, 62, 1112-1129

Pearce, T. J., Besly, B. M., Wray, D. S., and Wright, D. K. 1999. Chemostratigraphy: A Method to Improve Interwell Correlation in Barren Sequences – a Case Study Using Onshore

Duckmantian/Stephanian Sequences (West Midlands, U.K.). Sedimentary Geology, 124, 197-220.

Pearson, K. 1901. On Lines and Planes of Closest Fit to Systems of Points in Space. Philosophical Magazine. 2 (11): 559–572. doi:10.1080/14786440109462720.

Perez, R., and Marfurt, K. 2013. Calibration of Brittleness to Elastic Rock Properties via Mineralogy Logs in Unconventional Reservoirs. Oral Presentation at AAPG International Conference and Exhibition, Cartagena, Colombia, 8-11 September.

Picard M. D. 1957. Green Shale Facies, Lower Green River Formation, Utah. *AAPG Bulletin* : 41 (10): 2373–2376. doi: https://doi.org/10.1306/0BDA5999-16BD-11D7-8645000102C1865D

Pittman E. D. 1992. Relationship of Porosity and Permeability to Various Parameters Derived from Mercury Injection – Capillary Pressure Curves for Sandstones. AAPG Bulletin Vol. 76(2): 191-198, ISSN 0149-1423.

Rahmanian, M., Solano, N., and Aguilera, R. 2010. Storage and Output flow from Shale and Tight Gas Reservoirs. SPE 13361. Presented at SPE Western Regional Meeting, 27- 29 May, Anaheim, California. SPE 133611-MS doi: 10.2118/133611-MS.

Randolph, P. L., Soeder, D. J., & Chowdiah, P. 1984. Porosity and Permeability of Tight Sands. Presented at Unconventional Gas Recovery Symposium, 13-15 May, Pittsburg, PA. SPE-12836. doi:10.2118/12836-MS.

Ramkumar, M. 2015. Chemostratigraphy Concepts, Techniques, and Applications, first edition: Elsevier.

Rebelle, M. & Bruno, L. 2014. Rock-Typing in Carbonates: A Critical Review of Clustering Methods. Presented at the Abu Dhabi International Petroleum Exhibition and Conference, 10-13 November, Abu Dhabi, UAE. SPE-171759-MS.

Rebelle, M., Umbhauer, F., and Poli, E. 2009. Pore to Grid Carbonate Rock-Typing. Presented at the International Petroleum Technology Conference, 7-9 December, Doha, Qatar. IPTC 13120.

Ringnér M. 2008. What is principal component analysis? Nat Biotechnol. Doi: 10.1038/nbt0308-303. PMID: 18327243.

Roehler H. W. 1993. Eocene climates, depositional environments, and geography, greater Green River basin, Wyoming, Utah, and Colorado. https://doi.org/10.3133/pp1506F.

Rushing, J. A., Newsham, K. E., & Blasingame, T. A. 2008. Rock Typing: Keys to Understanding Productivity in Tight Gas Sands. Presented at Unconventional Reservoirs Conference, 10-12 February, Keystone, Colorado. SPE-114164. doi:10.2118/114164-MS.

Sageman, B.B. and Lyons, T.W. 2004. Geochemistry of Fine-Grained Sediments and Sedimentary Rocks. In: Mackenzie, F. (ed.) Sediments, Diagenesis, and Sedimentary Rock. Treatise on Geochemistyr, 7, 115-158.

Schieber, J. 2010. Common Themes in the Formation and Preservation of Intrinsic Porosity in Shales and Mudstones – Illustrated With Examples Across the Phanerozoic. Presented at SPE Unconventional Gas Conference, Pittsburg, Pennsylvania, USA, 23- 25 Feb 2010.

Schiffmann, K. I. 2011, Determination of fracture toughness of bulk materials and thin films by nanoindentation: comparison of different models, Phil. Mag. 91,7-9, 1163-1178.

Shao-rong, F. (2007). Research and Improvement of Decision Trees Algorithm. *Journal of Xiamen University*.

Shukla, P. 2013. Nanoindentation Studies on Shales. Master Thesis, University of Oklahoma, Norman, Oklahoma.

Shukla, P., Kumar, V., Curtis, M., Sondergeld, C., & Rai, C. 2013. Nanoindentation Studies on Shales. ARMA 13-578. Presented at 47th US Rock Mechanics/Geomechanics Symposium held in San Francisco, CA, USA 23-26 Jun 2013.

Sondergeld, C., & Rai, C. Elastic anisotropy of shales. 2011. *The Leading Edge*; 30 (3): 324–331. doi: https://doi.org/10.1190/1.3567264.

Sondergeld, C., & Rai, C. 1993. A New Concept of Quantitative Core Characterization. The Leading Edge 12(7): 774-779.

Sondhi, N. 2011. Petrophysical characterization of the Eagle Ford shale, Master Thesis, Oklahoma U., Norman, Oklahoma.

Spain, D.R., & Liu, S. 2011. Petrophysical Rock Typing of Tight Gas Sands – Beyond Porosity and Saturation: Example from the Cotton Valley Formation, East Texas. Presented at SPE Middle East Unconventional Gas Conference and Exhibition, 31 Jan – 2 Feb, Muscat, Oman. SPE 142808.

Tan, P.N., Steinbach, M., & Kumar, V. 2006. Introduction to Data Mining. *Pearson Addison-Wesley*.

Tavakoli, V. 2017. Application of gamma deviation log (GDL) in sequence stratigraphy of carbonate strata, an example from offshore Persian Gulf, Iran. J. Petrol. Sci. Eng. 156, 868–876.

Tavakoli, V. 2020. Carbonate Reservoir Heterogeneity: Overcoming the Challenges. Springer, 108pp.

Tavakoli, V. 2015. Chemostratigraphy of the Permian-Triassic Strata of the Offshore Persian Gulf, Iran, pp. 373–393. Chemostratigraphy: Concepts, Techniques,

Timur, A. 1968. An Investigation of Permeability, Porosity, and Residual Water Saturation Relationship for Sandstone Reservoirs, The Log Analyst, Vol. 9, No. 4, (July-August 1968), pp. 8.

Thimm, H. F. 2006. Understanding the Generation of Dissolved Silica in Thermal Projects: Theoretical Progress. Paper presented at the Canadian International Petroleum Conference, Calgary, Alberta. doi: https://doi.org/10.2118/2006-137.

Thomas C. & Chidsey, Jr., 2018. Uinta Basin Produced Water. Retrieved from geology.utah.gov/map-pub/survey-notes/uinta-basin-produced-water.

Thomeer J. H. 1983. Air Permeability as a Function of Three Pore Network Parameters. *Journal of Petroleum Technology*, 35(4): 809-814.

Thornton, C. 2017. Machine Learning – Lecture 15 Support Vector Machines. Web Address: http://users.sussex.ac.uk/~christ/crs/ml/lec08a.html (Accessed 27 Mar 2022).

Trumbo, J. 1993. Petrophysical evaluation of the Castle Peak Sandstone, Green River Formation, Uinta Basin, Utah. Journal of Petroleum Science and Engineering, 10(3), 209-225.

Tribovillard, N., Algeo, T.J., Lyons, T., and Riboulleau, A. 2006. Trace Metals as Paleoredox and Paleoproductivity Proxies: An Update. Chemical Geology, 232, 12-32.

Tribovillard, N., Bout-Roumazeilles, V., Algeo, T., Lyons, T. W., Sionneau, T., Montero-Serrano, J.C., Riboulleau, A., & Baudin, F. 2008., Paleodepositional Conditions in the Orca Basin as Inferred From Organic Matter and Trace Metal Contents, Marine Geology, v 254, pp 62-72, doi: 10.1016/j.margeo.2008.04.016.

U.S. Geological Survey. (2012). Geology of Tight Oil and Potential Tight Oil Reservoirs in the Lower Part of the Green River Formation. Retrieved from https://www.usgs.gov/publications/geology-tight-oil-and-potential-tight-oil-reservoirs-lower-part-green-river-formation

Vafaie, A., Habibnia, B., Moallemi, S.A., 2015. Experimental investigation of the pore structure characteristics of the Garau gas shale formation in the Lurestan Basin. Iran. J. Nat. Gas Sci. Eng. 27 (2), 432–442.

Vafaie, A., & Rahimzadeh Kivi, I. 2020. An investigation on the effect of thermal maturity and rock composition on the mechanical behavior of carbonaceous shale formations. Marine and Petroleum Geology, 116, 104315. https://doi.org/10.1016/j.marpetgeo.2020.104315

Walton, P. T. 1994. Geology of the Cretaceous of the Uinta Basin, Utah. *GSA Bulletin* 55 (1): 91–130. doi: https://doi.org/10.1130/GSAB-55-91.

Wang, F. P., and R. M. Reed, 2009, Pore networks and fluid flow in gas shales: Society of Petroleum Engineers Annual Technical Conference and Exhibition, New Orleans, Louisiana, October 4–7, 2009, SPE Paper 124253, 8 p., doi:10.2118/124253-MS.

Wang, F. P., and J. F. W. Gale, 2009, Screening criteria for shale -gas systems: GCAGS Transactions, v. 59, p.779–793.

Walls, J. D. 1982. Tight Gas Sands Permeability, Pore Structure, and Clay, *Journal of Petroleum Technology*, (1982b) 2708-2714.

Wendte, J., Byrnes, A., & Sargent, D. 2009. The control of hydrothermal dolomitization and associated fracturing on porosity and permeability of reservoir facies of the upper Devonian Jean Marie member (Redknife formation) in the July Lake area of northeastern British Columbia. Bull. Can. Petrol. Geol. 57(4), 387–408.

Williams J. L. 2008. Energy Economist: Wells and Politics, Web link: http://www.energyeconomist.com/a6257783p/archives/ee080611exp.html.

Wu, J., Zhang, S., Cao, H., Zheng, M., Sun, P., & Luo, X. 2018. Fracability evaluation of shale gas reservoir-A case study in the Lower Cambrian Niutitang formation, northwestern Hunan, China. J. Petrol. Sci. Eng. 164, 675–684.

Xu, C., & Verdin, C.T. 2013. Core-Based Petrophysical Rock Classification By Quantifying Pore-System Orthogonality With a Bimodal Gaussian Density Function. Presented at International Symposium of the Society of Core Analysts, 16-19 Sep, California, USA. SCA2013-079.

Zhang, C., & Ma, Y., 2012. Ensemble machine learning: methods and applications.

Zheng, X., Spiro, B., & Han, Z. 2020. Comparison of Geochemical and Mineralogical Characteristics of Palaeogene Oil Shales and Coals from the Huangxian Basin, Shandong Province, East China. *Minerals*, *10*(6), 496. https://doi.org/10.3390/min10060496.